

MC@NLO for Heavy Flavour Photoproduction at HERA

Dissertation

zur Erlangung des Doktorgrades
des Department Physik
der Universität Hamburg

vorgelegt von

Tobias Toll

aus Norrtälje

Hamburg
Januar 2010

Gutachter der Dissertation:

Dr. Hannes Jung
Prof. Dr. Peter Schleper

Gutachter der Disputation:

Dr. Hannes Jung
Prof. Dr. Joachim Bartels

Datum der Disputation:

15. Januar 2010

Vorsitzender des Prüfungsausschusses:

Prof. Dr. Robert Klanner

Vorsitzender des Promotionsausschusses:

Prof. Dr. Robert Klanner

Dekan der MIN Fakultät:

Prof. Dr. Heinrich Graener

Leiter des Department Physik:

Prof. Dr. Joachim Bartels

Abstract

A Monte Carlo at next-to-leading order (MC@NLO) has been constructed for the production of heavy quark flavours in photoproduction. As such, it is the first Monte Carlo event generator with next-to-leading order (NLO) accuracy for a process in lepton hadron scattering.

In order to construct such an MC@NLO, the matrix element for the process has to be calculated at NLO and then be matched with a parton shower. When doing this, it is important that none of the parton configurations produced are doubly counted.

In this thesis, the concept of a Monte Carlo event generator will be explained, with emphasis on the HERWIG parton shower. Also, different techniques of calculating matrix elements at NLO accuracy will be explained. It will then be shown how the NLO calculation can be matched with the HERWIG parton shower in an MC@NLO without double counting, producing unweighted events at NLO-accuracy.

Many comparisons are made between the MC@NLO here constructed, the HERWIG Monte Carlo and the FMNR NLO calculation. Also many comparisons are made to HERA data from the H1 and ZEUS experiments. It is shown that all HERA data with heavy quarks produced in photoproduction can be described by the MC@NLO program constructed in this thesis.

Kurzfassung

Es wurde ein Monte-Carlo-Ereignisgenerator in nächstführender Ordnung (MC@NLO) für die Photoproduktion schwerer Quarks erstellt. Als solches ist es der erste Ereignisgenerator für Lepton-Hadron-Streuung in nächstführender Ordnung (next-to-leading order, NLO). Für die Konstruktion eines MC@NLO muss das Matrixelement für die entsprechenden Prozesse zur NLO berechnet werden und mit Partonschauer in Übereinstimmung gebracht werden. Dabei muss darauf geachtet werden, dass keine Partonkonfiguration doppelt gezählt wird.

In dieser Arbeit wird das Konzept eines MC@NLO dargestellt, wobei der Schwerpunkt auf dem Partonschauer des Ereignisgenerators HERWIG liegt. Verschiedene Techniken für die Berechnung von Matrixelementen in nächstführender Ordnung werden erklärt. Daraufhin wird gezeigt, wie die NLO-Berechnungen mit dem Partonschauer aus HERWIG in Übereinstimmung gebracht werden können, ohne dass Partonkonfigurationen doppelt gezählt werden. Daraus resultieren ungewichtete Ereignisse mit NLO-Präzision.

Vergleiche zwischen dem in dieser Arbeit konstruierten MC@NLO, dem Ereignisgenerator HERWIG und der NLO Berechnung FMNR werden präsentiert. Ein Vergleich mit Schwerquarkdaten der HERA-Experimente H1 und ZEUS zeigt, dass dieser MC@NLO die Messungen in Photoproduktion beschreiben kann.

Contents

| | | |
|----------|--|-----------|
| 1 | Introduction to Quantum Chromo Dynamics | 1 |
| 1.1 | Quantum Chromo Dynamics | 9 |
| 1.1.1 | Feynman Diagrams and Renormalization | 10 |
| 1.1.2 | Lepton Hadron Scattering in the Quark Parton Model | 14 |
| 1.1.3 | Adding QCD to the DIS Cross-Section | 18 |
| 1.1.4 | The DGLAP equations | 23 |
| 1.1.5 | Heavy Quarks in Photoproduction | 25 |
| 2 | Monte Carlo Techniques and the HERWIG Event Generator | 28 |
| 2.1 | Monte Carlo Integration | 31 |
| 2.1.1 | Selection From a Distribution | 34 |
| 2.2 | Generating Parton Showers | 35 |
| 2.2.1 | Initial State Parton Showers | 37 |
| 2.2.2 | Parton Showers are Solutions to the DGLAP Equations | 38 |
| 2.3 | The HERWIG Parton Shower | 41 |
| 2.3.1 | The Angular Ordered Phase-space for Heavy Quarks | 43 |
| 2.4 | Hadronization | 44 |
| 2.4.1 | Independent Fragmentation | 44 |
| 2.4.2 | Cluster Fragmentation | 46 |
| 2.4.3 | Lund String Fragmentation | 47 |
| 2.5 | Other Parton Evolutions | 49 |
| 3 | Next-to-leading Order Calculations | 51 |
| 3.1 | A Toy Model of a Next-to-Leading Order Cross-section Calculation | 54 |

| | | |
|----------|---|------------|
| 3.1.1 | The Phase Space Slicing Method | 56 |
| 3.1.2 | The Subtraction Method | 57 |
| 3.2 | The Subtraction Method in QCD | 58 |
| 3.2.1 | Soft and Collinear Limits | 58 |
| 3.2.2 | Collinear Factorization at NLO | 59 |
| 3.3 | eP Cross-Sections | 61 |
| 3.3.1 | A Description of the Calculation | 64 |
| 3.4 | Calculating Total and Differential Cross-sections at NLO | 68 |
| 3.5 | Dipole Subtraction | 68 |
| 4 | Monte Carlo at Next-to-leading Order | 70 |
| 4.1 | A Toy Monte Carlo at Next-to-leading Order | 71 |
| 4.2 | MC@NLO for eP scattering | 73 |
| 4.2.1 | Projecting the $2 \rightarrow 2$ configuration onto the $2 \rightarrow 3$ configuration | 75 |
| 4.2.2 | HERWIG Showering Variables in the Form of $2 \rightarrow 3$ invariants | 79 |
| 4.2.3 | The Monte Carlo Subtraction Terms for $\gamma^*P \rightarrow Q\bar{Q}$ | 81 |
| 4.2.4 | Local Cancellation of IR Singularities | 85 |
| 4.3 | Generating MC@NLO Events | 86 |
| 4.4 | Other Matching Schemes of NLO-Matrix Element and Parton Showers | 88 |
| 5 | Phenomenological Comparisons at Parton-level | 90 |
| 5.1 | Parton Dynamics | 91 |
| 5.1.1 | Influence of Events with Negative Weights | 94 |
| 5.1.2 | Influence of the Photon | 97 |
| 5.2 | Scale Variations | 99 |
| 6 | Comparisons to Measurements of Heavy Quarks at HERA | 104 |
| 6.1 | Comparisons to Measurements of $D^{*\pm}$ Mesons | 104 |
| 6.2 | Comparisons to Beauty Measurements | 114 |
| 6.3 | Comparisons with Other Calculations | 122 |
| 6.4 | Conclusions | 122 |
| 7 | Summary and Outlook | 124 |

| | |
|--|------------|
| A Dimensional Regularization | 128 |
| B Generating a Parton Shower by use of the Veto Algorithm | 132 |
| Bibliography | 135 |

*To my mother, father, sister and brother,
Gunilla, Gunnar, Johanna and Michael .*

Chapter 1

Introduction to Quantum Chromo Dynamics

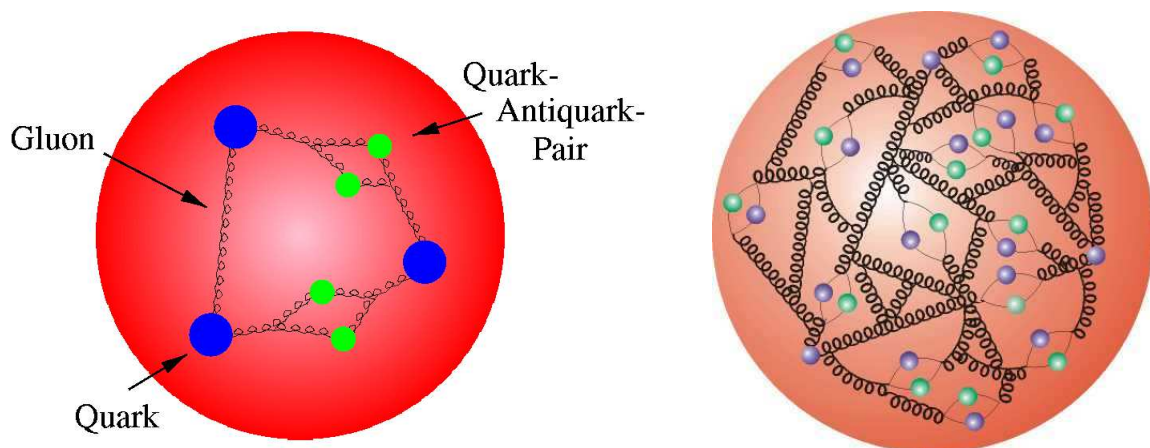


Figure 1.1: Question: What is a proton made of? Answer: It depends on how you look at it.

At the particle accelerator HERA, located at the DESY site in Hamburg, protons are made to collide with electrons at high energies. The central question to be answered measuring these collisions is: What is a proton? To answer this question, a detailed knowledge of the theory of the forces involved is needed. But it can be useful to first have a picture of what goes on in the interaction, to have an intuitive understanding of what a proton is.

It is known that the proton gets many of its characteristics from three particles, two up-quarks and one down-quark. These are called valence quarks. The up-quarks have an electric charge of $+2/3$ and the down-quark, of $-1/3$. From these three quarks the proton gets for example its electric charge of $+1$. But the quarks are held together in the proton by the strong force, and the strong force field consists of virtual gluons, which means that

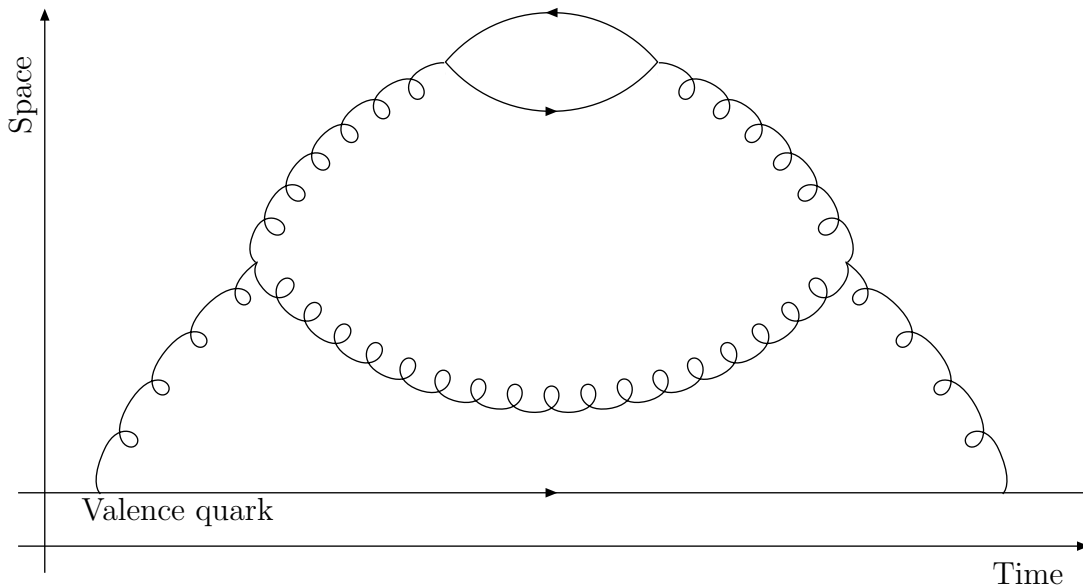


Figure 1.2: An example of a virtual partonic chain in a proton. A valence quark emits a virtual gluon and reabsorbs it later. This virtual gluon splits into a virtual gluon pair. One of the gluons in this pair splits into a virtual sea-quark pair. The sea-quark pair is then recombined, as is the gluon pair. The remainder of the virtual chain is then reabsorbed by the valence quark.

the proton also contains gluons.

Measurements show that approximately half of the proton's momentum is carried by gluons. The proton may therefore be viewed as the three valence quarks surrounded by a cloud of virtual gluons. That the gluons are virtual means they borrow the energy for their existence in accordance with Heisenberg's uncertainty principle. The time a gluon can exist in this way is proportional to its wavelength. A virtual gluon with a large wavelength may therefore exist long enough to split into a pair of other virtual gluons with shorter wavelengths. These gluons may in their turn split into yet other pairs of gluons with even shorter wavelengths. This means that however large or small a region one looks at inside the proton, one will always find gluons within that region. In this sense, the gluon field is self-similar at different scales. But there is a non-linear factor that makes the proton lose this self-similarity: the gluons can split up into quark anti-quark pairs as well as into gluons. These quarks and anti-quarks are called sea quarks. The energy needed to create such a pair depends on the quark mass, and the masses are extremely different for different quarks. This means that only gluons with wavelengths shorter than twice the seaquark mass can split up into a sea quark-antiquark pair. The seaquarks, gluons and valence quarks go by the common name of partons.

Each given gluon or sea quark belongs in this way to a parton chain of radiations. They all are radiated by a parton with larger wavelength which in its turn was radiated by a

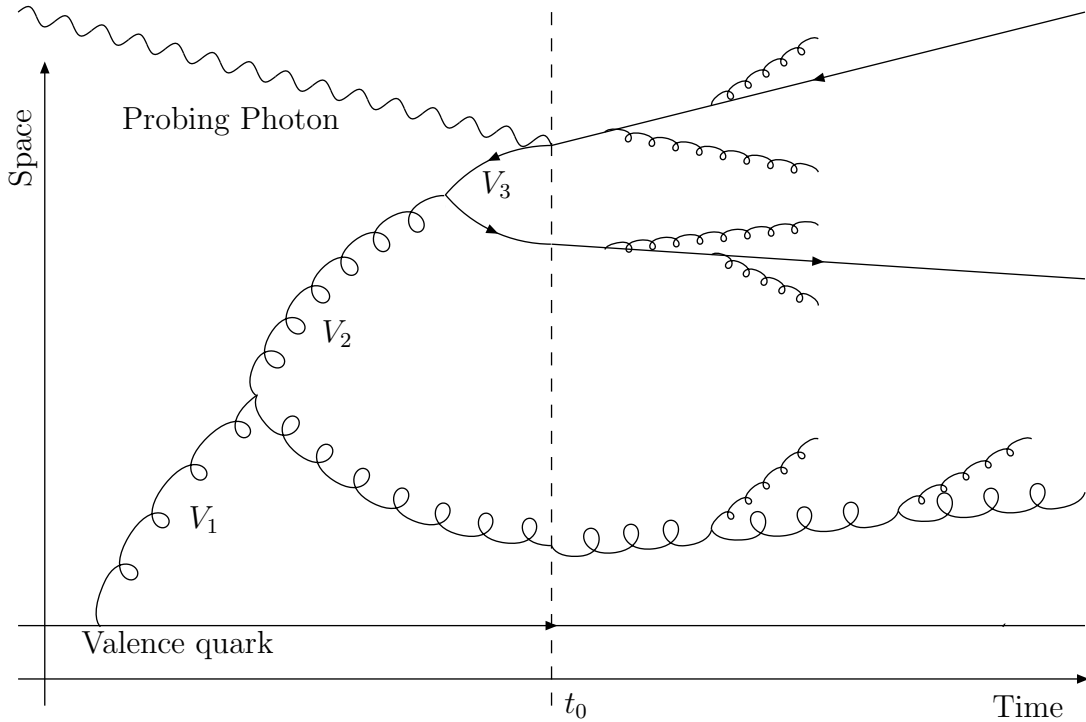


Figure 1.3: When a photon interacts with a quark in the virtual parton chain at a time t_0 in fig. 1.2, this chain may become real. If the quark gets a hard enough kick by the photon, the whole chain may be kicked out of the proton. On the way out, the now real quark, antiquark and gluon will radiate bremsstrahlung resulting in three jets. In this picture, the radiations are automatically ordered in virtuality V , such that $V_1 < V_2 < V_3$.

parton of even larger wavelength up until the valence quark. Each parton also belongs to a chain of other partons of ever smaller wavelengths. At each moment many such parton chains exist in the proton, and they keep fluctuating in and out of existence. In fig. 1.2, one example of such a parton chain is illustrated.

The next question is: how can one look into a proton and see these parton chains? To do this, one needs a probe which can interact with the partons. At HERA, electrons were made to collide with the proton, which then interacted electro-magnetically via the exchange of a virtual photon, which acts as a probe. This photon probe can only interact with partons which carry electric charge, and will therefore only interact with either valence or sea-quarks. However, in order for the photon to resolve the electric charge of a quark or an antiquark, its wavelength needs to be small enough to resolve the quark-antiquark pair. If the distance between the quark and its antiquark is much smaller than the photon's wavelength, the charge of the antiquark will screen the charge of the quark, which means the photon cannot interact with any of them. Therefore, the smaller the wavelength of the photon, the more partons it can resolve. If the photon interacts with a virtual sea-quark, this sea-quark can become real. The seaquark comes from a chain of

radiations of partons at larger scales, which means that this whole chain becomes real, while all the other possible chains of radiations do not contribute to the interaction. This can be compared with the collapse of the wave function in classical quantum mechanics, where out of all possible outcomes of a measurement, only one eigenstate of the measurement is realised. In fig. 1.3, the chain in fig. 1.2 becomes real by interacting with a photon, producing three real partons.

If the struck quark gains enough energy by the probe it will be kicked out of the proton, together with its parton chain, resulting in a cascade of partons. It will still be connected to the left-behind proton remnant by the strong force, and while decelerating in this force-field, it will radiate gluon bremsstrahlung, as will the partons contained in the parton chain. The struck quark and all the radiated partons cannot exist as free particle and they will become confined in hadrons, which may then be measured by the detectors surrounding the collision points in the accelerator.

The virtual photon may also split up into a quark anti-quark pair, which may also radiate gluons, hence sometimes, when one wants to probe the proton with a virtual photon, one ends up probing the photon as well ¹. Also, the proton structure may be much more complicated than has been described here. In fig. 1.4 one example of a more complicated structure is shown.

This is the principal behind all high energy measurements in particle accelerators: the more energetic the probe, the closer one looks and the greater the structure revealed, a structure manifested in the different kinds of hadrons reaching the detectors.

Structure of the Theses

The goal of this chapter is to give a mathematical description of the proton structure in the pictures shown in figures 1.2 and 1.3, which goes by the name of DGLAP-evolution. The techniques of Monte Carlo integration and parton showers, used to solve the emerging equations and to simulate the events, will be described in chapter 2. The following two chapters will describe a way to improve these calculations, first with next-to-leading order calculations described in chapter 3 and then how that is combined with parton showers in an MC@NLO in chapter 4. The construction of such an MC@NLO is the purpose of this thesis. In chapter 5, the results from the new MC@NLO are shown at the parton-level and in chapter 6, comparisons are made with HERA measurements.

To give a mathematical description of the proton, the starting point will be classical mechanics.

¹This may be compared to the concept of Wittgenstein's ruler in philosophy: if you want to measure a table with a ruler your result will depend on how well you know the length of the ruler. If the length of the ruler is unknown you will measure the length of the ruler with the table as much as vice versa (or rather, when a student of physics tries to explain concepts in philosophy he risks showing his lack of knowledge in the subject as much as explaining the concept).

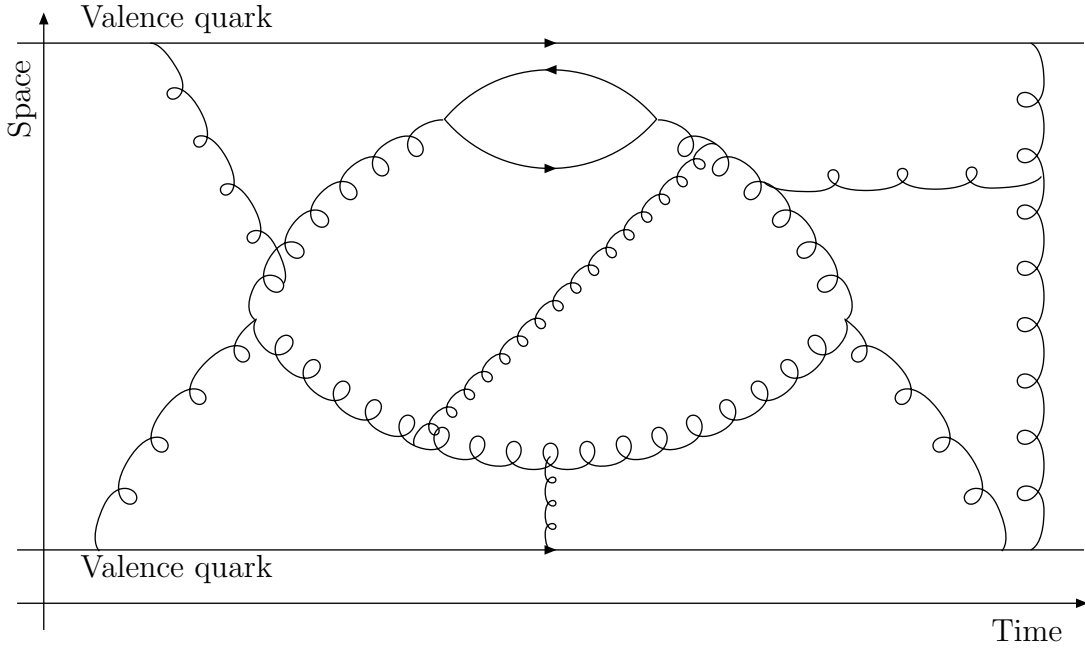


Figure 1.4: An example of a more complicated proton structure than that shown in fig. 1.2.

Hamilton's Principle of Least Action

The basis for all modern physics are derived from classical mechanics. In classical physics Hamilton's principle states that the motion of a system between times t_1 and t_2 is described as the minimum of the action

$$S = \int_{t_1}^{t_2} L(q_1, \dots, q_n, \dot{q}_1, \dots, \dot{q}_n, t) dt, \quad (1.1)$$

where L is called the Lagrangian of the system, q_i are the generalized coordinates and \dot{q}_i their time derivative. The Lagrangian is the difference between the kinetic and potential energy of the system

$$L = T - V. \quad (1.2)$$

Finding an extreme to the action is equivalent to solving the following equations called the Euler-Lagrange equations

$$\sum_{i=1}^n \left(\frac{d}{dt} \frac{\partial L}{\partial \dot{q}_i} - \frac{\partial L}{\partial q_i} \right) = 0. \quad (1.3)$$

In classical mechanics the equations of motions for any system can in principle be obtained by solving these equations. In reality most systems are too complicated, so even if the equations by which the system is described are known, there is no possibility to solve those

equations. A famous historical example is the three-body problem, which is a system with three bodies interacting with a $1/r$ force. The problem is still not analytically solved.

Here a classical system is defined as being both non-relativistic and non-quantum mechanical. But Hamilton's principle is applicable far beyond these classical limits. In special relativity the action becomes

$$S = - \int_C L d\tau = -mc^2 \int_{t_1}^{t_2} \sqrt{1 - \frac{v^2}{c^2}} dt, \quad (1.4)$$

for a single free particle with mass m . The speed of light c will from now on be set equal to 1. This action gives the Euler-Lagrange equation

$$0 = \gamma m \dot{v} = \gamma m \ddot{x}, \quad (1.5)$$

where $\gamma = 1/\sqrt{1-v^2}$. This tells us that a free particle moves in straight lines in space-time. Also in General Relativity, Einstein's theory of gravity, the main equations can be derived using Hamilton's principle, with the Einstein-Hilbert action.

An equivalent formulation of action is to use Lagrangian densities \mathcal{L} , integrated over space-time, instead of Lagrangians, such that

$$S = \int_{t_1}^{t_2} L dt = \int_V \mathcal{L} d^4x, \quad (1.6)$$

where x is a space-time four-vector. In the following the density \mathcal{L} will also be referred to as the Lagrangian. In quantum mechanics the action gets a more significant role, since the particles are now described by wave functions describing the probability distribution in space-time to find the particle (or the system of particles) in a specific state. Here, the wave function Ψ is given directly from the action as follows

$$\Psi(x) = A(x) e^{i\frac{S}{\hbar}}, \quad (1.7)$$

where $A(x)$ is a normalization such that the total probability is equal to unity, and \hbar is Dirac's constant, which is Planck's constant h divided by 2π . \hbar can be interpreted in quantum mechanics as the unit action, since it has the same units and dimensionality as the action. In the following \hbar will be set to unity.

Example: Classical Electro Dynamics

Maxwell's theory of electro magnetics is classical in the sense that it is non-quantum mechanical. It is, however, relativistic. The Maxwell equations read:

$$\nabla \cdot \mathbf{E} = \rho \quad (\text{Gauss's Law}) \quad (1.8)$$

$$\nabla \cdot \mathbf{B} = 0 \quad (\text{No magnetic monopoles}) \quad (1.9)$$

$$\nabla \times \mathbf{B} = \mathbf{J} + \frac{\partial \mathbf{E}}{\partial t} \quad (\text{Modified Ampere's law}) \quad (1.10)$$

$$\nabla \times \mathbf{E} = -\frac{\partial \mathbf{B}}{\partial t} \quad (\text{Faraday's and Lenz's law}) \quad (1.11)$$

Here \mathbf{E} is the electric field, \mathbf{B} the magnetic field, ρ the charge density and \mathbf{J} the charge current.

This can be reformulated into a Lagrangian theory. Define a vector potential \mathbf{A} and a scalar potential ϕ . These can be combined into a four-vector:

$$A^\mu = (\phi, \mathbf{A}). \quad (1.12)$$

Also the current and charge density can be combined into a four-vector:

$$J^\mu = (\rho, \mathbf{J}) \quad (1.13)$$

A Lagrangian may then be defined as

$$\mathcal{L}_{EM} = \frac{1}{2}(\mathbf{E}^2 - \mathbf{B}^2) - \rho\phi + \mathbf{J} \cdot \mathbf{A}, \quad (1.14)$$

the Euler-Lagrange equations coming from this Lagrangian then gives back the Maxwell's equations. Defining an antisymmetric tensor:

$$F^{\mu\nu} = \partial^\mu A^\nu - \partial^\nu A^\mu, \quad (1.15)$$

the Lagrangian can be rewritten as

$$\mathcal{L}_{EM} = -\frac{1}{4}F_{\mu\nu}F^{\mu\nu} - J_\mu A^\mu. \quad (1.16)$$

Here the first term on the r.h.s. is the kinetic energy of the electro-magnetic field, while the second term contains the interactions and is hence the potential energy. In order to turn this into a modern quantum field theory of electro-magnetism, the field has to be quantized.

Lagrangians and Gauge Symmetries

In relativistic quantum mechanics, the Lagrangian density for a free fermion field is described by the Dirac Lagrangian

$$\mathcal{L}_0 = \psi^\dagger(x)(i\gamma^\sigma \partial_\sigma - m)\psi(x), \quad (1.17)$$

where ψ is the fermion field. There is a freedom in the solutions of the resulting kinematic equations in the choice of phase in the field, i.e. one can transform the field thus:

$$\psi(x) \rightarrow \psi'(x) = \exp(iQ\theta)\psi(x) \quad (1.18)$$

Since only the absolute square of the function $\psi(x)$ bares any physical meaning, this transformation, which is called a global gauge transformation, must leave all equations unchanged. However, if one allows the phase transformation to depend on the space-time

coordinate the free Lagrangian is no longer invariant. The phase redefinition $\theta \rightarrow \theta(x)$, gives by use of the chain rule:

$$\partial_\mu \psi(x) \rightarrow \exp(iQ\theta(x))(\partial_\mu + iQ\partial_\mu\theta(x))\psi(x). \quad (1.19)$$

Therefore, if one phase convention has been chosen by an observer at one point in space-time, the same convention needs to be taken by all observers in any space-time point in order for them to agree on any observation. This does not seem very natural. The ‘‘Gauge Principle’’ states that the local gauge transformation should leave the theory, as defined by the Lagrangian, invariant. This is only possible if one adds some additional piece to the Lagrangian, transforming it in such a way as to cancel the $\partial_\mu\theta(x)$ term in eq. (1.19). This can be obtained by introducing a new field $A_\mu(x)$ which transforms as:

$$A_\mu \rightarrow A'_\mu(x) = A_\mu(x) + \frac{1}{e}\partial_\mu\theta \quad (1.20)$$

and adding it to the differential operator and turning it into a so called covariant derivative $\partial_\mu \rightarrow D_\mu$, where

$$D_\mu\psi(x) = [\partial_\mu - ieQA_\mu(x)]\psi(x). \quad (1.21)$$

The covariant derivative transforms like the field itself:

$$D_\mu\psi(x) \rightarrow (D_\mu\psi)'(x) = \exp[iQ\theta(x)] D_\mu\psi(x). \quad (1.22)$$

The Lagrangian then becomes

$$\mathcal{L} = i\psi^\dagger(x)\gamma^\mu D_\mu\psi(x) - m\psi^\dagger(x)\psi(x) = \mathcal{L}_0 + eQA_\mu(x)\psi^\dagger(x)\gamma^\mu\psi(x) \quad (1.23)$$

and is unchanged under local gauge transformations. The local gauge transformation can be described as transformation between elements in the group $U(1)$. Just by invoking the gauge principle, there is now a term in the Lagrangian describing interactions between the fermion fields and the gauge field A_μ , which is a spin-1 field. The interaction term is nothing but the QED vertex and the electromagnetic charge eQ is completely arbitrary, and works as a parameter in the theory which needs to be measured. In order for the field A_μ to be a real propagating field, one also needs to add a gauge invariant kinetic term to the Lagrangian:

$$\mathcal{L}_{\text{Kin}} = -\frac{1}{4}F_{\mu\nu}F^{\mu\nu} \quad (1.24)$$

where $F_{\mu\nu}$ is defined in eq. (1.15). It is easy to show that a mass-term for the gauge field $\frac{1}{2}m^2 A^\mu A_\mu$ would violate gauge invariance and is therefore forbidden. Therefore the photon field is predicted to be massless. The symmetry $U(1)$ here described has been extremely successful in describing electro-magnetic phenomena. However it turns out not to be sufficient to describe any phenomena produced by the weak and strong forces. Those forces turns out to be gauge invariant under $SU(2)$ and $SU(3)$ symmetries respectively.

The forces describing all interactions in the standard model are thus symmetric under the symmetry group:

$$U(1) \times SU(2) \times SU(3) \quad (1.25)$$

giving the following covariant derivative:

$$D^\mu = \delta^\mu - ig_1 \frac{Y}{2} A^\mu - ig_2 \frac{\tau_i}{2} W_i^\mu - ig_3 \frac{\lambda_a}{2} G_a^\mu. \quad (1.26)$$

Here A^μ is the electro magnetic (photon) field, Y is the $U(1)$ generator and is just a number. τ_i are the Pauli matrices generating $SU(2)$ and W_i are the three weak boson fields (the W^+ , W^- and Z). Similarly λ_a are the 8 matrices generating $SU(3)$ and G_a are the 8 gluon fields. Substituting this covariant derivative into eq. (1.17) gives the standard model Lagrangian with all the interaction particles, the bosons.

What is still missing in the standard model are the fermions, which are the three families of leptons:

$$\begin{pmatrix} \nu_e \\ e \end{pmatrix} \begin{pmatrix} \nu_\mu \\ \mu \end{pmatrix} \begin{pmatrix} \nu_\tau \\ \tau \end{pmatrix} \quad (1.27)$$

and quarks:

$$\begin{pmatrix} u \\ d \end{pmatrix} \begin{pmatrix} c \\ s \end{pmatrix} \begin{pmatrix} t \\ b \end{pmatrix} \quad (1.28)$$

That is the whole standard model in a nut-shell (except for the Higgs mechanism). In the theory there are 15 masses and three coupling constants which all have to be measured (as well as some parameters related to the Higgs mechanism and CP-violation etc.).

1.1 Quantum Chromo Dynamics

For probing the proton, the $SU(3)$ part of the Lagrangian is the most important. This is the Quantum Chromo Dynamics part of the theory. The QCD effective Lagrangian can be separated into three part:

$$\mathcal{L}_{\text{eff}}^{\text{QCD}}(\psi_f(x), \bar{\psi}_f(x), A(x), c(x), \bar{c}(x) : g, m_f) = \mathcal{L}_{\text{classical}} + \mathcal{L}_{\text{gauge fixing}} + \mathcal{L}_{\text{ghost}}. \quad (1.29)$$

It is a function of three kinds of fields: fermion quark fields $\psi(x)$, boson gluon fields $A(x)$ and ghost fields $c(x)$. It also has a dependence upon two kinds of parameters: the strong coupling g and the quark masses m_f , where f label a distinct quark field (flavour). The classical density $\mathcal{L}_{\text{classical}}$ is invariant under local $SU(3)$ gauge transformations. The classical Lagrangian is:

$$\mathcal{L}_{\text{classical}} = \sum_f \bar{\psi}_f (iD[A] - m_f) \psi_f - \frac{1}{4} F_{\alpha\beta}^A F_A^{\alpha\beta} \quad (1.30)$$

where

$$F_{\alpha\beta}^A = [\partial_{\alpha}\mathcal{A}_{\beta}^A - \partial_{\beta}\mathcal{A}_{\alpha}^A - gf^{ABC}A_{\alpha}^BA_{\beta}^C]. \quad (1.31)$$

When comparing to eq. (1.15) one sees that it is the third term that distinguishes QCD from QED. This term is non-abelian.

1.1.1 Feynman Diagrams and Renormalization

The electro-magnetic part of the standard model, the Quantum Electro Dynamics (QED) has been the most successful theory ever. The success depends on some properties of the calculation of the theory called the sum of paths, or Feynman diagrams. The question usually being asked is: given an initial and a final state, what is the probability that something will happen. In QED the answer is: the probability of a certain final state to come from a certain initial state is the absolute squared of the sum of all possible intermediate states, i.e.:

$$\mathcal{P}(\text{Final state given initial state}) = \left| \sum \mathcal{A}(\text{All possible intermediate states}) \right|^2.$$

Where \mathcal{P} denotes probability and \mathcal{A} denotes probability amplitude. If the initial state is a photon at position A and the final state is a photon at position B and the rest of the universe is empty, this principle states that the photon will travel all possible paths between points A and B. One of these paths will be a straight line, another will deviate from the straight line in one direction, and yet another just as much in another direction. In the end all deviations from the straight line will cancel and the classical result of light traveling in straight lines is obtained.

Another type of the same kind of problem is the $2 \rightarrow 2$ process, where two particles in the initial state interacts leaving two particles in the final state. One example is when the initial state is an electron and a positron and the final state is a muon and an anti-muon. To solve this problem, Feynman diagrams are useful. These are diagrams with time on the horizontal and space on the vertical axis. This problem would then look like fig. 1.5, where the gray blob represents all possible intermediate states. These are infinitely many, since the leptons in both the initial and final states may radiate and reabsorb any number of virtual photons. A photon radiation is however not for free, its probability is proportional to the electromagnetic coupling strength and this turns out to be small. Therefore there is a way of ordering the possibilities of the blob in order of relevance, i.e. in order of how many times the electromagnetic coupling has to be used. In fig. 1.6 the most important diagrams contributing to this process are shown.

These diagrams can be used to calculate the cross-sections of different processes at a given order in the coupling with the Feynman rules. These rules are derived from the Lagrangian of the theory and are of two types: propagators and vertices. The propagators corresponds to a particle propagating between two points and is derived from the kinematic part

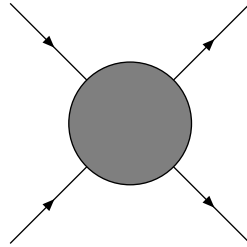


Figure 1.5: The $2 \rightarrow 2$ process. The blob represent all possible intermediate states.

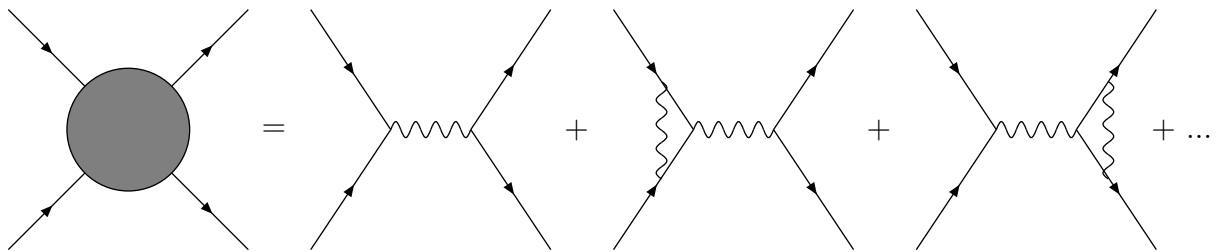


Figure 1.6: The $2 \rightarrow 2$ process unblobbed and ordered in the coupling.

of the Lagrangian, while the vertices are connection between different particle lines in space-time and correspond to the interactions in the Lagrangian. A diagram is then calculated convoluting the different vertices and propagators in the diagram. In figure 1.7 the Feynman rules for propagators in QCD are shown and the rules for QCD vertices are shown in fig. 1.8.

The ordering of the diagrams in orders of the coupling $\alpha = g^2/2\pi$ depends on the weakness of α . The coupling is however not a constant but depends on at which scale one looks at a vertex. To understand why, it is useful to think of an electromagnetic charge in vacuum. It is surrounded by a field which consists of virtual photons. These photons may fluctuate into charge-anticharge pairs, which forms virtual dipoles. These dipoles will be arranged in a way such that the anti-charge of the dipole will be closer to the original charge more often than the charge, in this way effectively screening the original charge. The larger the scale of the vertex, the smaller a distance is resolved and the less of the original charge is being screened. Therefore is the strength of the electro-magnetic coupling expected to increase with the scale.

To see this from the Feynman diagrams, one has to consider the loops on the propagators created by the pair-creation of charges. The measured electric charge e depends on the bare charge e_0 as shown in fig. 1.9. The contribution coming from one loop is given by

$$\begin{array}{ll}
\alpha, i \longrightarrow \longrightarrow \beta, j & i \frac{\delta_{ij}}{k^2 - m^2 + i\epsilon} [k + m]_{\beta\alpha} \\
\mu, b \text{ (wavy line) } \nu, a & i \frac{\delta_{ba}}{k^2 - m^2 + i\epsilon} \left[-g^{\mu\nu} + \frac{k^\mu n^\nu + n^\mu k^\nu}{n \cdot k} - n^2 \frac{k^\mu k^\nu}{(n \cdot k)^2} \right] \\
a \text{ (dashed line) } \longrightarrow \text{ (dashed line) } b & i \frac{\delta_{ba}}{k^2 + i\epsilon}
\end{array}$$

Figure 1.7: Feynman rules for the propagators in QCD. On top a quark-line, in the middle a gluon line and on the bottom a ghost line [1].

the calculation of the Feynman diagram for a loop resulting in [2]:

$$I(q^2) = \frac{\alpha_{\text{EM}}}{3\pi} \log \left(\frac{\mu_R^2}{q^2} \right) \quad (1.32)$$

where μ_R^2 is a large cut-off scale and q^2 the scale of the interaction. The right hand side of fig. 1.9 then becomes:

$$e^2 = e_0^2 \left[1 - I(q^2) + (I(q^2))^2 - (I(q^2))^3 + \dots \right] = e_0^2 \frac{1}{1 + I(q^2)} \quad (1.33)$$

Replacing $\alpha_{\text{EM}}^{(0)}$ with $\alpha_{\text{EM}}(\mu_R^2)$ one then obtains for the coupling:

$$\alpha_{\text{EM}}(Q^2) = \frac{\alpha_{\text{EM}}(\mu_R^2)}{1 - \frac{\alpha_{\text{EM}}(\mu_R^2)}{3\pi} \log \left(\frac{Q^2}{\mu_R^2} \right)} \quad (1.34)$$

Here one can see that when the probing scale Q^2 increases the electromagnetic coupling does indeed increase. A technique to calculate loop integrals is presented in appendix A.

For QCD the situation is more complicated, since there are more possible vertices. The self-interaction of the gluons makes it possible for the gluon propagator to split up into gluon loops. The result for the running coupling in this case is [1]:

$$\alpha_s(Q^2) = \frac{12\pi}{(33 - 2n_f) \log \frac{Q^2}{\Lambda_{\text{QCD}}^2}} \quad (1.35)$$

where

$$\Lambda_{\text{QCD}}^2 = \mu_R^2 \exp \left(\frac{-12\pi}{(33 - 2n_f) \alpha_s(\mu_R^2)} \right) \quad (1.36)$$

and n_f is the number of active quark flavours. Here it can be seen that α_s is decreasing with the scale. This means that for small scales the coupling strength becomes larger and

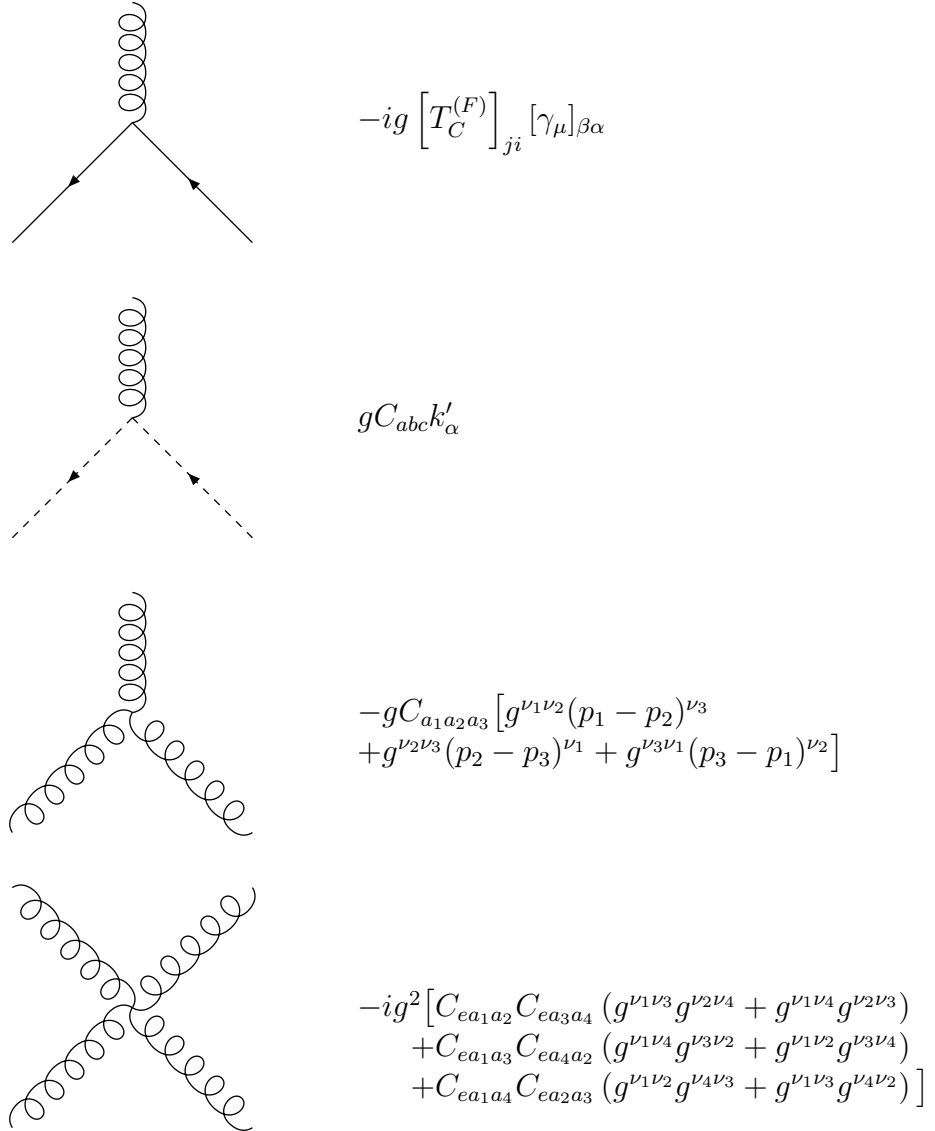


Figure 1.8: Feynman rules for the vertices in QCD.[1]

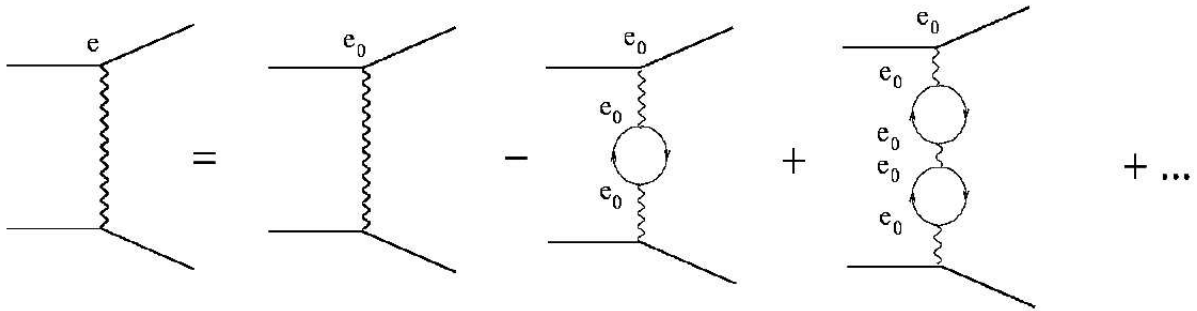


Figure 1.9: The observable electric charge e is different from the bare charge e_0 .

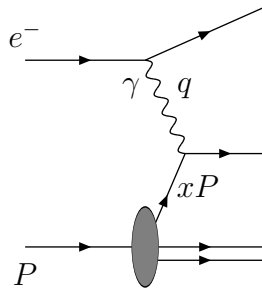


Figure 1.10: Inelastic $e^-P \rightarrow e^-X$ scattering.

for some scale $Q^2 \simeq \Lambda_{\text{QCD}}^2$, it becomes so large that the ordering of the Feynman diagrams by orders in the coupling breaks down. In this case the truncation of the perturbative expansion becomes unreliable and the interpretation that every possible intermediate state occurs weighted with a coupling is no longer valid for QCD. This means that when the separation between a colour and its anticolour becomes larger than a certain scale the perturbative approach breaks down. For these large length scales so-called colour confinement occur, where the colour-field between the colour and the anticolour is confined into a tube. This effect comes from the self-interaction of the gluon field.

On the other hand, for smaller length scales, i.e. for $Q^2 \gg \Lambda_{\text{QCD}}^2$, the coupling becomes small and the perturbative expansion approach becomes very good. This procedure to give the coupling an energy dependence is called normalization and μ_R is the renormalization scale. The scale-parameter μ_R^2 is a free variable and no observable should depend on it.

1.1.2 Lepton Hadron Scattering in the Quark Parton Model

In figure 1.10 an inelastic scattering between an electron and a proton is shown. Using the four-momenta of the incoming proton P , the incoming electron k and the scattered

lepton k' , the following Lorentz invariant variables can be defined:

$$s = (k + P)^2 \quad (1.37)$$

$$Q^2 = -q^2 = -(k - k')^2 \quad (1.38)$$

$$x = \frac{Q^2}{2Pq} \quad (1.39)$$

$$y = \frac{Pq}{Pk}. \quad (1.40)$$

Here s is the center of mass energy squared, and since the beam particles are highly relativistic the center of mass energy is $\sqrt{s} = 2\sqrt{E_P E_e}$ GeV. The variable Q^2 is the negative square of the photon four-momentum. It is the transfer of four-momentum from the electron to the proton. In the case of a photon exchange this corresponds to the virtuality of the photon. For $Q^2 \ll M_W^2 \approx 6400\text{GeV}^2$ the exchange of massive bosons is suppressed and can be safely ignored. The variables x and y can be interpreted as the momentum fractions of the proton and the electron taking part in the interaction respectively. Only three of these variables are independent and in the relativistic limit, where masses can be neglected, the following relation hold

$$Q^2 = xys \quad (1.41)$$

$$(1.42)$$

In the restframe of the proton, the energy the electron loses (or gains) in the interaction is

$$\nu = \frac{pq}{M_P} = (E_e - E'_e) \Big|_{\text{Rest}} \quad (1.43)$$

The general form of the eP scattering can be obtained from the leptonic and hadronic tensors [3]:

$$L_e^{\mu\nu} = \frac{1}{2} \text{Tr}((k' + m)\gamma^\mu(k + m)\gamma^\nu) \quad (1.44)$$

$$W^{\mu\nu} = -W_1 g^{\mu\nu} + \frac{W_2}{M^2} p^\mu p^\nu + \frac{W_4}{M^2} q^\mu q^\nu + \frac{W_5}{M^2} (p^\mu q^\nu + q^\mu q^\nu + q^\mu q^\nu) \quad (1.45)$$

such that

$$\frac{d^2\sigma}{dxdy} \propto L_{\mu\nu}^e W^{\mu\nu} \quad (1.46)$$

where the hadronic tensor $W^{\mu\nu}$ serves to parametrize our total ignorance of the structure of the proton. It can be shown, by conservation of current, that only two of the W_i are independent. These are called structure functions. The differential cross section as a function of these two structure functions is then [2]:

$$\frac{d^2\sigma}{dxdy} = \frac{4\pi\alpha_{\text{EM}}s}{Q^4} [xy^2 F_1 + (1-y)F_2] \quad (1.47)$$

where the structure functions F_1 and F_2 are defined as:

$$\begin{aligned} F_1 &= M_P W_1 \\ F_2 &= \nu W_2 \end{aligned}$$

These structure functions have to be measured. With a point-like proton the scattering would be elastic and they would become:

$$F_1(Q^2, \nu) = \frac{Q^2}{4M_P} \delta\left(\nu - \frac{Q^2}{2M_P}\right), \quad (1.48)$$

$$F_2(Q^2, \nu) = \nu \delta\left(\nu - \frac{Q^2}{2M_P}\right). \quad (1.49)$$

However, the proton is not a point particle, and for large values of Q^2 it in fact has many constituents.

To make a more realistic model of the proton, one can assume that it consists of pointlike spin 1/2 particles, called partons. Each parton carries a fraction ξ_i of the proton momentum such that $p_i^\mu = \xi_i P^\mu$. This means that the partons are collinear to the proton, i.e. they lack any momentum transverse to the proton direction. This model is called the quark parton model (QPM). The photon probe interacts with the parton i elastically which generates the following contribution to the structure functions:

$$F_1^{(i)}(Q^2, \nu) = \frac{e_i^2 Q^2 M_P}{4m_i^2} \delta\left(\nu - \frac{Q^2}{2m_i}\right) = \frac{e_i^2}{2} \delta(\xi_i - x) \quad (1.50)$$

$$F_2^{(i)}(Q^2, \nu) = \nu e_i^2 \delta\left(\nu - \frac{Q^2}{2m_i}\right) = e_i^2 x \delta(\xi_i - x) \quad (1.51)$$

where in the last step the relation $m_i = \xi_i M_P$ is used and x is defined above. In terms of ν , $x = Q^2/(2\nu M_P)$. This means that the structure functions only depends on the variable x , which also fixes the momentum fractions ξ_i . The proton structure functions can be estimated from a sum of the parton ones in eq. (1.51). Denoting $f_i(\xi_i)$ the probability to find a parton i in the proton with momentum fraction ξ_i . These functions are called parton density functions (PDFs). Integrating the PDFs over ξ_i and adding the contributions from different quark types i gives:

$$F_1(Q^2, \nu) = M_P \sum_i \int_0^1 d\xi_i f_i(\xi_i) F_1^{(i)}(Q^2, \nu) = \frac{1}{2} \sum_i e_i^2 f_i(x) \equiv F_1(x) \quad (1.52)$$

$$F_2(Q^2, \nu) = \nu \sum_i \int_0^1 d\xi_i f_i(\xi_i) F_2^{(i)}(Q^2, \nu) = x \sum_i e_i^2 f_i(x) \equiv F_2(x) \quad (1.53)$$

This simple description implies so called Bjorken scaling, the structure functions only depend on the kinematic variable x . Moreover, one gets the Callan-Gross relation:

$$F_2(x) = 2xF_1(x) \quad (1.54)$$

The combination $F_2(x) - 2xF_1(x)$ is usually called the longitudinal structure function $F_L(x)$. In the QPM $F_L(x) = 0$.

The structure function F_2 in the QPM is:

$$\frac{F_2(x)}{x} = \sum_i e_i^2 f_i(x) \quad (1.55)$$

The DIS cross section in the quark parton model, eq. (1.47), can now be expressed such that it only depends on $F_2(x)$ and not on $F_1(x)$. Using $dy^2 = dQ^2 xs$ gives:

$$\begin{aligned} \frac{d^2\sigma}{dx dQ^2} &= \frac{4\pi\alpha_{\text{EM}}^2}{Q^4} \left[y^2 F_1(x) + \frac{(1-y)}{x} F_2(x) \right] \\ &= \frac{4\pi\alpha_{\text{EM}}^2}{Q^4} \left[(1 + (1-y)^2) F_1(x) + \frac{1-y}{x} (F_2(x) - 2xF_1(x)) \right] \\ &= \frac{2\pi\alpha_{\text{EM}}^2}{Q^4} \left[(1 + (1-y)^2) \frac{F_2(x)}{x} - \frac{y^2}{x} F_L(x) \right]. \end{aligned} \quad (1.56)$$

Putting $F_L(x) = 0$, this can be rewritten in the following way:

$$\frac{d\sigma}{dx dQ^2} = \frac{\alpha_{\text{EM}}}{2\pi} \frac{1}{Q^2} (1 + (1-y)^2) \times \frac{4\pi^2 \alpha_{\text{EM}}}{Q^2} \frac{F_2(x)}{x} \quad (1.57)$$

The first half on the r.h.s. is a function only of y and the second half is a function only of x , which means that the first part may be associated with the electron side of the collision while the second half by the proton side, or with the leptonic and hadronic part respectively. This defines the so called Weizsäcker-Williams function [4, 5]:

$$yf_\gamma^e(y, Q^2) = \frac{\alpha_{\text{EM}}}{2\pi} \frac{1}{Q^2} (1 + (1-y)^2) \quad (1.58)$$

which describes the flux of photons coming from the electrons. In analogy with the parton density functions, it can be said to be the probability of finding a photon inside the electron with momentum fraction y at a scale Q^2 . With this separation it is clear that it is F_2 that carries the information about the proton.

Properties of the Parton Density Functions

The parton density functions $f_i(x)$ has the following properties: the number of partons of type i in the proton N_i can be obtained by

$$N_i = \int_0^1 d\xi_i f_i(\xi_i) \quad (1.59)$$

and the momentum fraction carried by partons of type i is given by

$$\frac{\langle p_i \rangle}{P} = \int_0^1 d\xi_i \xi_i f_i(\xi_i). \quad (1.60)$$

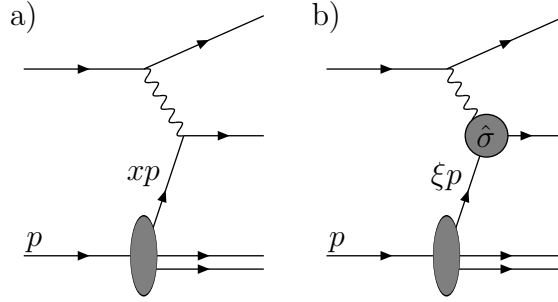


Figure 1.11: In a) the QPM picture is shown while in b) the QCD improved parton model is depicted, where $\hat{\sigma}$ symbolically means any QCD process.

It is known from that the proton consists of three valence quarks, two of which are up quarks and one which is a down quark. This leads to the flavour sum rules of the proton [3]:

$$\int_0^1 dx f_{u_V}(x) = 2 \quad (1.61)$$

$$\int_0^1 dx f_{d_V}(x) = 1 \quad (1.62)$$

$$(1.63)$$

The sum of the momenta of all quarks turns out experimentally to be

$$\sum_{q/\bar{q}} \int_0^1 dx x f_q(x) \sim 0.477 \quad (1.64)$$

This implies that less than half of the proton momentum can be explained by valence and sea quarks. Something else is needed, namely gluons, which means QCD has to be added to the DIS cross-section.

1.1.3 Adding QCD to the DIS Cross-Section

So far the inelastic scattering between an electron and a proton has been treated as a QED process. However, the valence quarks in the proton are known to interact strongly, which means that the proton also contains a gluon field. Therefore also QCD must be considered in the scope of the electron proton scattering. In fig. 1.11 a) the zeroth order QPM process is shown, which is what has been treated so far. In fig. 1.11 b) a generic QCD process is shown where one or more gluonic interaction can occur both before and after the photon interacts with a quark. The cross section $\hat{\sigma}$ is calculable with perturbative QCD.

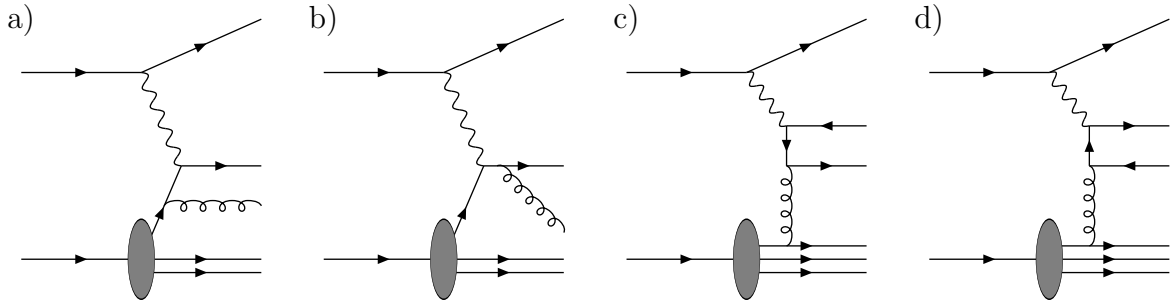


Figure 1.12: Order $\mathcal{O}(\alpha_{EM}\alpha_s)$ contributions to F_2 . In a) and b) initial and final state QCD Compton radiations are shown and in c) and d) Boson Gluon Fusion are shown.

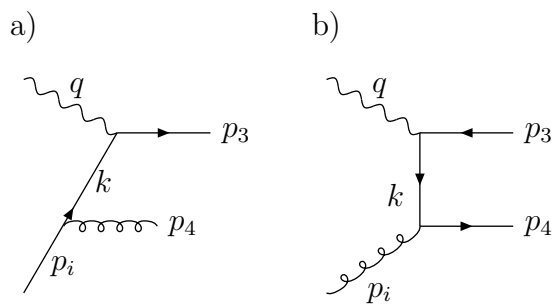


Figure 1.13: The definition of the kinematic variables for a) QCD Compton and b) boson gluon fusion.

The processes contributing to F_2 at order $\mathcal{O}(\alpha_{\text{EM}}\alpha_s)$ are depicted in fig. 1.12. When a parton is radiated by the incoming parton before the radiation, the incoming parton's momentum will be altered in the branching. In fig. 1.12 a) and b) the so called QCD Compton (QCDC) radiation processes are shown and in fig. 1.12 c) and d) the so called Boson Gluon Fusion (BGF) processes are shown. In the QCDC processes the incoming parton is a quark which interacts with the photon as before, but in the BGF processes the incoming parton is a gluon which splits up into a quark anti-quark pair which then interacts with the photon.

A parton with momentum $p_i = \xi P$ is coming into the interaction from the proton. Define $z = Q^2/(2p_i q) = x/\xi$ which is the momentum fraction of the incoming parton taken by the parton which interacts with the photon. If $f_i(\xi)$ is the probability to find parton i inside the proton with a momentum fraction ξ , the overall photon-proton cross section is a convolution of $f_i(\xi)$ and $\hat{\sigma}$:

$$\sigma(x, Q^2) = \sum_i \int_0^1 dz \int_0^1 d\xi f_i(\xi) \delta(x - z\xi) \hat{\sigma}(z, Q^2). \quad (1.65)$$

Adding the QCD Compton Process

The first addition to go beyond the QPM cross section is the QCD Compton process in figs. 1.12 a) and b). For those diagrams the parton level cross-section is [2]:

$$\hat{\sigma}_{\text{QCDC}} = \int d\Omega \frac{2}{3} \frac{e_i^2 \alpha_{\text{EM}} \alpha_s}{\hat{s}} \left[-\frac{\hat{t}}{\hat{s}} - \frac{\hat{s}}{\hat{t}} + \frac{2\hat{u}Q^2}{\hat{s}\hat{t}} \right] \quad (1.66)$$

where \hat{s} , \hat{t} and \hat{u} are the so-called Mandelstam variables defined by

$$\hat{s} = (p_i + q)^2 = Q^2 \frac{1-z}{z} \quad (1.67)$$

$$\hat{t} = k^2 = (q - p_3)^2 \quad (1.68)$$

$$\hat{u} = (q - p_4)^2 \quad (1.69)$$

where the four-momenta are defined in figure 1.13 and $z \equiv \frac{Q^2}{2p_i q}$. It should be noted that $\hat{s} + \hat{t} + \hat{u} = -3Q^2 + 2q(p_i - p' - q') = -Q^2$. In the processes in fig. 1.12 there is a virtual propagator present, with four-momentum k . The term $\propto \hat{t}/\hat{s}$ in eq. (1.66) comes from the diagram in fig. 1.12 b), the term $\propto \hat{s}/\hat{t}$ comes from the diagram fig. 1.12 a) and the third term in eq. (1.66) is the interference term between the two diagrams.

In the limit where $\hat{t} \ll \hat{s}$, i.e. the resonance where $k^2 \rightarrow 0$, the expression in square brackets in eq. (1.66) becomes:

$$-\frac{\hat{t}}{\hat{s}} - \frac{\hat{s}}{\hat{t}} + \frac{2\hat{u}Q^2}{\hat{s}\hat{t}} \approx \frac{-1}{\hat{t}} \left(\hat{s} + \frac{2(Q^2 + \hat{s})Q^2}{\hat{s}} \right) = -\frac{Q^2}{\hat{t}} \frac{1+z^2}{z(1-z)} = \frac{Q^2}{k_{\perp}^2} \frac{1+z^2}{z} \quad (1.70)$$

here k_\perp is the transverse momentum of the propagator and $k_\perp^2 = -\frac{\hat{s}t}{\hat{s}+Q^2} = -t(1-z)$. In the same approximation $d\Omega \simeq (4\pi/\hat{s})dk_\perp$. The partonic cross-section then becomes:

$$\frac{\hat{\sigma}_{\text{QCDC}}(z, Q^2)}{\hat{\sigma}_0} = \frac{e_i^2 \alpha_s}{2\pi} \frac{4}{3} \frac{1+z^2}{1-z} \int \frac{dk_\perp^2}{k_\perp^2} \equiv \frac{e_i^2 \alpha_s}{2\pi} P_{qq}(z) \int \frac{dk_\perp^2}{k_\perp^2} \quad (1.71)$$

where $\hat{\sigma}_0 = \frac{4\pi^2 \alpha_{\text{EM}}}{\hat{s}}$ and in the last step the so called splitting function $P_{qq}(z) = 4/3(1+z^2)/(1-z)$ is defined. This function is interpreted as the probability for a quark to split into a quark and a gluon where the energy fraction z is taken by the produced quark. Integrating over k_\perp^2 , with a lower cut-off $k_{\perp, \text{min}}^2 = \kappa^2$ and the upper scale $\hat{s} = Q^2(1-z)/z$ gives:

$$\begin{aligned} \frac{\hat{\sigma}_{\text{QCDC}}(z, Q^2)}{\hat{\sigma}_0} &= \frac{e_i^2 \alpha_s}{2\pi} P_{qq}(z) \int_{\kappa^2}^{Q^2(1-z)/z} \frac{dk_\perp^2}{k_\perp^2} = \frac{e_i^2 \alpha_s}{2\pi} P_{qq}(z) \ln \left(\frac{Q^2}{\kappa^2} \frac{1-z}{z} \right) \\ &= \frac{e_i^2 \alpha_s}{2\pi} \left[P_{qq}(z) \ln \left(\frac{Q^2}{\kappa^2} \right) + C(z) \right] \end{aligned} \quad (1.72)$$

where $C(z)$ include all the terms left over from the leading $\alpha_s \ln(Q^2/\kappa^2)$ term. The partonic cross section from QCDC can now be added to the QPM expression of F_2 , eq. (1.55) to give:

$$\begin{aligned} \frac{F_2(x, Q^2)}{x} &= \sum_i \int_0^1 dz \int d\xi f_i(\xi) \delta(x - z\xi) \left[e_i^2 \delta(1-z) + \frac{\hat{\sigma}_{\text{QCDC}}(z, Q^2)}{\hat{\sigma}_0} \right] \\ &= \sum_i e_i^2 \int_x^1 \frac{d\xi}{\xi} f_i(\xi) \left[\delta \left(1 - \frac{x}{\xi} \right) + \frac{\alpha_s}{2\pi} P_{qq} \left(\frac{x}{\xi} \right) \ln \left(\frac{Q^2}{\kappa^2} \right) + \dots \right] \end{aligned} \quad (1.73)$$

where only the leading term in $\alpha_s \ln(Q^2/\kappa^2)$ is kept.

This equation can be interpreted as a redefinition of the quark densities $f_i(x)$ in the QPM such that

$$f_i(x, Q^2) = f_i^{\text{QPM}}(x) + f_i^{\text{QCDC}}(x, Q^2), \quad (1.74)$$

where

$$f_i^{\text{QCDC}}(x, Q^2) = \frac{\alpha_s}{2\pi} \int_z^1 \frac{d\xi}{\xi} P_{qq} \left(\frac{x}{\xi} \right) \ln \left(\frac{Q^2}{\kappa^2} \right). \quad (1.75)$$

In this formulation the parton densities depend strongly on an arbitrary cut-off κ^2 . This cut-off has to do with the collinear singularity in the partonic cross-section. It's easy to understand that a cut-off is needed, since small k_\perp^2 corresponds to large wave-length, and the wave-length of the interacting partons should not be much longer than the size of the proton. The solution is similar to that of renormalization. The quark distribution $f_i(x)$ is the bare distribution which includes scales which are not measurable. By introducing a new scale $\mu_F^2 \gg \kappa^2$ the soft non-perturbative physics gets absorbed into the renormalized

scale dependent parton density $f_i(x, \mu_F^2)$. This is the collinear factorization scale at which the collinear singularity is absorbed into the parton density, such that

$$\ln\left(\frac{Q^2}{\kappa^2}\right) = \ln\left(\frac{Q^2}{\mu_F^2}\right) + \ln\left(\frac{\mu_F^2}{\kappa^2}\right) \quad (1.76)$$

The parton density then becomes:

$$f_i(x, \mu_F^2) = f_i^{\text{QPM}}(x) + \frac{\alpha_s}{2\pi} \int_z^1 \frac{d\xi}{\xi} f_i^{\text{QPM}}(x) P_{qq}\left(\frac{x}{\xi}\right) \ln\left(\frac{Q^2}{\kappa^2}\right) \quad (1.77)$$

Then F_2 becomes:

$$\begin{aligned} \frac{F_2(Q^2, \mu_F^2, x)}{x} &= \sum_i e_i^2 \int_x^1 \frac{d\xi}{\xi} f_i(\xi, \mu_F^2) \times \\ &\quad \left[\delta\left(1 - \frac{x}{\xi}\right) + \frac{\alpha_s}{2\pi} P_{qq}\left(\frac{x}{\xi}\right) \ln\left(\frac{Q^2}{\mu_F^2}\right) + \frac{\alpha_s}{2\pi} C\left(\frac{x}{\xi}\right) \right] \end{aligned} \quad (1.78)$$

If one chooses as factorization scale $\mu_F^2 = Q^2$ and let the terms $C(z)$ be absorbed into the definition of the renormalized parton density (which is a procedure called the DIS factorization scheme), then this expression reduces to

$$F_2^{\text{DIS}}(x, Q^2) = \sum_i e_i^2 x f_i^{\text{DIS}}(x, Q^2) \quad (1.79)$$

which is the same as the QPM result eq. (1.55) but with a dependence on Q^2 . Another choice would be to absorb as little as possible of the $C(z)$ into the parton densities, such that:

$$F_2^{\text{MS}}(x, Q^2) = x \sum_i e_i^2 \int \frac{d\xi}{\xi} f_i^{\text{MS}}(x, Q^2) \left[\delta\left(1 - \frac{x}{\xi}\right) + \frac{\alpha_s}{2\pi} C^{\text{MS}}\left(\frac{x}{\xi}\right) + \dots \right] \quad (1.80)$$

which is called the Minimum Subtraction ($\overline{\text{MS}}$) scheme. The scheme one chooses is arbitrary, but once a scheme is chosen the same scheme has to be kept throughout the calculation.

Adding the Boson Gluon Fusion Process

The next addition which can be made to the QPM cross-section is that of Boson Gluon Fusion depicted in figs. 1.12 c) and d). BGF is added to the QPM in a similar way as the QCDC. The partonic cross-section for these processes is [2]:

$$\hat{\sigma}_{\text{BGF}} = \int d\Omega \frac{1}{4} \frac{e_i^2 \alpha_{\text{EM}} \alpha_s}{\hat{s}} \left[\frac{\hat{u}}{\hat{t}} + \frac{\hat{t}}{\hat{u}} - \frac{2\hat{s}Q^2}{\hat{t}\hat{u}} \right] \quad (1.81)$$

where the term proportional to \hat{u}/\hat{t} comes from the diagram in fig. 1.12 c), the term proportional to \hat{t}/\hat{u} comes from fig. 1.12 d) and the third term comes from the interference between the two diagrams. As for QCDC, taking the small \hat{t} limit and expressing the cross-section as a function of k_{\perp}^2 one gets:

$$\frac{\hat{\sigma}_{BGF}(z, Q^2)}{\hat{\sigma}_0} = \frac{e_i^2 \alpha_s}{2\pi} \frac{1}{2} [z^2 + (1-z)^2] \int \frac{dk_{\perp}^2}{k_{\perp}^2} \quad (1.82)$$

Defining the splitting function $P_{qg}(z)$ as the probability of a gluon splitting into a quark anti-quark pair where one of the produced partons take the momentum fraction z as

$$P_{qg} = \frac{1}{2} [z^2 + (1-z)^2]. \quad (1.83)$$

Also, as before for QCDC, introduce a soft cut-off κ^2 for small k_{\perp}^2 and a gluon distribution in the proton, $f_g(x)$, then introducing a collinear factorization scale μ_F^2 one obtains for F_2 :

$$\frac{F_2^g(x, Q^2)}{x} = \sum_i \int_x^1 \frac{d\xi}{\xi} e_i^2 f_g(\xi) \left[\frac{\alpha_s}{2\pi} P_{qg} \left(\frac{x}{\xi} \right) \ln \left(\frac{Q^2}{\mu_F^2} \right) + \frac{\alpha_s}{2\pi} D \left(\frac{x}{\xi} \right) \right] \quad (1.84)$$

which is a piece that should be added to the F_2 of QPM and QCDC. It should be noted that with the splitting of the gluon into a quark-antiquark pair, the BGF processes are also contributing to the quark densities $f_i(x, Q^2)$, such that

$$f_i(x, \mu_F^2) = f_i^{\text{QPM}}(x) + \frac{\alpha_s}{2\pi} \int_z^1 \frac{d\xi}{\xi} \left[f_i^{\text{QPM}}(x) P_{qg} \left(\frac{x}{\xi} \right) + f_g(x, \mu_F^2) P_{qg} \left(\frac{x}{\xi} \right) \right] \ln \left(\frac{Q^2}{\mu_F^2} \right) \quad (1.85)$$

1.1.4 The DGLAP equations

The benefit of introducing the collinear factorization scale μ_F^2 is that it is an effective way to get rid of the collinear singularities, and also in a natural way take away the dependence on the very soft scale κ . But μ_F^2 is still not a physical quantity, and the total cross-section, or F_2 should not depend upon any unphysical scales. Therefore should the following hold:

$$\frac{\partial F_2(x, \mu_F^2)}{\partial \ln \mu_F^2} = 0. \quad (1.86)$$

To perform this derivative, one needs to derivate the parton density functions which leads to a set of coupled differential equations of the quark and gluon densities. These equations are called the DGLAP evolution equations after the physicists that developed them: Dokshitzer, Gribov, Lipatov, Altarelli and Parisi [6, 7, 8, 9]. The equations become:

$$\frac{\partial f_i(x, \mu_F^2)}{\partial \ln \mu_F^2} = \frac{\alpha_s}{2\pi} \sum_i \int_x^1 \frac{d\xi}{\xi} \left[f_i(\xi, \mu_F^2) P_{qq} \left(\frac{x}{\xi} \right) + f_g(\xi, \mu_F^2) P_{qg} \left(\frac{x}{\xi} \right) \right] \quad (1.87)$$

$$\frac{\partial f_g(x, \mu_F^2)}{\partial \ln \mu_F^2} = \frac{\alpha_s}{2\pi} \sum_i \int_x^1 \frac{d\xi}{\xi} \left[f_i(\xi, \mu_F^2) P_{gq} \left(\frac{x}{\xi} \right) + f_g(\xi, \mu_F^2) P_{gg} \left(\frac{x}{\xi} \right) \right] \quad (1.88)$$

These equations provide the mathematical formalism for the pictorial view of the proton given in the introduction of this chapter. Before the interaction, the (not yet) struck quark or anti-quark is surrounded by a cloud of virtual partons constantly being emitted and re-absorbed. These particles may in their turn emit and absorb particles. The larger the scale Q^2 of the interaction, the more of these partons may be resolved. Therefore the probability of interacting with a parton i changes with the scale Q^2 . It is this evolution which is shown in eqs. (1.87) and (1.88). At low values of Q^2 not many partons can be resolved and the proton is expected to consist mostly of the valence quarks. These are then expected to carry large fractions of the proton's momentum $x \sim 1/3$. As Q^2 increases more and more particles may be resolved and the momentum of the proton is spread over more particles via parton branchings which are represented by the splitting functions in the DGLAP equations. Therefore the small x part of the PDFs are expected to grow with Q^2 . Many of these small x partons are expected to be gluons originating mainly from $g \rightarrow gg$ branchings and sea-quarks coming from $g \rightarrow q\bar{q}$ branchings. During this process it is important to respect the momentum sum rule:

$$1 = \int_0^1 dx x \left[f_g(x) + \sum_i f_i(x) \right]. \quad (1.89)$$

How to calculate the evolution from a small scale $\mu_0 \sim \Lambda_{\text{QCD}}$ to a large scale $\mu_F \sim Q^2$ is shown in eqs. (1.87) and (1.88). However, these equations need an input in the form of initial parton densities $f(x, \mu_0)$. These are non-perturbative and cannot be calculated. Instead they have to be guessed. They are usually obtained by a parametrized form and are then evolved through eqs. (1.87) and (1.88) and fitted to experimental data taken at different x and Q^2 . These are then treated as universal, i.e. they can be used in any calculation using the DGLAP equations with protons.

How to solve the DGLAP equations in detail, using Sudakov form factors will be explained in chapter 2. This is one of many ways to solve the equations.

Properties of the DGLAP Splitting Functions

Some comments on the properties of the DGLAP splitting functions are needed. The splitting functions are [3]:

$$\begin{aligned} P_{qq}(z) &= \frac{4}{3} \frac{1+z^2}{1-z} \\ P_{gq}(z) &= P_{qg}(1-z) \\ P_{qg}(z) &= \frac{1}{2} (z^2 + (1-z)^2) \\ P_{gg}(z) &= 6 \left(\frac{1-z}{z} + \frac{z}{1-z} + z(1-z) \right) \end{aligned} \quad (1.90)$$

The splitting functions are interpreted as probability distribution functions, such that the function $P_{ji}(z)$ gives the probability of finding parton j inside parton i with momentum

fraction z . However, some of these are not regular for all values of z . To still be able to interpret the splitting functions as a distribution the so called plus-prescription is introduced for the splitting functions with a $1/(1-z)$ pole, defined by:

$$\int_0^1 dz \frac{f(z)}{(1-z)_+} = \int_0^1 dz \frac{f(z) - f(1)}{1-z} \quad (1.91)$$

The splitting functions do by unity include virtual contributions. This can be understood since the splitting functions should not affect the total cross-section. The probability of finding a quark inside of a quark should be equal to 1. Therefore the extra contribution coming from the radiation of an extra parton must be compensated by a virtual contribution in the splitting. Hence, the one loop splitting functions are given by:

$$P(z) \rightarrow P(z) + K_{ij}\delta(1-z) \quad (1.92)$$

where the delta function represents the probability of leaving the splitting parton unchanged. K_{ij} is a constant which can be determined by the rules for conservation of flavour:

$$\begin{aligned} 0 &= \int_0^1 P_{qq}(z) dz = \int_0^1 \left(\frac{4}{3} \frac{1+z^2}{(1-z)_+} + K_{qq}\delta(1-z) \right) dz \\ &= \int_0^1 \frac{4}{3} \frac{z^2-1}{1-z} dz + K_{qq} = K_{qq} - 2 \end{aligned} \quad (1.93)$$

Hence is the factor $K_{qq} = 2$. Similarly, for $P_{gg}(z)$:

$$0 = \int_0^1 P_{gg}(z) dz = \int_0^1 6 \left(\frac{1-z}{z} + \frac{z}{(1-z)_+} + z(1-z) \right) + K_{gg}\delta(1-z) \quad (1.94)$$

gives $K_{gg} = (33 - 2n_f)/6$ where n_f is the number of active quark flavours. The one-loop splitting functions then are:

$$\begin{aligned} P_{qq}^{(1)}(z) &= \frac{4}{3} \frac{1+z^2}{(1-z)_+} + 2\delta(1-z) \\ P_{gg}^{(1)}(z) &= 6 \left[\frac{z}{(1-z)_+} + \frac{1-z}{z} + z(1-z) \right] + \frac{33-2n_f}{6} \delta(1-z) \end{aligned} \quad (1.95)$$

1.1.5 Heavy Quarks in Photoproduction

So far in this chapter all partons has been treated in the relativistic limit where their masses become negligible, or rather when $4m^2 \ll \hat{s}$ such that the velocity function

$$\beta = \sqrt{1 - \frac{4m^2}{\hat{s}}} \approx 1. \quad (1.96)$$

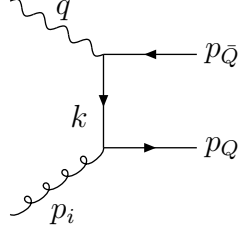


Figure 1.14: In photoproduction heavy quarks are produced by photon gluon fusion.

At HERA energies, this is mostly true for up, down and strange quarks but not necessarily true for charm, beauty and top quarks. Since the heavy quarks are not valence quarks in the proton it is assumed that the PDFs fulfill $f_Q(x, Q^2) = f_{\bar{Q}}(x, Q^2)$ where the subscript Q denotes any heavy quark. There are several approaches to include heavy quarks in the DGLAP framework. Three of them are:

1. The Zero Mass Variable Flavour Scheme (ZM-VFS), where the heavy quark density $f_Q(x, Q^2) = 0$ for $Q^2 < \mu_Q^2$ and the number of quark flavours are $n_l + \theta(Q^2 - \mu_Q^2)$ where n_l denotes the number of quark flavours with masses smaller than m_Q . Here the threshold $m_Q^2 < \mu_Q^2 < 4m_Q^2$ is a parameter which has to be fitted to measurements. The advantage of this scheme is that it provides a minimal alteration of the DGLAP approach, where the heavy quarks may be produced in a splitting during the evolution. The disadvantage is that the physical threshold $\hat{s} \geq 4m_Q^2$ is not treated correctly.
2. The Fixed Flavour Number Scheme (FFNS), where all the heavy quarks are produced dynamically, at leading order in the boson gluon fusion process. In the FFNS $f_Q(x, Q^2) = 0$ for all Q^2 . The physical threshold is treated correctly in the FFNS but to the price of large $\ln(Q^2/m_Q^2)$ terms in the evolution.
3. The Variable Flavour Number Scheme (VFNS), which is an interpolation between the FFNS at low Q^2 and the ZM-VFNS at large Q^2 . In this approach the physical threshold is treated correctly with the possibility of finite heavy quark PDFs at large Q^2 .

In eq. (1.56) it is seen that the eP cross-section is $\propto 1/Q^4$. It is therefore dominated by small Q^2 . The kinematic regime where the incoming photon is quasi real, i.e. when $Q^2 \simeq 0$ is called photoproduction. In photoproduction the FFNS is the natural choice to include heavy quarks into the DGLAP formalism. The BGF cross-section in eq. (1.81) has to be altered to include the mass of the heavy quark and the quasi real photon. It is

convenient to modify the Mandelstam variables for heavy quarks in the following way:

$$\begin{aligned}\tilde{u} &= \hat{u} - m_Q^2 \\ \tilde{t} &= \hat{t} - m_Q^2\end{aligned}\tag{1.97}$$

such that $\hat{s} + \tilde{t} + \tilde{u} = 0$. The partonic cross-section for BGF producing heavy quarks in photoproduction then becomes [10]:

$$\begin{aligned}\frac{\hat{\sigma}_{FFNS}}{\hat{\sigma}_0} &= \int d\Omega \frac{e_i^2 \alpha_s}{2\pi} \frac{1}{\tilde{t}\tilde{u}} \left[\tilde{u}^2 + \tilde{t}^2 + 4m_Q^2 \hat{s} \left(1 - \frac{m^2 \hat{s}}{\tilde{t}\tilde{u}} \right) \right] \\ &\approx \int d\Omega \frac{e_i^2 \alpha_s}{2\pi} \left[1 - (1 - \beta^2) \left(1 + \frac{m_Q^2}{4\tilde{t}} \right) \right] \\ &\approx \frac{2e_i^2 \alpha_s}{\pi} (1 - z) \int_0^{\hat{s}} \frac{dk_{\perp}^2}{(k_{\perp}^2 + m_Q^2)} \left[1 - (1 - \beta^2) \left(1 + \frac{m_Q^2}{4\tilde{t}} \right) \right]\end{aligned}\tag{1.98}$$

Here $\tilde{t} = -(m_Q^2 + k_{\perp}^2)(1 - z)$ and β is the velocity of the heavy quark defined in eq. (1.96). In the first step the small \tilde{t} limit has been taken, which corresponds to $k^2 = m_Q^2$ being the mass resonance of the propagator. In the second step $d\Omega \approx (4\pi/\hat{s})dk_{\perp}$. The mass term in the denominator in the last step means that the partonic cross-section does not diverge for $k_{\perp}^2 \rightarrow 0$, but rather peaks at $k_{\perp}^2 = m_Q^2$ and no cut-off κ is needed. The upper scale is still given by $\hat{s} = xys$.

Chapter 2

Monte Carlo Techniques and the HERWIG Event Generator

When an electron and a proton collide in an accelerator, the collision can produce tens or even hundreds of particles, some of which are measured in the detectors surrounding the beam-pipe at the interaction point. At HERA there are two such experiments, H1 and ZEUS. In order to make sense of the large quantities of data from the detectors one needs a detailed theoretical understanding of the interactions. However, using theory from first principle, to explain the measurements leads to highly nonlinear equation systems, which are impossible to solve analytically. Also, only the perturbative part of the theory is even in principle calculable from first principle, the non-perturbative part is not. Instead it is necessary to make approximations and to build models that describe the physics at hand. These models then have to be compared to the data. If they manage to describe some of the data it means that at least a part of the measurement is understood. Also, no model is perfect, they always contain parameters, and these parameters have to be adjusted and fitted to measured data, which means that the theoretical prediction always comes with an uncertainty band. However, there are no perfect measurements either, and they too come with experimental uncertainties. This implies that the theoretical understanding should be at a similar level as the experimental understanding of the measured data.

When an electron and a proton collide in the detector, the event enters two phases of transition, a perturbative and a hadronization phase, as depicted in fig. 2.1. The perturbative phase is governed by short distances, up to roughly the size of the proton, which means that most of this phase takes place inside the proton that takes part in the interaction. In the perturbative phase all partons are treated as free particles, which is possible through asymptotic freedom. The hadronization phase is governed by longer distances, which is where the asymptotic freedom breaks down. The partons can no longer be treated as free particles and must instead somehow get trapped in colour-singlet states, i.e. in hadrons. The end result of a realistic simulation of high energy physics events are always hadrons, leptons and electroweak bosons, since these are the only particles detected in

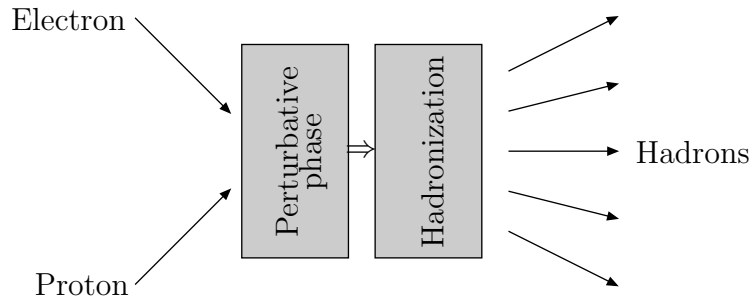


Figure 2.1: When an electron and a proton collide at HERA, many hadrons are created. The intermediate states may be divided into a perturbative phase and a soft hadronization phase.

the experiments.

In order to simulate these events, all the applicable phenomenological models available are collected in computer programs called Monte Carlo (MC) event generators. The purpose of this chapter is to describe how MC event generator works. In chapter 1, the structure of the proton, when probed by a virtual photon, was described. This was illustrated in fig. 1.3. In fig. 2.2, the same picture is shown, but with the different parts of an MC simulation included. Instead of starting with the proton, and evolving to the hard interaction, an MC program starts with the hard interaction, by calculating a matrix element (ME) from first principle in perturbative QCD, as indicated in the figure. From these particles, the initial state radiations are simulated backwards in time in the initial state partons shower, down to a cut-off virtuality close to Λ_{QCD} . The parton propagator left at this scale has to be taken from the proton PDF at the cut-off scale. The parton showers will be described in section 2.2. It is performed with splitting functions, describing the probability of one particle splitting into two particles (or in some parton showers the probability of two particles splitting into three). Then, all produced partons are made to radiate bremsstrahlung in the final state parton shower, until another cut-off scale is reached. At this scale, the partons enter the hadronization phase of transition, where they are confined in hadrons. How this is modeled will be explained in section 2.4. The distributions of energies, momenta and other properties of these hadrons may then be filled in histograms which can be compared to measurements. One ingredient in the calculation which is not depicted in fig. 2.2 is the inclusion of unstable particles. There are partons which decay before they can hadronize, such as the top quark, and there are hadrons that decay before they can be detected, such as B-hadrons. These decays must also be modeled and included into the calculation.

All of the elements in fig.2.2 are modeled in different ways, and in order to receive an answer from the calculation which makes sense, all the different parts have to be well fitted together, they have to be matched.

In fig. 2.2, one of the main approximations made is that most of the quantum interference effects are ignored. Instead of adding probability amplitudes, probabilities are added.

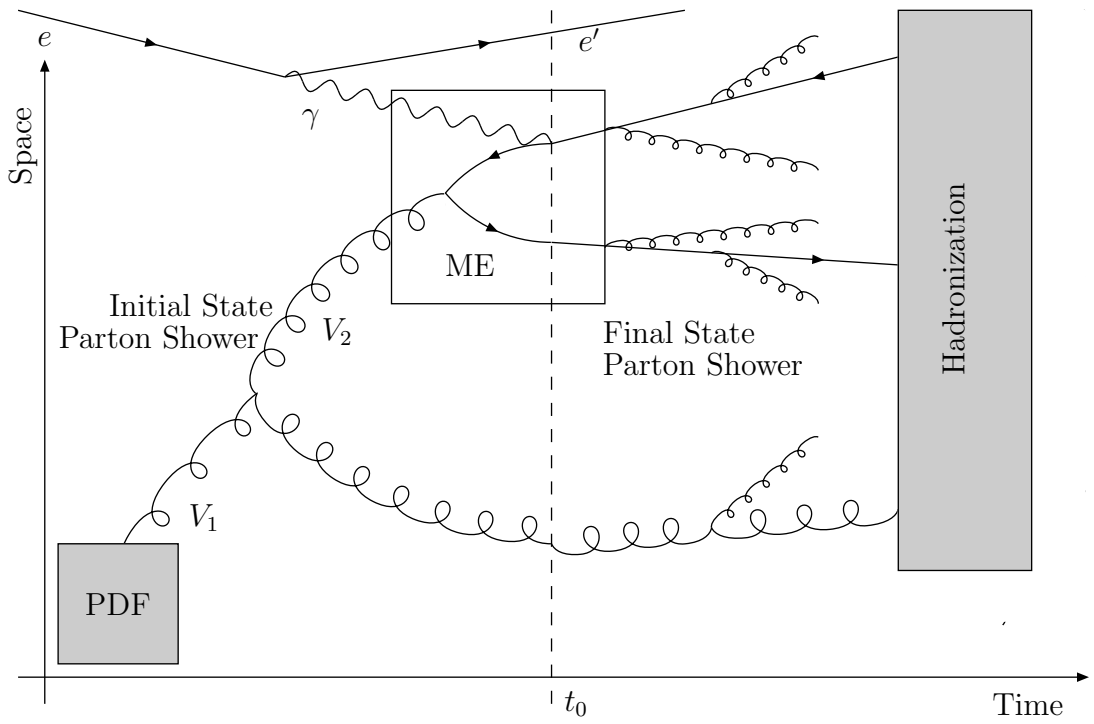


Figure 2.2: The same figure as in fig. 1.2, but with the different parts of a Monte Carlo event generator also in it, as explained in the text.

This is acceptable, if the errors it leads to are small enough, compared to the experimental uncertainties. But, the longer new data is collected, the better will the statistical precision¹ of the measurement become which raises the demands on the theoretical predictions and models. This thesis is about improving the precision in one Monte Carlo event generator, namely HERWIG, by inclusion of more interference effects in the matrix element part of the calculation by the technique of MC@NLO. How this is done will be explained in later chapters.

In this chapter, before going through all the elements depicted in fig. 2.2, what is meant by the Monte Carlo method of integration will first be explained in section 2.1. In section 2.2 it will be described how the theory of DGLAP evolution in chapter 1 is implemented in a Monte Carlo event generator. Also the models of hadronization will be briefly described in section 2.4. In section 2.3 the HERWIG Monte Carlo event generator will be described.

2.1 Monte Carlo Integration

When calculating a high energy physics event, e.g. the one depicted in fig. 2.2, the expectation value for an observable \mathcal{O} is the evaluation of the integral:

$$\begin{aligned} \langle \mathcal{O} \rangle = & \sum_{n_k, \mathbf{Q}_k} \int d^{4n_k} \mathbf{q} |\mathcal{M}_{n_q}(\mathbf{Q}_q, \mathbf{q})|^2 \phi_{n_q}(\mathbf{q}) \\ & \times \left[\sum_{n_k, \mathbf{Q}_k} \int d^{4n_k} \mathbf{k} PS(\mathbf{Q}_q, \mathbf{q}; \mathbf{Q}_k, \mathbf{k}) \right. \\ & \left. \times \left[\sum_{n_p, \mathbf{Q}_p} \int d^{4n_p} \mathbf{p} H(\mathbf{Q}_k, \mathbf{k}; \mathbf{Q}_p, \mathbf{p}) \mathcal{O}_{n_p}(\mathbf{Q}_p, \mathbf{p}) \right] \right], \end{aligned} \quad (2.1)$$

where \mathcal{M} stands for the matrix element which produces n_q partons, ϕ is the invariant phase space, PS is the parton shower, which produces additionally n_k partons and H is the hadronization which brings the partons into an hadronic final state containing n_p hadrons, which are observable. As seen in eq. (2.1) each particle adds another four dimensions to the integration, which means that this integral can have a large number of dimensions. Also, the integrated functions can be very complicated. In general it is not possible to compute the integral in eq. (2.1) analytically. Also, to simulate the events in the accelerator one needs to be able to generate random events one by one.

The most commonly used method to compute the integral eq. (2.1) is the so called Monte Carlo method of integration. It is a method that uses random numbers and probability distributions which makes it very well suited for generating physics events, since quantum mechanics includes in itself randomness and what is measured in experiments are distributions. The purpose of using random numbers is two-fold. For one, random numbers

¹At some point systematical uncertainties become more important than the statistical ones.

are used to estimate an integral, for example the total rate of a process, but it is also used to generate events one at a time.

Averaged Sums

A straight forward approach to evaluate an integral is to use an averaged sum. An estimate of the integral

$$I = \int_a^b dx f(x) \quad (2.2)$$

may be obtained by

$$I = \int_a^b dx f(x) \approx \sum_i^N f(x_i) \Delta x = (b-a) \frac{1}{N} \sum_i^N f(x_i). \quad (2.3)$$

Here the x_i 's have to be uniformly distributed. They may be chosen randomly according to a distribution, but this is not necessary, since it would also work to chose them e.g. at fixed intervals. When $N \rightarrow \infty$ this is an exact solution by the law of large numbers. This can be generalized for any dimension

$$\begin{aligned} I &= \int_{\Omega} d^m \mathbf{x} f(\mathbf{x}) = \int_{a_1}^{b_1} \dots \int_{a_m}^{b_m} dx_1 \dots dx_m f(x_1, \dots, x_m) \\ &\approx \frac{(b_1 - a_1) \dots (b_m - a_m)}{N^m} \sum_{k_1=1}^N \dots \sum_{k_m=1}^N f(x_{1k_1}, \dots, x_{mk_m}) \end{aligned} \quad (2.4)$$

For this estimate to be good N has to be a very large number in general. One may choose the numbers \mathbf{x} in any way such that they are uniformly distributed. A convenient way to do this is to choose the numbers randomly from a uniform distribution. This has several advantages as will be seen later, but an obvious advantage is that one can estimate the integral with a certain number of randomly chosen \mathbf{x} values and if the result is not satisfactory good one can simply produce more randomly chosen \mathbf{x} values to improve the estimate. To do this one needs to be able to generate random numbers. In each Monte Carlo program there is a routine that generates pseudo random numbers R such that:

$$\begin{aligned} p_R(r) &= 1, \text{ when } 0 \leq r \leq 1 \\ p_R(r) &= 0, \text{ otherwise} \end{aligned} \quad (2.5)$$

These are called pseudo random numbers, since the numbers are not absolutely uncorrelated. Given a value R generated from $p_R(r)$ a value x may be uniformly distributed on a range $[x_1, x_2]$ by $x = R(x_2 - x_1)$. For a random number generator to be good the produced numbers have to be uniformly distributed and uncorrelated. It will be assumed that a sufficiently good such generator is available in the following.

Importance Sampling

When the integrand varies rapidly over the integration range the method in eq. (2.4) is very inefficient, in the sense that N then has to be a very large number for the integral to be reasonably well estimated. In this case a more efficient way to estimate the integral is so called importance sampling. Assume that it is possible to generate variables \mathbf{x}_i on Ω according to a probability distribution function $p(\mathbf{x})$. The integral can then be written as:

$$I = \int_{\Omega} d^m \mathbf{x} f(\mathbf{x}) = \int_{\Omega} d^m \mathbf{x} \frac{f(\mathbf{x})}{p(\mathbf{x})} p(\mathbf{x}) \equiv \left\langle \frac{f(\mathbf{x})}{p(\mathbf{x})} \right\rangle \quad (2.6)$$

where in the last step the definition of an expectation value has been used, where the function $p(\mathbf{x})$ is interpreted as a probability density function. This is a generalization of eq. (2.3) which is the case when $p(x)$ is a flat distribution in one dimension.

The law of large numbers says that the estimate of the integral approaches the correct value as the number N approaches infinity [11], but it does not give a hint of how close to the true value an estimate is for finite N . The central limit theorem states that the sum of a large number of independent random variables will have a Gaussian distribution. This means that the error one gets with such an estimation is given by [11]:

$$\delta \approx \frac{\sigma \left(\frac{f(\mathbf{x})}{p(\mathbf{x})} \right)}{\sqrt{N}} \quad (2.7)$$

where the variance σ is given by:

$$\sigma^2 \left(\frac{f(\mathbf{x})}{p(\mathbf{x})} \right) = \left\langle \left(\frac{f(\mathbf{x})}{p(\mathbf{x})} \right)^2 \right\rangle - \left\langle \left(\frac{f(\mathbf{x})}{p(\mathbf{x})} \right) \right\rangle^2 \quad (2.8)$$

The task then becomes finding an appropriate function $p(\mathbf{x})$ such that the error in the estimate becomes as small as possible. It is clear that a choice $p(\mathbf{x}) = c|f(\mathbf{x})|$ for a constant c gives the smallest possible error, but then the estimate of the integral becomes just as hard to compute as the integral itself. When an appropriate function $p(\mathbf{x})$ is found one can evaluate the integral by the following steps:

1. Find a function $p(\mathbf{x})$ which is similar to $f(\mathbf{x})$.
2. Rewrite the integrand $f(\mathbf{x})d^m \mathbf{x} = \frac{f(\mathbf{x})}{p(\mathbf{x})}p(\mathbf{x})d^m \mathbf{x}$.
3. Perform a variable substitution $d^m \mathbf{y} = p(\mathbf{x})d^m \mathbf{x}$.
4. Set $h(\mathbf{y}) = f(\mathbf{x})/p(\mathbf{x})$ such that $f(\mathbf{x})d^m \mathbf{x} = h(\mathbf{y})d^m \mathbf{y}$.

If p is a good approximation of f , then the function h will not vary much over the interval Ω and the integral can be estimated with good precision using eq. (2.4).

As a simple example, consider the function $f(x) = 1/x^{0.7}$ as the function to be estimated on the interval $[\epsilon : 1]$ where $0 < \epsilon \ll 1$. Then the steps above become:

1. Choose $p(x) = \frac{1}{x}$.
2. $f(x)dx = \frac{f(x)}{p(x)}p(x)dx = x^{0.3} \left(\frac{1}{x}dx\right)$.
3. Substitute $dy = \frac{1}{x}dx = d \ln(x)$, such that $x = e^y$.
4. Set $h(y) = f(x)/p(x) = x^{0.3} = e^{0.3y}$ such that $f(x)dx = e^{0.3y}dy$.

Where the function $f(x)$ varies rapidly for small x the function $h(y)$ does not.

2.1.1 Selection From a Distribution

Often one wants to generate a set of variables \mathbf{x} according to the distribution $f(\mathbf{x})$ as well as evaluating the integral of $f(\mathbf{x})$. For example $f(\mathbf{x})$ could be the matrix element $\mathcal{M}_{n_q}(\mathbf{Q}_q \mathbf{q})$ in eq. (2.1) and one would like to generate the p_{\perp} distribution of the radiated partons as well as estimate the full integral. It is possible to obtain values \mathbf{x} from f using a pseudo random number generator. To make the notation simpler, the one dimensional case will be considered, but it is easily generalized to any number of dimensions. To generate a value x according to $f(x)$ one can use uniformly and randomly distributed numbers $R \in [0 : 1]$ and solve the following equation for x :

$$\int_{x_{\min}}^x f(\hat{x})d\hat{x} = R \int_{x_{\min}}^{x_{\max}} f(\hat{x})d\hat{x}, \quad (2.9)$$

this means that a fraction R of the total area under $f(x)$ should be to the left of x . The solution is:

$$x = F^{-1} (F(x_{\min}) + R(F(x_{\max}) - F(x_{\min}))). \quad (2.10)$$

To solve this equation one needs to know both the primitive function $F(x)$ and its inverse $F^{-1}(x)$, which is a very rare scenario.

If these properties of $f(x)$ are not known, a so called hit and miss scheme may be adopted instead. If f has a known maximum $f_{\max} \geq f(x)$ in the considered x range, then one can generate x according to $f(x)$ by the following scheme:

1. Select an x value with an uniform probability over the range, i.e.
 $x = x_{\min} + R_1(x_{\max} - x_{\min})$

2. Compare another random number R_2 with the ratio $f(x)/f_{\max}$.
 If $\frac{f(x)}{f_{\max}} \leq R_2$ reject the x value and return to 1.
 Otherwise, the most recent value is kept as the generated x

It is easy to see that this gives the correct distribution, since the probability that $f(x)/f_{\max} > R_2$ is proportional to $f(x)$. The efficiency of this method, i.e. the average probability that an x value will be kept is

$$\frac{\int f(x)dx}{f_{\max} \cdot (x_{\max} - x_{\min})} \quad (2.11)$$

which is only large when f does not vary much over the interval. Often, this is not the case however, $f(x)$ may have narrow spikes or even singularities just outside the range. Then the hit and miss method may be refined by using importance sampling. To do this one needs to find a function $g(x)$ with the properties that $g(x) \geq f(x)$ over the interval and $G(x)$ and $G^{-1}(x)$ are known. Then one can obtain a value x from $f(x)$ in the following way:

1. Select a value x from $g(x)$ using eq. (2.10)
2. Compare a random number R with the ratio $f(x)/g(x)$,
 If $\frac{f(x)}{g(x)} \leq R$ reject the x value and return to 1.
 Otherwise, the most recent value is kept as the generated x

In the first step, an x is selected with the probability $g(x)dx$, and in the second step this is kept with the probability $f(x)/g(x)$ such that the total probability of keeping the generated x value is $f(x)dx$. This scheme will be efficient as long as $f(x)/g(x)$ does not vary too much over the interval.

2.2 Generating Parton Showers

The purpose of a parton shower is to generate real exclusive events on parton level down to an almost non-perturbative scale. In section 2.2.2 it will be shown that the parton shower approach will reproduce the DGLAP equations described in chapter 1.1.4. There are other approaches towards generating multi parton final states. One example is tree-level generators, but those will only produce events to a given order. Also NLO generators may give exclusive events, but those will only give a few extra partons.

The tree-level matrix element for an n -parton state can be approximated by a product of splitting functions, which corresponds to a sequence of one-parton emissions from the zeroth order state. In fig. 2.2 there is not entirely clear which happens when, i.e. which element in the picture happens first, and then next and so on. In principle many of these radiations could occur simultaneously in a given Lorentz frame. When simulating parton

showers in a computer program, two emissions cannot be simulated simultaneously due to the linearity of the code. Instead some sort of 'time' ordering is necessary, by which the subsequent emissions are simulated in the code. The choice of a time scale t is somewhat arbitrary and different Monte Carlo event generators adopt different choices. It should be noted that in an event generator there are two kinds of ordering. What has been described here is the order in which partons are radiated within the algorithm. For the parton dynamics however, it is more interesting how the radiated partons are ordered in colour. Often these two orderings coincide in MC event generation, but this is not always the case. For example in the Colour Dipole Model as implemented in ARIADNE[12] the radiations are generated ordered in their transverse momentum (p_\perp), but the colour ordering is uncorrelated with the p_\perp ordering, whereas in PYTHIA [13] the partons are both generated in a p_\perp order and are also colour ordered in p_\perp . A good choice of time will leave the colour-ordering of the emission unchanged under a Lorentz transformation.

As a simple example, the choice of 'time' parameter may be

$$t = \ln \left(\frac{p_\perp^2}{p_{\perp,\min}^2} \right) \quad (2.12)$$

such that

$$dt = d \ln(p_\perp^2) = \frac{dp_\perp^2}{p_\perp^2} \quad (2.13)$$

where p_\perp is the transverse momentum of the emitting parton when it radiates. This can be seen as similar to a real concept of time ordering, since the harder radiations typically occur during shorter time scales, but it should be noted that it is just a choice of in which order the radiations are simulated. In the following t will not be further specified, and could in principle mean any ordering.

In each radiation in the parton shower a mother particle a will branch into two particles b and c . Particle b takes an energy-momentum fraction z from the mother particle a and particle c takes a fraction $1 - z$. In terms of the two variable t and z , the differential probability of having such a branching of particle a is:

$$d\mathcal{P}_a = \sum_b \frac{\alpha_s}{2\pi} P_{ba}(z) dt dz \quad (2.14)$$

where the sum runs over all allowed branchings, e.g. for a quark $q \rightarrow qg$. The DGLAP splitting functions are given in eqs. (1.90), but may be summarized once more:

$$\begin{aligned} \hat{P}_{gg}(z) &= 6 \left[\frac{1-z}{z} + \frac{z}{1-z} + z(1-z) \right] \\ \hat{P}_{qg}(z) &= \frac{1}{2} [z^2 + (1-z)^2] \\ \hat{P}_{qq}(z) &= \frac{4}{3} \frac{1+z^2}{1-z}. \end{aligned} \quad (2.15)$$

These are the unregularized splitting functions and they have to be regularized by an appropriate cut-off in z . However, an individual particle does not run through a range of t values, in the end each branching is associated with a fixed t value, and the task of the parton shower evolution is to pick that value. For a given t value, the integral of the branching probability over all allowed z values is:

$$\mathcal{I}_{ba}(t) = \int_{z_{\min}(t)}^{z_{\max}(t)} dz \frac{\alpha_s}{2\pi} \hat{P}_{ba}(z) \quad (2.16)$$

The probability that a branching occurs in a small range of t values δt is given by $\sum_b \mathcal{I}_{ba}(t) \delta t$, where the sum is over the possible radiated partons. Therefore the probability of *no* emission in that range is $1 - \sum_b \mathcal{I}_{ba}(t) \delta t$. If the evolution of parton a starts at a time t_0 , then the probability that it has not yet branched at a later time $t > t_0$ is given by the product of the probabilities that it did not branch in any of the small intervals of size δt between t_0 and t . If $\delta t \rightarrow 0$, the no-branching probability exponentiates and becomes:

$$\mathcal{P}_{\text{no-branching}}(t_0, t) = \exp \left[- \int_{t_0}^t dt \sum_b \mathcal{I}_{ba}(\hat{t}) \right] \equiv S_a(t). \quad (2.17)$$

which defines the so-called Sudakov formfactor $S_a(t)$. If a particle has already branched at a time $t' < t$, it can no longer branch at t . Therefore, the probability that particle a branches at time t is the product of the no-branching probability between times t_0 and t , multiplied by the probability of branching at t :

$$\mathcal{P}_a(t) = - \frac{d\mathcal{P}_{\text{no-branching}}(t_0, t)}{dt} = \left(\sum_b \mathcal{I}_{ba}(t) \right) \exp \left(- \int_{t_0}^t dt \sum_b \mathcal{I}_{ba}(\hat{t}) \right) \quad (2.18)$$

This equation is very similar to that for radioactive decay. The ordering in t above is treated differently for initial and final state parton showers. For the latter t is decreasing from a t_{\max} set by the hard interaction to a lower cut-off t_0 where the shower stops, while for initial state parton showers t is increasing from a lower scale t'_0 to t_{\max} . Also, if a parton a is created in a branching at time t_i and branches at a time t_{i+1} , then the non-branching probability between times t_i and t_{i+1} becomes $S_a(t_{i+1})/S_a(t_i)$.

To generate the ordering parameter t according to the Sudakov form-factor one may use the so called veto algorithm [14], which is described in appendix B. This is similar to the method of importance sampling described in section 2.1 with the difference that the generated values t are ordered in size.

2.2.1 Initial State Parton Showers

For incoming hadrons, the evolution of the parton densities, described in chapter 1, has to be considered. In the DGLAP evolution for the parton densities (eqs. (1.87) and (1.88)),

with $t = \log \mu^2 / \Lambda^2$ they are:

$$\frac{df_b(x, t)}{dt} = \sum_a \int \frac{d\hat{x}}{\hat{x}} f_a(\hat{x}, t) \frac{\alpha_s}{2\pi} \hat{P}_{ba} \left(\frac{x}{\hat{x}} \right) \quad (2.19)$$

This equation can be interpreted as the probability for parton a with momentum fraction \hat{x} to become resolved into partons b and c carrying momentum fractions $x = z\hat{x}$ and $(1-z)\hat{x}$ respectively, when t is increased by dt . However, it turns out that a backwards evolution scenario is often more efficient. This is due to the fact that in the event generator, the hard interaction is generated first and in order to match the parton shower to the matrix element it is more convenient to use the matrix element as a starting point also for the initial state parton shower, and evolve it backwards to the proton. In such a scenario, the starting scale t_{\max} is therefore given by the hard interaction. Backwards evolution can be said as a way to undo the evolution of the PDFs. The evolution gives the relative probability for the parton a to become unresolved into parton c during a small decrease in the scale by dt :

$$d\mathcal{P}_a = \frac{df_a(x_a, t)}{f_a(x_a, t)} = |dt| \sum_c \int \frac{d\hat{x}}{\hat{x}} \frac{f_c(\hat{x}, t)}{f_a(x_a, t)} \frac{\alpha_s}{2\pi} \hat{P}_{ac} \left(\frac{x_a}{\hat{x}} \right) \quad (2.20)$$

Defining in a similar way as in eq. 2.16:

$$\begin{aligned} \mathcal{I}_{ac}(t) &= \int_{z_{\min}(t)}^{z_{\max}(t)} \int dz \frac{d\hat{x}}{\hat{x}} \frac{f_c(\hat{x}, t)}{f_a(x_a, t)} \frac{\alpha_s}{2\pi} P_{ac}(z) \left(\frac{x_a}{\hat{x}} \right) \delta(x_a - z\hat{x}) \\ &= \int_{z_{\min}(t)}^{z_{\max}(t)} \frac{dz}{z} \frac{\alpha_s}{2\pi} P_{ac}(z) \frac{f_c(x_a/z, t)}{f_a(x_a, t)} \end{aligned} \quad (2.21)$$

and using the same reasoning leading up to eq. (2.17), constructing the no-branching probability will lead to a Sudakov formfactor for the backwards evolution:

$$S_a(x_a, t_{\max}, t) = \exp \left(- \int_t^{t_{\max}} dt \sum_c \mathcal{I}_{ac}(\hat{t}) \right) \quad (2.22)$$

This yields the probability of the first backwards initial state splitting:

$$d\mathcal{P}_a = \left(\sum_c \mathcal{I}_{ca}(t) \right) \exp \left(- \int_t^{t_{\max}} dt \sum_c \mathcal{I}_{ac}(\hat{t}) \right) \quad (2.23)$$

This can then be evolved down to a cut-off scale using the veto algorithm.

2.2.2 Parton Showers are Solutions to the DGLAP Equations

In the parton shower picture described here, one can derive an expression for the parton density functions. Consider for example the case of initial state radiation where an

incoming quark only radiates gluons. The Sudakov form factor in this parton shower is then

$$S_q(t) = \exp \left(- \int_{t_0}^t \frac{d\hat{t}}{\hat{t}} \int dz \frac{\alpha_s}{2\pi} \hat{P}_{qq}(z) \right) \quad (2.24)$$

The probability of finding the quark carrying a momentum fraction x at the scale t is $f(x, t)$. There are however several ways in which a quark may end up in the phase space point (x, t) , it may have been extracted with these values directly from the proton, or it may have started at a point with $\hat{x} > x$ and $\hat{t} < t$ and radiated any amount of gluons to end up in (x, t) . The probability for the first case to happen is given by

$$f(x, t)_{\text{no emitted gluons}} = S_q(t) f(x, t_0). \quad (2.25)$$

which is the probability density function for a quark at (x, t_0) multiplied by the probability that it does not radiate between the scales t_0 and t . For the second case, all possible ways the quark may radiate gluons has to be considered and integrated over:

$$\begin{aligned} f(x, t)_{\text{any emitted gluon}} &= \int_{t_0}^t \frac{d\hat{t}}{\hat{t}} \frac{S_q(t)}{S_q(\hat{t})} \int d\hat{x} dz \frac{\alpha_s}{2\pi} \hat{P}_{qq}(z) f(\hat{x}, \hat{t}) \delta(x - z\hat{x}) \\ &= \int_{t_0}^t \frac{d\hat{t}}{\hat{t}} \frac{S_q(t)}{S_q(\hat{t})} \int \frac{dz}{z} \frac{\alpha_s}{2\pi} \hat{P}_{qq}(z) f(x/z, \hat{t}) \end{aligned} \quad (2.26)$$

where, as mentioned above, the ratio $S_q(t)/S_q(\hat{t})$ gives the no-branching probability when evolving between scales \hat{t} and t . The delta function comes from the fact that after a branching the momentum fraction is changed from \hat{x} to $x = z\hat{x}$ by energy momentum conservation. The parton-shower expression for the parton density is thus:

$$f(x, t) = S_q(t) f(x, t_0) + \int_{t_0}^t \frac{d\hat{t}}{\hat{t}} \frac{S_q(t)}{S_q(\hat{t})} \int \frac{dz}{z} \frac{\alpha_s}{2\pi} \hat{P}_{qq}(z) f(x/z, \hat{t}) \quad (2.27)$$

Reorganizing the terms it becomes:

$$\frac{f(x, t)}{S_q(t)} = f(x, t_0) + \int_{t_0}^t \frac{d\hat{t}}{\hat{t}} \int \frac{dz}{z} \frac{\alpha_s}{2\pi} \hat{P}_{qq}(z) \frac{f(x/z, \hat{t})}{S_q(\hat{t})} \quad (2.28)$$

By taking the derivative of both sides with respect to t one obtains:

$$t \frac{\partial}{\partial t} \frac{f(x, t)}{S_q(t)} = \frac{1}{S_q(t)} \int \frac{dz}{z} \frac{\alpha_s}{2\pi} \hat{P}_{qq}(z) f(x/z, t) \quad (2.29)$$

Comparing this expression with the DGLAP equation for quark densities, eq. (1.87), one sees that they are very similar, except that f is replaced by f/S_q and the regularized splitting function is replaced by the unregularized one. If multiplied by the Sudakov, the l.h.s. of eq. (2.29) can be rewritten as:

$$S_q(t) \cdot t \frac{\partial}{\partial t} \frac{f(x, t)}{S_q(t)} = t \frac{\partial}{\partial t} f(x, t) - \frac{f(x, t)}{S_q(t)} t \frac{\partial}{\partial t} S_q(t) \quad (2.30)$$

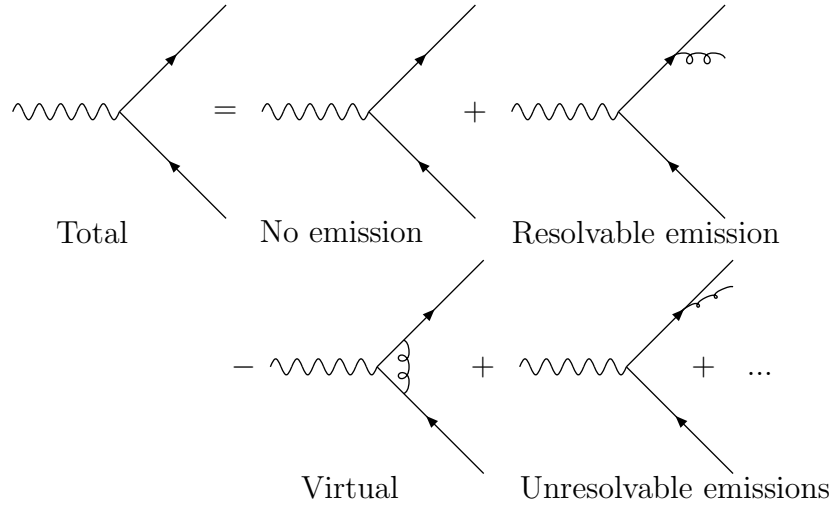


Figure 2.3: A pictorial view of how the unitarity of the parton shower leads to inclusion of virtual contributions to all orders, or: $\{\text{Resolvable emissions}\} = \{\text{Virtual contribution} - \text{Unresolvable emissions}\}$

where the last term is:

$$\frac{f(x, t)}{S_q t} t \frac{\partial}{\partial t} S_q(t) = -f(x, t) \int dz \frac{\alpha_s}{2\pi} \hat{P}_{qq}(z) \quad (2.31)$$

from the definition of $S_q(t)$. Substituting this into equation (2.29) yields:

$$t \frac{\partial f(x, t)}{\partial t} = \int dz \frac{\alpha_s}{2\pi} \hat{P}_{qq}(z) \left(\frac{1}{z} f(x/z, t) - f(x, t) \right) \quad (2.32)$$

Using the plus prescription, eq. (1.91), $P_{qq}(z) = \hat{P}_{qq}(z)_+$ this becomes

$$t \frac{\partial}{\partial t} f(x, t) = \int \frac{dz}{z} \frac{\alpha_s}{2\pi} P(z) f(x/z, t) \quad (2.33)$$

which now is exactly the DGLAP equation for a quark. It is easy to show that using Sudakov form factors allowing for any splitting will exactly reproduce the DGLAP equations, eqs. (1.87) and (1.88). The DGLAP equations are often referred to as evolution equations, since they describe how a parton from the proton evolves by radiating partons before it is resolved in the hard interaction.

Since the unregularized splitting functions are used in the Sudakov form factor, they have an infra red singularity at $z = 1$ which needs to be removed in order for the term to be defined. In chapter 1.1.4 this has been done by use of the plus prescription, but in the Sudakov form factor an explicit infra-red cut-off $z < 1 - \epsilon(t)$ is needed. Branchings with z larger than this are classified as unresolvable, they involve the emission of an undetectable soft parton. The Sudakov form factor then gives the probability of evolving

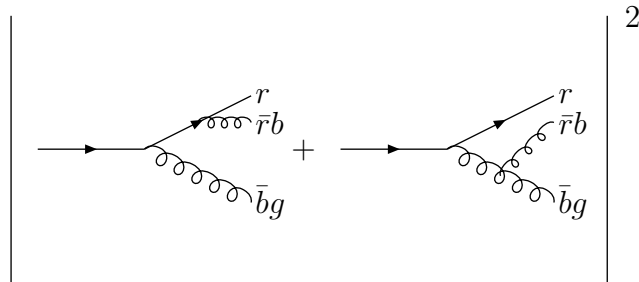


Figure 2.4: A diagram of the coherence term not taken into account in the DGLAP splitting probabilities.

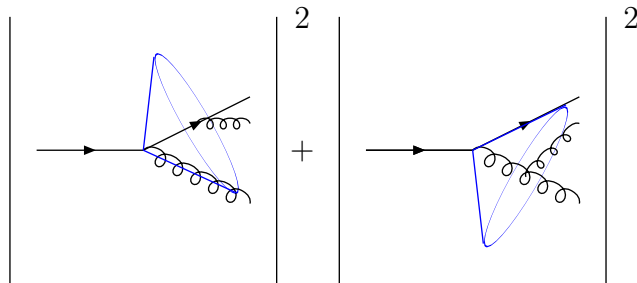


Figure 2.5: When restricting parton branchings to an angular ordered region many coherence effects are taken into account.

from t_0 to t without any *resolvable* branching. The Sudakov form factors also sum virtual (parton loop) corrections to all orders since they are included in the splitting functions. The virtual corrections affect the no-branching probability and are included via unitarity, which means that the sum of branching and no-branching probabilities must be unity. This is pictorially shown in fig. 2.3 for the case of final state radiation. The resolvable branching probability then tells us via unitarity the sum of virtual and unresolvable real contributions. These two kinds of contributions are both divergent but their sum is finite and hence consistently included in eq. (2.27).

2.3 The HERWIG Parton Shower

HERWIG (Hadron Emission Reactions With Interfering Gluons (including supersymmetric processes)) [15] is a multipurpose Monte Carlo event generator. It includes a wide range of hard interaction physics processes, calculated at leading order in α_s and also many kinds of colliding particles, e.g. hadron-hadron, lepton-hadron. In HERWIG the parton shower is restricted to an angular ordered region. The reason for angular ordering may be understood from coherent branchings. In fig. 2.4 it is shown how a green quark is radiating a gluon which is green-antiblue and thus changing colour to blue. The

blue colour-line then radiates a blue-antired gluon which gives a final state with a red quark, an antired-blue gluon and an antiblue-green gluon. This final state may also be achieved if the first radiated gluon is green-antired and then radiates another gluon which is antired-blue. Hence, these two diagrams should interfere, and it is not possible to tell which parton radiated the second gluon. Therefore, this radiation may be viewed as coming from a colour dipole. After the second gluon is radiated there are instead two dipoles, one between the red-antired colours and one between the blue-antiblue colours, and these will then radiate softer radiations independently. In the direction further away from the red-antired dipole, the radiations coming from the red-antired colourcharges will interfere destructively. In these directions, the radiations corresponds to emissions from a blue-antiblue dipole. Therefore, the radiations from within the blue-antiblue dipole becomes ordered in angle, as for the red-antired dipole. This interference effect can be approximated by radiations from each dipole independently but ordered in angle, which is illustrated in fig. 2.5.

To simulate this angular order in a parton shower, one may chose as a time variable

$$\xi = \frac{p_b \cdot p_c}{E_b E_c} \simeq 1 - \cos \theta_{ba} \simeq \frac{\theta_{ba}^2}{2} \quad (2.34)$$

for a branching of particle a into particles b and c . Here p_i is the four-momentum of particle i and E_i its energy and the opening angle θ_{ba} the angle between particles b and a . The second step is exact for relativistic partons and the last step holds for small angles. It should be noted that this quantity is not Lorentz invariant. Imposing an ordering such that $\xi_i < \xi_{i-1}$, where ξ_i and ξ_{i-1} refers to successive branchings, corresponds to an angular ordering $\theta_i < \theta_{i-1}$ for small angles. The propagator factor dt in equation (2.18) is replaces by $d\xi/\xi$. It may be noted that at small angles

$$\frac{d\xi}{\xi} \simeq 2 \frac{d\theta}{\theta} = 2 d \ln \theta \propto d\eta \quad (2.35)$$

where η is the (pseudo) rapidity, such that the angular order is similar to an order in rapidity. As in eq. (2.14), the probability of a branching $a \rightarrow bc$ becomes:

$$d\mathcal{P}_a = \sum_b \frac{\alpha_s}{2\pi} P_{ba}(z) \frac{d\xi}{\xi} dz \quad (2.36)$$

An angular cut-off ξ_0 is needed where the parton shower terminates. This is a somewhat arbitrary choice, since how the cut-off is chosen depends on at which angles a radiation can be considered resolvable. In HERWIG the following choice is adopted:

$$\xi_0 = \frac{Q_0^2}{E^2} \quad (2.37)$$

for a parton with energy E , where Q_0 is then a mass scale which has to be tuned. With this cut-off prescription, the most natural choice of evolution parameter is not ξ itself, but rather

$$Q = E \sqrt{\xi} \geq Q_0. \quad (2.38)$$

For small angles, this becomes:

$$Q = \frac{p_{\perp}}{2(1-z)} \quad (2.39)$$

where p_{\perp} is the transverse momentum of the radiated parton. For small z , the HERWIG radiations are therefore also ordered in p_{\perp} , but for large z , they are not.

Keeping the angular condition that $\xi_b, \xi_c < \xi_a$, this translates into

$$\begin{aligned} Q_b &= E_b \sqrt{\xi_b} = z E_a \sqrt{\xi_b} < z E_a \sqrt{\xi_a} = z Q_a, \\ Q_c &= E_c \sqrt{\xi_c} = (1-z) E_a \sqrt{\xi_c} < (1-z) E_a \sqrt{\xi_a} = (1-z) Q_a \end{aligned} \quad (2.40)$$

where $z = E_b/E_a$ as before. This gives a cut-off condition on z :

$$\frac{Q_0}{Q_a} < z < 1 - \frac{Q_0}{Q_a} \quad (2.41)$$

Then the Sudakov formfactor for the HERWIG final state parton shower becomes:

$$\Delta_{a \rightarrow bc}(Q_a) = \exp \left(- \int_{4Q_0^2}^{Q_a^2} \frac{dQ^2}{Q^2} \int_{\frac{Q_0}{Q}}^{1-\frac{Q_0}{Q}} dz \frac{\alpha_s(z^2(1-z)^2 Q^2)}{2\pi} \hat{P}_{ba}(z) \right) \quad (2.42)$$

For initial state radiation the backwards evolution is used, which means that the Sudakov is modified as before to also include the density functions of the partons in the branchings. It proceeds from the hard scattering at a scale Q set by the colour coherence, down to a hadron scale Q_0 , set by a parameter.

2.3.1 The Angular Ordered Phase-space for Heavy Quarks

When heavy quarks are created in the hard interaction, the angular ordered phase-space of radiation from the quarks is modified. For a heavy quark a splitting into another heavy quark b and a light particle c , the variable ξ becomes:

$$\xi = \frac{p_b p_c}{E_b E_c} = 1 - \frac{|\mathbf{p}_b|}{E_b} \cos \theta_{ba} = 1 - \sqrt{1 - \frac{m^2}{E_b^2}} \cos \theta_{ba} = 1 - \beta \cos \theta_{ba}. \quad (2.43)$$

where β is the velocity of the radiated heavy quark. However, the soft radiation in the direction of the heavy quark is suppressed dynamically within an angle such that [16]:

$$\xi > \frac{m^2}{E_b^2}. \quad (2.44)$$

This region is called a “dead cone” and has been observed in experiments, e.g. in [17]. As seen in fig. 2.5, the radiations are also confined within a cone. The region outside this cone is called a “dead zone”. For final and initial state radiation it is given by:

$$\xi < 1 \quad \text{Final state} \quad (2.45)$$

$$\xi < z^2 \quad \text{Initial state.} \quad (2.46)$$

For mass-less partons this corresponds to radiation in angles $\theta < \pi/2$. The factor z^2 in initial state radiation comes from the backwards evolution, where now $z = E_a/E_b$. The z values with heavy quarks are restricted by:

$$\frac{m}{E_b\sqrt{\xi}} < z < 1 \quad (2.47)$$

2.4 Hadronization

After the final state parton shower terminates it has produced a set of particles with a virtuality of the order of the cut-off scale t_0 . These particles then enter the hadronization phase of transition described in fig. 2.1, where long distance non-perturbative effects are important. In this phase the particles have to be transformed into hadrons. Here, perturbative QCD cannot be used. Instead, to describe the hadronization, one must rely on phenomenological models. Some of these models will be described in this section. In principle, the parameter t_0 is arbitrary and not connected to hadronization. Hadronization is expected to occur at a scale close to Λ_{QCD} . However, the cut-off could be treated like a hadronization parameter. This comes from the fact that a particle with higher virtuality is expected to produce more hadrons. Therefore, in a perfect hadronization model, it should be possible to choose a value of t_0 such that the number of hadrons produced do not depend upon it. In practice this does not happen, since the hadronization models never match the parton shower perfectly. In these models, t_0 is therefore treated as a parameter, which has to be fitted to measurements. The favoured value tends to be rather small, a few times Λ_{QCD} , which may imply that an extrapolation of perturbative theory is more reliable on these scales than the hadronization models. This observation, that perturbation theory seems to be important down to very small scales, leads to the hypothesis of local parton hadron duality [18]. This hypothesis states that the flow of momentum and quantum numbers at the hadron level follow those at the parton level. Also, as a consequence of this hypothesis, the fragmentation of a parton can be described by a fragmentation function $D_p^H(z)$, which is the probability of finding a hadron H with momentum fraction z inside a parton p . This can be seen as the inverse of a parton density function of the hadron. The flavour of a quark producing a jet should also be found close to the jet-axis. The deviation from the parton-hadron duality reflects how large the hadronization effects are at scales close to Λ_{QCD} .

2.4.1 Independent Fragmentation

The simplest approach to generating hadrons from the partons produced by the parton shower or by the hard interaction, is to assume that each particle fragments independently. One such approach is the so called Field Feynman scheme [19, 20] shown in fig. 2.6. Here the fragmenting quark is combined with an antiquark from a $q\bar{q}$ pair created out of the vacuum, to give a meson with energy fraction z of the original quark. The leftover

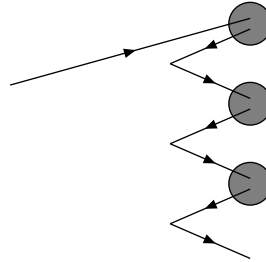


Figure 2.6: In independent fragmentation a quark is picking up an antiquark from a $q\bar{q}$ pair created from vacuum to create a meson. The leftover quark is then also picking up an antiquark in the same way and so on until a cut-off is reached.

quark, with energy fraction $(1 - z)$, is fragmented in the same way until the leftover energy falls under a cut-off scale. This scheme is easy to implement in a recursive Monte Carlo algorithm. The relative transverse momenta of the created $q\bar{q}$ pairs are given by a Gaussian distribution. For gluon fragmentation, the gluon is first split into a $q\bar{q}$ pair, assigning the gluon's momenta to one of the created particles according to the DGLAP splitting function. Baryons are formed by the creation of $qq\bar{q}$ pairs from the vacuum.

This model only includes a few parameters: the width of the transverse momentum distribution, the ratio of creation of different flavours and the ratio of vector to pseudoscalar mesons. It still manages to describe many features of two- and three-jet final states in e^+e^- annihilation at moderate energies. A weakness of this model is that it depends on the energy of the parton rather than the virtuality, which makes it frame dependent. This typically leads to violation of momentum conservation which has to be corrected after the hadronization is completed. Another weakness is the leftover colour and flavour from the leftover parton, which need to be neutralized.

Peterson Fragmentation

For the independent fragmentation of a heavy quark, the so called Peterson fragmentation [21] is often used. This model is similar to the Field-Feynman scheme above with the difference that the heavy quark momentum will only be slightly altered when attaching a light anti-quark to it in the fragmentation process. Therefore the heavy quark and the produced hadron should carry almost the same energy and the hypothesis of local parton hadron duality is expected to be especially true here. The hadron containing the heavy quark take a fraction z of the heavy quark energy, while the leftover light quark takes the energy fraction $(1 - z)$. The Peterson fragmentation function is:

$$D_Q^H(z) = \frac{N_H}{z \left(1 - \frac{1}{z} - \epsilon_Q \frac{1}{1-z}\right)^2}, \quad (2.48)$$

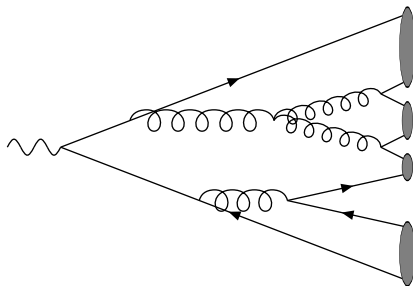


Figure 2.7: Clusters form between colour connected quarks in the cluster model. Gluons are made to split up into $q\bar{q}$ pairs which then can form clusters.

where N is the normalization, which is fixed by demanding that the sum over all possible hadrons containing the heavy quark is unity. Here ϵ_Q is a parameter which should be of the order of the ratio of the light quark mass to that of the heavy quark, m_q^2/m_Q^2 , but it has to be fitted to experimental data. The function peaks at $z \simeq 1 - 2\epsilon_Q$ with a width $\sim \epsilon_Q$. This means that the larger m_Q is, the more of the heavy quarks momentum will be taken by the produced hadron. The light quark created may then fragment according to the Field Feynman scheme described above. When implemented in a computer program, the z values of the created hadrons are generated according to eq. (2.48) to create distributions of the kinematics of the created hadrons, which then can be put into histograms. These distributions then have to be weighted with the probability of creating the specific hadron, i.e. the value to the normalization N_H by which the hadron contributes.

2.4.2 Cluster Fragmentation

At larger distances, of the order Λ_{QCD} , the force between the partons is expected to be significant. This is not taken into account in the independent fragmentation models where each parton is treated separately. A relatively straight forward approach to take the interaction between the produced partons into account are the cluster fragmentation models. The bases of these models is the pre-confinement properties, proven in perturbative QCD [22, 23, 24]. Pre-confinement implies that, at the end of a parton shower, the mass and spatial distributions of colour singlet quark anti-quark pairs have a universal distribution. These colour singlet pairs are called clusters, and they do not yet represent any real hadrons. In practice, any gluons remaining at the cut-off scale t_0 are forced to split into a light $q\bar{q}$ pair. The distribution of the cluster masses falls rapidly at high masses and is very weakly dependent on Q^2 [25]. The universal properties of these colour singlet clusters, which appear naturally at the end of the parton shower, makes it a useful bases for a hadronization model.

The clusters once formed, are assumed to decay into real hadrons independently. Most clusters Cl are assumed to decay into two hadrons h_1 and h_2 . These hadrons are subject only to flavour conservation, such that if h_1 is a $q\bar{x}$ hadron, then h_2 is a $\bar{q}x$ hadron where

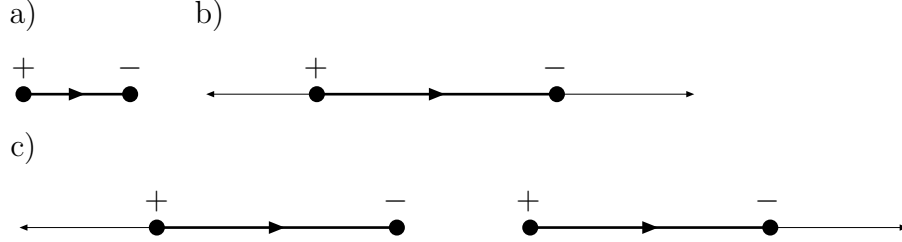


Figure 2.8: a) Two opposite charges in one dimension, with the field drawn as a thick line with an arrow indicating the direction of the force flux. b) When one of the particles get a kick and the pair get separated, the energy in the field between them increases. The figure is drawn in the CM-system of the particles and the thin arrows indicates the velocities of the particles. c) Eventually another pair of oppositely charged particles can be created, by the energy stored in the string, and the string breaks.

x is either a quark or diquark. The invariant mass of the cluster is thus used to create either one or two $q\bar{q}$ -pairs. The probability for a given pair of hadrons to be created is assumed to be proportional to its available phase space:

$$\mathcal{P}(Cl \rightarrow h_1 + h_2) \propto (2J_{h_1} + 1)(2J_{h_2} + 1)\mathbf{p}(m_{Cl}, m_{h_1}, m_{h_2})\Theta(m_{Cl} - m_{h_1} - m_{h_2}) \quad (2.49)$$

where J_h are the angular momenta of the hadrons, \mathbf{p} is the three-momentum in the two-body decay in the center of mass frame and the Θ function ensures that the decay is allowed, i.e. that $m_{Cl} > m_{h_1} + m_{h_2}$. The decay is also assumed to be isotropic in the cluster's rest frame.

There are two special cases where this scheme doesn't work. Some clusters will be too light to decay into two hadrons. Such clusters are transformed into one hadron with the excess momenta distributed amongst neighbouring clusters. In the tail of the mass-spectrum there are also some very heavy clusters. Here isotropic two-body decays would yield hadrons with unnaturally large momenta. By introducing light $q\bar{q}$ pairs these clusters are forced to split into lighter daughter clusters whose direction of motion are aligned with the original $q - \bar{q}$ axis. The selection of which clusters are considered heavy enough for this type of decay requires extra parameters, which need to be tuned. This scheme of letting a cluster decay into daughter clusters is similar to the Lund colour string model, which is the subject of the next section.

2.4.3 Lund String Fragmentation

In the Lund string fragmentation model [26, 27, 28], the underlying assumption is more complex than for independent or cluster fragmentations. Here, the confining colour force field between a quark and an antiquark is believed to collapse into a colour flux tube of uniform energy density per unit length. This tube is approximated by a colour string with

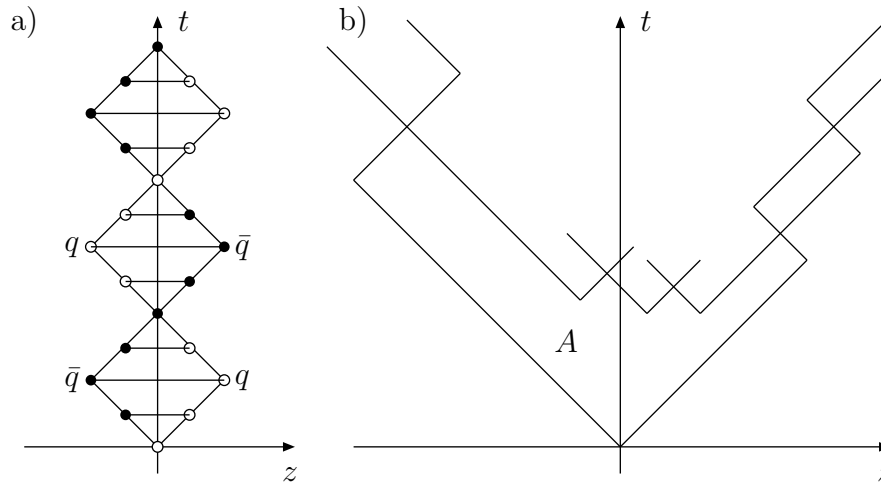


Figure 2.9: a) A quark and an antiquark in their CM-system. When separated they oscillate through each other in a so called yo-yo mode. b) If the separation becomes large enough the string breaks, creating a new quark-antiquark pair. It may even break in many places, creating several such pairs. All quark-antiquark pairs bound in yo-yo modes in the end represent a meson.

tension $\kappa \simeq 1\text{GeV}/\text{fm}$. This string is classical, massless and relativistic. The potential energy stored in the string is:

$$V(r) \propto \kappa r \quad (2.50)$$

where r is the length of the string. When a quark and an antiquark, e.g. created in e^-e^+ annihilation, are separated the energy stored in the string is therefore proportional to the separation of the quarks. When separated, the kinetic energy of the endpoint quark and anti-quark is transformed into potential energy stored in the string between them. If the quarks get enough separated, there will be sufficient energy stored in the string for another $q\bar{q}$ pair to be created. When this happens, the string breaks, as is depicted in fig. 2.8.

If the initial kinetic energy of the quarks is smaller than what is needed to create another $q\bar{q}$ pair, the end point particles will turn and accelerate towards each other again. This movement is called a yo-yo mode. For the simplest case of massless particles it is depicted in fig. 2.9 a).

All $q\bar{q}$ pairs bound in yo-yo modes represent a hadron. In fig. 2.9 b), the hadronization of a $q\bar{q}$ initial state is shown. The invariant mass available for hadron production is proportional to the area A underneath the breaking points in the picture. Hadrons are created by the Lund symmetric fragmentation function:

$$f(z) = \frac{N}{z} (1-z)^a e^{-b\frac{m^2}{z}} \quad (2.51)$$

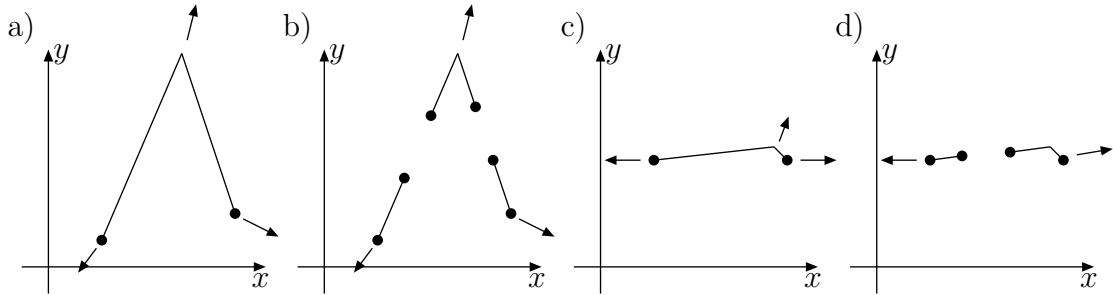


Figure 2.10: a) The string segment between a quark and an antiquark get a kink. This kink acts as a gluon. b) The string fragments into hadrons, the kink gets embedded into one of the hadrons. If the gluon is hard enough it give rise to a third jet. c) A gluon is emitted close to one of the quarks. d) When hadronizing the collinear gluon does not give rise to a jet.

where z is the light-cone momentum fraction taken by the hadron with transverse mass m_{\perp} . Here N is normalization and a is a parameter. The mass of the hadron is proportional to the space-time area spanned by one cycle in the yo-yo mode. The hadronization proceeds from both ends of the string simultaneously. Therefore, and since it is only possible to create a limited number of hadrons, it is necessary to have some special treatment of the central region, both for quantum number conservation and for momentum conservation.

Gluons are in the Lund model treated as kinks on the string segment naturally making gluons colour octets, since each kink will be connected to both a quark and an antiquark. The gluon hadronizes when the string breaks on both sides of the kink giving a hadron going in the direction of the gluon. This is depicted in fig. 2.10 a) and b). This treatment of gluons makes the model automatically infrared safe, since a soft gluon will not have enough energy to break the string. When this happens the only contribution is a small p_{\perp} broadening of the quark jets. The model is also collinear safe, since when the kink is close to one of the end points the string will only break on the other side of the gluon and what is obtained is a quark-jet containing the whole string piece between the kink and the quark as depicted in fig. 2.10 c) and d).

2.5 Other Parton Evolutions

In this chapter it has been described how a parton shower can be used to find exclusive final states according to the DGLAP equations. This evolution is ordered in transverse momentum of the radiated emissions. A parton enter the hard interaction after radiating one or many partons i , losing an energy fraction $1 - z_i$ in each branching. The momentum fraction of the interacting incoming parton is given as a product of all z_i values in the

branchings, such that

$$x_{Bj} = \prod_i z_i x_0. \quad (2.52)$$

If the incoming parton is a quark radiating gluons, the splitting function has a term proportional to $1/(1-z)$, which means that radiations with large z will dominate these branching. Thus x_{Bj} may be large in this case. Also, in this case, the radiations will be ordered in transverse momenta.

If the incoming parton is a gluon, there is two divergent pieces in the splitting function, a $1/(1-z)$ piece and also a $1/z$ piece, which means that the gluon may radiate many gluons with small z values. In this case x_{Bj} may be small. A small value of x_{Bj} corresponds intuitively to a scenario where the momentum of the proton is distributed over many partons. Therefore, in order to resolve these partons, Q^2 should be large. With a large value of Q^2 , the value of x_{Bj} may be arbitrary small in the DGLAP picture, and the radiations are still ordered in virtuality of the links.

If, on the other hand, one looks at a region of phase-space where x_{Bj} is small and Q^2 is also small, the phase-space for virtuality ordered chains becomes decreased. In this region of phase-space, many radiations are expected since x_{Bj} is small and at the same time, the order in virtuality in the links is suppressed by the small scale. Therefore is the DGLAP picture not expected to hold in this region of phase-space.

An evolution for small x_{Bj} , where the virtuality of the link is a random walk is called BFKL evolution after the physicists Balitsky, Fadin, Kuraev and Lipatov [29, 30, 31]. This kind of evolution is still not implemented in an event generator, even though some recent progress looks promising, e.g. [32].

An evolution including evolution both at small and at large values of x_{Bj} is called a CCFM-evolution after the physicists Catani, Ciafaloni, Fiorani and Marchesini [33, 34, 35, 36] and has been implemented in the multi purpose event generator CASCADE [37] for a gluon ladder, and in the LDC MC [38] in a modified form. The $1/(1-z)$ branchings becomes colour ordered in q_\perp , in the chain, while the non-eikonal current gives a random walk in q_\perp . The CCFM evolution becomes strictly ordered in angle, similarly to the order in Q in the HERWIG parton shower. The CCFM is possible to implement with so-called non-Sudakov formfactors.

Chapter 3

Next-to-leading Order Calculations

In this chapter, the QCD cross-section for heavy quark produced in photoproduction will be described at next-to-leading order. There are two parts of this calculation: the hadronic part and the pointlike part, which has to be added in order to describe real physical observables. The hadronic part has been calculated in [39]. In this chapter, the pointlike part of the calculation will be described. Here, the massive fixed flavour number scheme, described in chapter 1.1.5, is used in the calculation.

At leading order the cross-section for this interaction is of order $\mathcal{O}(\alpha_{EM}\alpha_s)$. This is the lowest order by which the process is calculable and is called the Born term. The two diagrams relevant for the Born term are shown in fig. 3.1. Next-to-leading order (NLO) is then defined as one higher order in α_s , i.e. $\mathcal{O}(\alpha_{EM}\alpha_s^2)$. At NLO, two kinds of terms have to be taken into account. Firstly, the real emissions, where one of the four particles in the interaction emits a real gluon or light quark, which are of order $\mathcal{O}(\alpha_{EM}\alpha_s^2)$. These diagrams are shown in figs. 3.2 and 3.3. The second kind of diagrams are the virtual contributions, shown in fig. 3.4, which are of order $\mathcal{O}(\alpha_{EM}\alpha_s^4)$. This is of higher order than NLO, but these terms still play a role in the NLO calculation since they give the same final state as the Born term and therefore interfere with the LO contribution. These interference term are of order $\mathcal{O}(\alpha_{EM}\alpha_s^2)$, which is NLO.

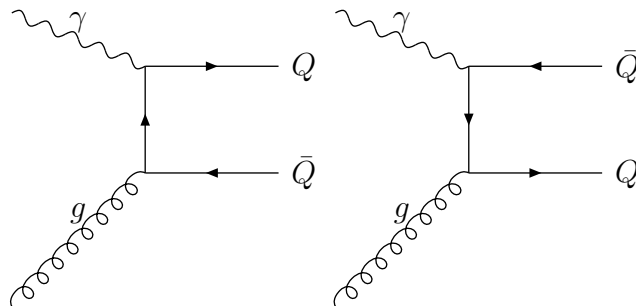


Figure 3.1: The two diagrams contributing to the Born-term

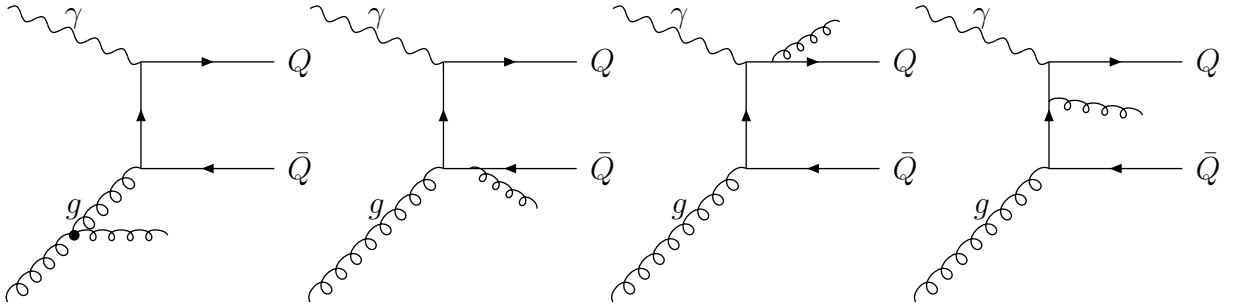


Figure 3.2: The real emission diagrams corresponding to the $\gamma g \rightarrow Q\bar{Q}g$ process. The charge conjugated diagrams are implied. These diagrams are depicting $\mathcal{O}(\alpha_{\text{EM}}\alpha_s^2)$ contributions.

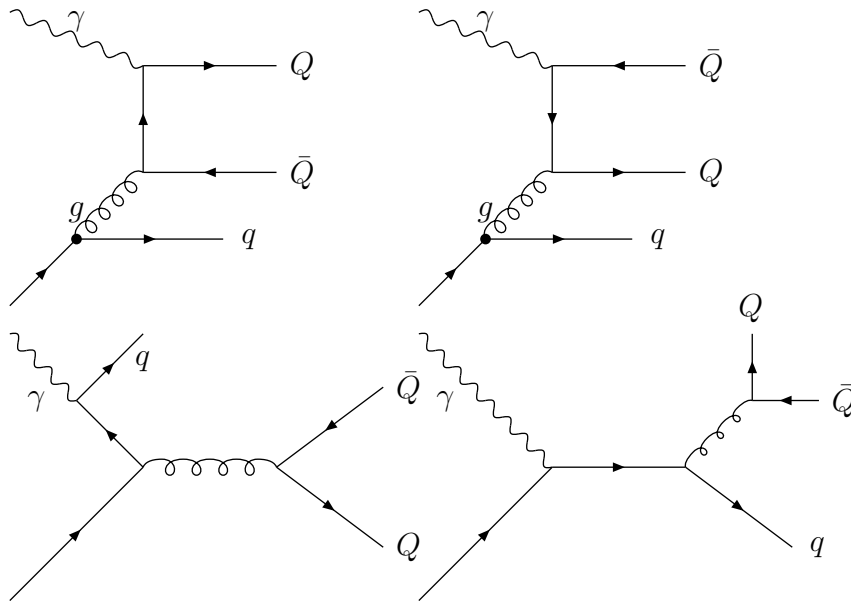


Figure 3.3: The real emission diagrams corresponding to the $\gamma q \rightarrow Q\bar{Q}q$ process. The charge conjugated diagrams are implied. These diagrams are depicting $\mathcal{O}(\alpha_{\text{EM}}\alpha_s^2)$ contributions.

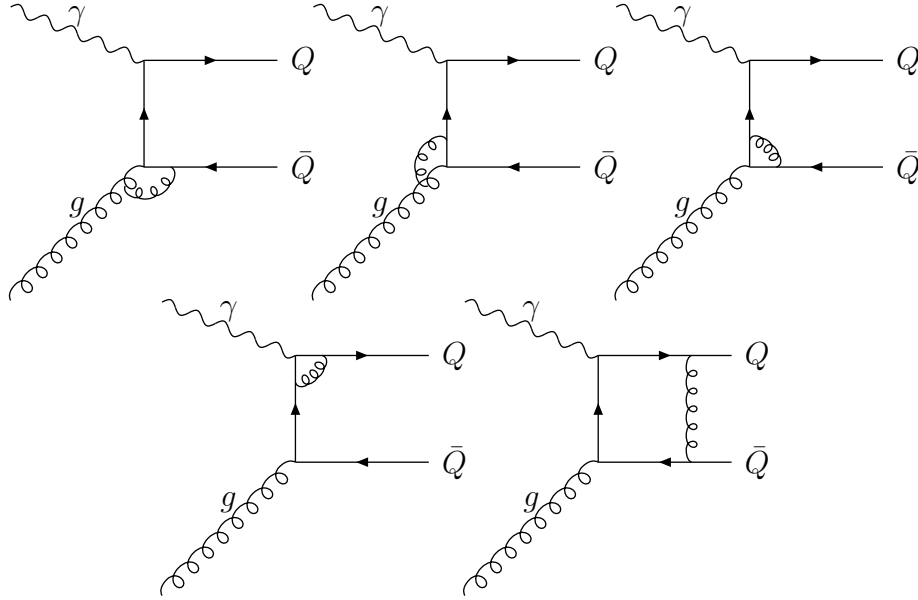


Figure 3.4: Virtual diagrams which contribute to the NLO cross section. These diagrams are of order $\mathcal{O}(\alpha_{\text{EM}}\alpha_s^4)$ but the interference with the Born terms gives an order $\mathcal{O}(\alpha_{\text{EM}}\alpha^2)$ contribution. Charge conjugated diagrams are implied.

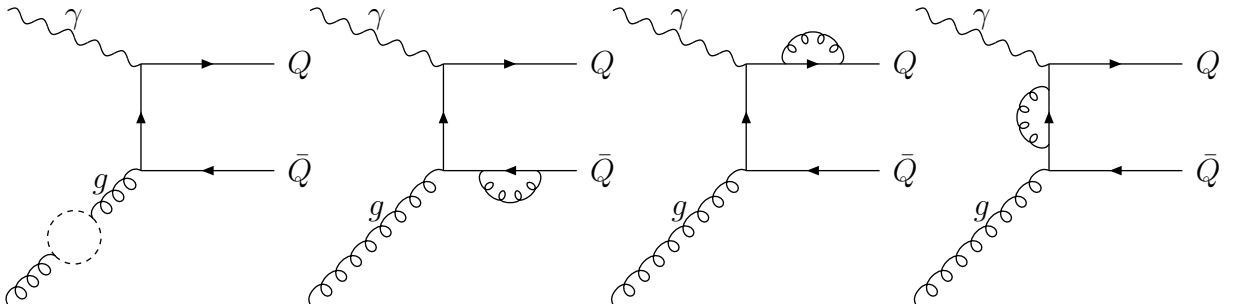


Figure 3.5: Virtual diagrams which do not take part of the next-to-leading order calculation. Instead diagrams of this type are absorbed in the definition of the coupling α_s through the renormalization procedure. Charge conjugated diagrams are implied.

Schematically the matrix element squared at NLO is given by:

$$|A_2|^2 = B^*B + (B^*V + V^*B) \tag{3.1}$$

$$|A_3|^2 = R^*R, \tag{3.2}$$

where B , V and R stands for the amplitudes of the Born term, the virtual terms and the real terms respectively. The subscripts denote the number of partons in the final state. With the notation

$$\begin{aligned} d\sigma^{(b)} &\propto B^*B \\ d\sigma^{(v)} &\propto B^*V + V^*B \\ d\sigma^{(r)} &\propto R^*R \end{aligned} \tag{3.3}$$

calculating the cross-section at next-to-leading order means computing the integrals:

$$\sigma_{\text{NLO}} = \int_3 d\phi_3 (d\sigma^{\text{Real}}) + \int_2 d\phi_2 (d\sigma^{\text{Born}} + d\sigma^{\text{Virtual}}). \tag{3.4}$$

where the integration is over a phase-space $d\phi_n$ which depends on how many particles are produced in the final state $n = 2, 3$. Each order in the perturbative expansion of the cross-section is finite, which means that the sum of the integrals in eq. (3.4) is finite. However, both integrals are separately divergent. This implies that the divergencies in the first integral exactly compensate those in the second integral. One way to deal with these intermediate divergencies is to regulate them by working in $d = 4 - 2\epsilon$ dimensions, where they are replaced by singularities in $1/\epsilon$. The principle behind dimensional regularization is explained in appendix A.

The purpose of this chapter is to explain how the NLO cross-section in eq. (3.4) can be calculated. In section 3.1 this will be illustrated in a simpler form, by a toy model. In section 3.2.2 it will be explained in general how the factorization theorem can be used to cancel the intermediate divergencies. In section 3.3, the calculation of the NLO cross-section for heavy flavour photoproduction will be described.

3.1 A Toy Model of a Next-to-Leading Order Cross-section Calculation

In this section a Toy Model is presented, which puts the key feature of the NLO calculation in a simpler form than the full QCD case [40]. This Toy Model will also be a good tool to present the key features of MC@NLO in a later chapter. In this model a system can radiate massless particles, called photons. The system has the energy x_s and the radiated photon is given the energy x such that $0 \leq x \leq x_s \leq 1$. After the emission the energy of the system becomes $x'_s = x_s - x$. The system may undergo a series of emissions but the photons will not emit further.

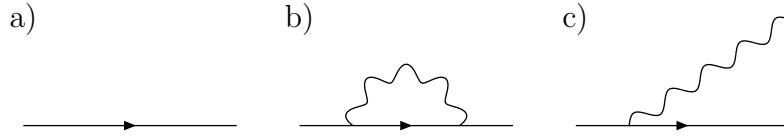


Figure 3.6: Simple pictures of the contributions to the toy model NLO calculation. a) shows the Born contribution, b) shows a virtual contribution and c) shows a real emission diagram.

To calculate the NLO cross-section for this system, the Born, virtual and real emission terms have to be defined. These are depicted in figure 3.6. In the Born term, no extra photon is radiated as seen in fig. 3.6 a). This is the leading order diagram. In the virtual corrections depicted in fig. 3.6 b), a virtual photon is radiated and reabsorbed by the system. This gives a contribution of the order $\mathcal{O}(a^2)$, where a is the coupling in the model. This is higher than NLO, but interference of the Born and virtual terms is of order $\mathcal{O}(a)$, which is NLO. In the real contribution shown in fig. 3.6 c), a real photon is radiated taking an energy x . This process is also of order $\mathcal{O}(a)$.

The total NLO cross section is

$$\frac{d\sigma_{\text{NLO}}}{dx} = \left(\frac{d\sigma}{dx}\right)_B + \left(\frac{d\sigma}{dx}\right)_V + \left(\frac{d\sigma}{dx}\right)_R \quad (3.5)$$

where

$$\left(\frac{d\sigma}{dx}\right)_B = B\delta(x), \quad (3.6)$$

$$\left(\frac{d\sigma}{dx}\right)_V = a\left(\frac{B}{2\epsilon} + V\right)\delta(x), \quad (3.7)$$

$$\left(\frac{d\sigma}{dx}\right)_R = a\frac{R(x)}{x}. \quad (3.8)$$

Here, B and V do not depend on x , and

$$\lim_{x \rightarrow 0} R(x) = B. \quad (3.9)$$

The delta-functions in eqs. (3.6) and (3.7) come from the fact that for the Born and virtual terms, no photon is radiated and hence $x = 0$. The parameter ϵ is entering the dimensional regularization in $4 - 2\epsilon$ dimensions. All singularities are then expressed as poles in ϵ .

The total NLO cross-section is then:

$$\sigma_{\text{NLO}} = \int_0^1 dx \left[\left(\frac{d\sigma}{dx}\right)_B + \left(\frac{d\sigma}{dx}\right)_V + \left(\frac{d\sigma}{dx}\right)_R \right] \quad (3.10)$$

The pole in ϵ in the virtual contribution has to be canceled by that extracted from the real contribution. There are different ways to do this. In the following, two methods will be described: the phase space slicing method and the subtraction method.

3.1.1 The Phase Space Slicing Method

The pole in ϵ is present in the virtual part of the calculation. In order to cancel this singularity, the real part of the calculation may be modified. In the phase space slicing method, a small parameter δ is introduced into the real contribution in the following way:

$$\begin{aligned}
 \sigma_{\text{R}} &= \int_0^1 dx \left(\frac{d\sigma}{dx} \right)_R \\
 &= \int_0^\delta dx \left(\frac{d\sigma}{dx} \right)_R + \int_\delta^1 dx \left(\frac{d\sigma}{dx} \right)_R \\
 &= a \int_0^\delta dx \frac{R(x)}{x} + a \int_\delta^1 dx \frac{R(x)}{x}
 \end{aligned} \tag{3.11}$$

The second term on the r.h.s. of this equation does not contain any singularity, while the first term still does. Here, $R(x)$ may be expanded in a Taylor series around $x = 0$, only keeping the first term:

$$R(x) = R(0) + \mathcal{O}(x) = B + \mathcal{O}(x) \tag{3.12}$$

The first integral in the r.h.s. of eq. 3.11 then becomes:

$$\begin{aligned}
 aB \int_0^\delta \frac{dx}{x} + \mathcal{O}(\delta) &= aB \int_0^\delta x^{-2\epsilon} \frac{dx}{x} + \mathcal{O}(\delta) = aB \frac{\delta^{-2\epsilon}}{-2\epsilon} + \mathcal{O}(\delta) \\
 &= a \left(\frac{1}{-2\epsilon} + \ln \delta \right) B + \mathcal{O}(\epsilon) + \mathcal{O}(\delta)
 \end{aligned} \tag{3.13}$$

where dimensional regularization has been used in a similar way as described in eq. (A.6), and in the last step $\delta^{-2\epsilon}$ is Taylor expanded in ϵ such that $\delta^{-2\epsilon} = 1 - \ln \delta \cdot 2\epsilon + \mathcal{O}(\epsilon^2)$. The factor $-a\frac{B}{2\epsilon}$ will exactly cancel the pole in ϵ present in the virtual contribution, which can be seen when eqs. (3.14) and (3.11) are substituted into eq. (3.10):

$$\begin{aligned}
 \sigma_{\text{NLO}}^{\text{slice}} &= \int_0^1 dx \left[\left(\frac{d\sigma}{dx} \right)_B + \left(\frac{d\sigma}{dx} \right)_V + \left(\frac{d\sigma}{dx} \right)_R \right] \\
 &= a \left(-\frac{1}{2\epsilon} + \ln \delta \right) B + \int_0^\delta dx \delta(x) \left[B + a \left(\frac{B}{2\epsilon} + V \right) \right] \\
 &\quad + \int_\delta^1 dx \left[B\delta(x) + a \left(\frac{B}{2\epsilon} + V \right) \delta(x) + a \frac{R(x)}{x} \right] + \mathcal{O}(\delta) \\
 &= B + a \left[(B \ln \delta + V) + \int_\delta^1 dx \frac{R(x)}{x} \right] + \mathcal{O}(\delta).
 \end{aligned} \tag{3.14}$$

This is the NLO prediction of the cross-section according to the phase space slicing method. Here δ act as a phenomenological parameter. The terms $\mathcal{O}(\delta)$ cannot be computed and one has to check that they are numerically small by plotting $\langle O \rangle_{\text{Slice}}$ versus δ in a suitable range in δ .

3.1.2 The Subtraction Method

In the subtraction method no approximation is performed, instead one term is added and subtracted from the real contribution in order to cancel the pole in the virtual contribution. The addition and subtraction of

$$\frac{aB}{x} \quad (3.15)$$

in the real contribution yields:

$$\begin{aligned} \sigma_{\text{R}} &= a \int_0^1 dx \left[\frac{R(x)}{x} + \frac{aB}{x} - \frac{aB}{x} \right] \\ &= aB \int_0^1 \frac{dx}{x} + a \int_0^1 dx \frac{R(x) - B}{x} \\ &= -a \frac{B}{2\epsilon} + a \int_0^1 dx \frac{R(x) - B}{x}, \end{aligned} \quad (3.16)$$

where dimensional regularization has been used similarly as in eq. 3.14 in the last step. As before, in the phase space slicing method, there is a term $-a \frac{B}{2\epsilon}$ present here, which is what is needed to cancel the divergency in ϵ present in the virtual contribution. This is seen by substituting eq. (3.16) into eq. (3.10), which gives:

$$\sigma_{\text{NLO}}^{\text{sub}} = B + aV + a \int_0^1 dx \frac{R(x) - B}{x}, \quad (3.17)$$

which is the NLO prediction of the cross-section as given by the subtraction method. The expectation value of an IR-safe¹ observable $O(x)$ is given by:

$$\begin{aligned} \langle O \rangle_{\text{sub}} &= \int_0^1 O(x) B \delta(x) dx + a \int_0^1 O(x) V \delta(x) dx + a \int_0^1 O(x) \frac{R(x) - B}{x} dx \quad (3.18) \\ &= BO(0) + aVO(0) + a \int_0^1 O(x) \frac{R(x) - B}{x} dx \end{aligned}$$

such that the term $aBO(x)/x$ is being added and subtracted.

¹IR-safe observables are also called jet-observables.

3.2 The Subtraction Method in QCD

In the subtraction method, the QCD NLO cross-section eq. 3.4 becomes:

$$\sigma_{\text{NLO}} = \int_3 d\phi_3 (d\sigma^{\text{Real}} - d\sigma^{\text{Sub}}) + \int_2 d\phi_2 (d\sigma^{\text{Born}} + d\sigma^{\text{Virtual}}) + \int_3 d\phi_3 (d\sigma^{\text{Sub}}). \quad (3.19)$$

The cross-section $d\sigma^{\text{Sub}}$, which is subtracted and added should fulfill two main properties:

1. Firstly, it must exactly match the singular behaviour in d dimensions of the real contribution $d\sigma^{\text{Real}}$. Therefore it acts as a local counter term for $d\sigma^{\text{Real}}$ and one can safely perform the limit $\epsilon \rightarrow 0$ in the first integral in eq. (3.19).
2. Secondly, $d\sigma^{\text{Sub}}$ must be analytically integrable in d dimensions over the one-parton subspace leading to the divergencies, such that the NLO cross-section can be written as:

$$\sigma_{\text{NLO}}^{\text{sub}} = \int_3 d\phi_3 (d\sigma^{\text{Real}} - d\sigma_3^{\text{Sub}}) \Big|_{\epsilon=0} + \int_2 d\phi_2 \left(d\sigma^{\text{Virtual}} + \int_1 d\sigma_3^{\text{Sub}} \right) \Big|_{\epsilon=0} + \int_2 d\phi_2 d\sigma^{\text{Born}} \quad (3.20)$$

where the subscript of the subtraction term is indicating over which phase-space it is integrated.

After integration, the subtraction terms cancel exactly by construction. The task then becomes to construct such subtraction terms.

3.2.1 Soft and Collinear Limits

The real cross-section contribution has the following structure [41]:

$$d\sigma^{\text{Real}} = d\Phi_{m+1} |\mathcal{M}_{m+1}(\{k_k\})|^2 F_J^{(m+1)}(\{k_k\}) \quad (3.21)$$

where $d\Phi_{m+1}$ and the tree level matrix element $\mathcal{M}_{m+1}(\{k_k\})$ are process dependent and $F_J^{(3)}$ depends on which observables are calculated.

The subtraction terms may be found by use of the soft and collinear factorization theorems. The tree-level matrix element $\mathcal{M}_{m+1}(k_1, \dots, k_{m+1})$ is a function of the $m+1$ final state particle momenta k_i . Its soft and collinear singular behaviour in d dimensions can be obtained by means of soft and collinear factorization formulas. In the soft limit, when the parton momentum k_j vanishes there is the following structure:

$$|\mathcal{M}_{m+1}(k_1, \dots, k_j, \dots, k_{m+1})|^2 \rightarrow |\mathcal{M}_m(k_1, \dots, k_{m+1})|^2 \otimes_c \vec{J}^2(k_j). \quad (3.22)$$

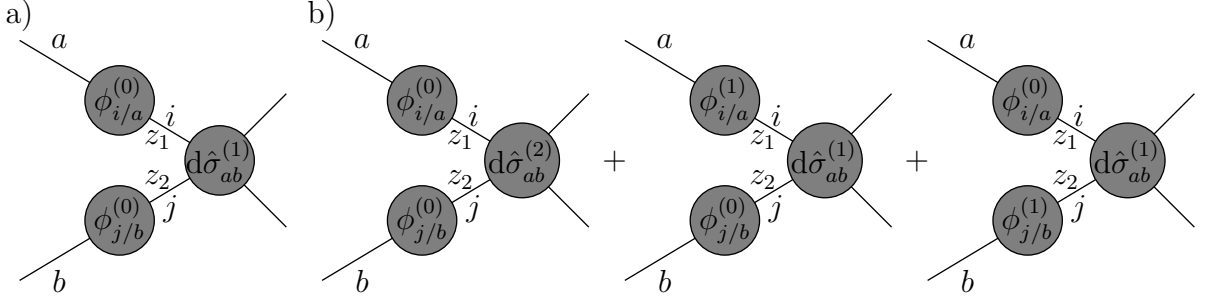


Figure 3.7: A pictorial view of a) the LO and b) the NLO contributions from the expansion of eq. (3.24).

Here, the r.h.s. contains the m final-state particle tree-level matrix-element, symbolically convoluted with the eikonal current $\vec{J}^2(k)$ for the emission of the soft particle k_j . Similarly, in the collinear limit, where the parton momenta k_i and k_j become parallel:

$$|\mathcal{M}_{m+1}(k_1, \dots, k_i, k_j, \dots, k_{m+1})|^2 \rightarrow |\mathcal{M}_m(k_1, \dots, k_j + k_i, \dots, k_{m+1})|^2 \otimes_h P_{ij} \quad (3.23)$$

where P_{ij} is the DGLAP splitting function for finding particle i in particle j . The eikonal current and the splitting functions are universal factors which do not depend on the process. They do however depend on the kinematics of the tree-level \mathcal{M}_m produced, and the eikonal current depends on the colour charges of the emitting partons, while the splitting function depends on their helicities. Equations (3.22) and (3.23) can now be used to find the subtraction term $d\sigma_3^{\text{Sub}}$. Away from the soft and singular regions, one has to make sure that momentum conservation is properly treated. Also, in the overlapping region, when k is both soft and collinear, one has to avoid to double count the subtraction.

3.2.2 Collinear Factorization at NLO

The short distance partonic cross section at NLO, $d\hat{\sigma}_{ab}$, can be expressed in the following way:

$$d\sigma_{ij}(p_1, p_2) = \sum_{ab} \int dz_1 dz_2 \phi_{i/a}(z_1) \phi_{j/b}(z_2) d\hat{\sigma}_{ab}(z_1 p_1, z_2 p_2), \quad (3.24)$$

where $p_{1,2} = x_{1,2} P_{1,2}$. The functions $\phi_{i/j}$ describe the content of parton j within parton i and are called partonic PDFs. The terms on both sides in eq. (3.24) expanded in α_s

gives:

$$d\sigma_{ij} = \sum_{n=1}^{\infty} \left(\frac{\alpha_s}{\pi}\right)^n d\sigma_{ij}^{(n)} \quad (3.25)$$

$$d\hat{\sigma}_{ab} = \sum_{n=1}^{\infty} \left(\frac{\alpha_s}{\pi}\right)^n d\hat{\sigma}_{ab}^{(n)} \quad (3.26)$$

$$\phi_{i/a}(z) = \sum_{n=0}^{\infty} \left(\frac{\alpha_s}{\pi}\right)^n \phi_{i/a}^{(n)} = \delta_{ia}\delta(1-z) - \frac{\alpha_s}{2\pi} \left(\frac{1}{\bar{\epsilon}} P_{ia}^{(1)}(z) + Q_{ia}(z)\right) + \mathcal{O}(\alpha_s^2) \quad (3.27)$$

where the delta-function in the partonic PDFs comes from the fact that at $\mathcal{O}(\alpha_s^0)$ the incoming parton a does not change. The functions $Q_{ij}(x)$ are completely arbitrary and different choices corresponds to different subtraction schemes. In the following, the $\overline{\text{MS}}$ scheme will be adopted in which $Q_{ij}(x)$ is absorbed by the definition of the parton densities and therefore put to 0 here. In this scheme, the pole part $\bar{\epsilon}$ becomes:

$$\frac{1}{\bar{\epsilon}} = \frac{1}{\epsilon} + \ln 4\pi - \gamma_E. \quad (3.28)$$

where the Euler number γ_E is defined in appendix A. The functions $P_{ij}^{(1)}(x)$ are the one loop DGLAP splitting functions for the probability of finding parton i in parton j in $4-2\epsilon$ dimensions. They are [42]:

$$P_{gg}^{(1)}(z) = 6 \left[\frac{z}{(1-z)_+} + \frac{1-z}{z} + z(1-z) \right] + \frac{33-2n_l}{6} \delta(1-z) \quad (3.29)$$

$$P_{qq}^{(1)}(z) = \frac{4}{3} \frac{1+z^2}{(1-z)_+} + 2\delta(1-z) \quad (3.30)$$

$$P_{gq}^{(1)}(z) = \frac{4}{3} \frac{1+(1-z)^2 - \epsilon z^2}{z} \quad (3.31)$$

$$P_{qg}^{(1)}(z) = \frac{1}{2} [z^2 + (1-z)^2 - 2z(1-z)\epsilon] \quad (3.32)$$

$$P_{q\gamma}^{(1)}(z) = 6P_{qg}^{(1)}(z) \quad (3.33)$$

which may be compared to eq. (1.90) and (1.96). The number of light flavours is $n_l = 3$ for charm production and $n_l = 4$ for beauty production.

The Born term is by definition the result to lowest order α_s . How to combine the different terms in eqs. (3.25)-(3.27) to reach this result is schematically shown in figure 3.7 a). The Born term is then:

$$\begin{aligned} d\sigma_{ij}^{(1)}(p_1, p_2) &= \sum_{ab} \int dz_1 dz_2 \phi_{i/a}^{(0)}(z_1) \phi_{j/b}^{(0)}(z_2) d\hat{\sigma}_{ab}^{(1)}(z_1 p_1, z_2 p_2) \\ &= \sum_{ab} \int dz_1 dz_2 \delta_{ia} \delta(1-z_1) \delta_{jb} \delta(1-z_2) d\hat{\sigma}_{ab}^{(1)}(z_1 p_1, z_2 p_2) \\ &= d\hat{\sigma}_{ij}^{(1)}(p_1, p_2) \equiv d\sigma_{ij}^{(b)}(p_1, p_2) \end{aligned} \quad (3.34)$$

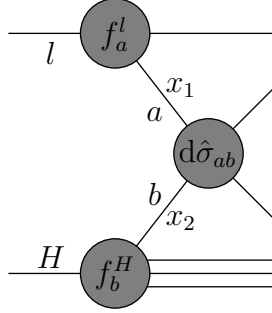


Figure 3.8: A pictorial view of the factorization described in eq. (3.36).

where in the last step (b) stands for the Born term. Similarly, the $\mathcal{O}(\alpha_s^2)$ term is obtained by combining the terms as is schematically shown in fig. 3.7 b):

$$\begin{aligned}
d\sigma_{ij}^{(2)}(p_1, p_2) &= \sum_{ab} \int dz_1 dz_2 [\phi_{i/a}^{(0)}(z_1) \phi^{(0)}(z_2) d\hat{\sigma}_{ab}^{(2)}(z_1 p_1, z_2 p_2) \\
&\quad + \phi_{i/a}^{(1)}(z_1) \phi^{(0)}(z_2) d\sigma_{ab}^{(1)}(z_1 p_1, z_2 p_2) \\
&\quad + \phi_{i/a}^{(0)}(z_1) \phi^{(1)}(z_2) d\sigma_{ab}^{(1)}(z_1 p_1, z_2 p_2)] \\
&= \sum_{ab} \int dz_1 dz_2 [\delta_{ia} \delta(1-z_1) \delta_{jb} \delta(1-z_2) d\hat{\sigma}_{ab}^{(2)}(z_1 p_1, z_2 p_2) \\
&\quad - \frac{\alpha_s}{2\pi \epsilon} P_{ia}^{(1)}(z_1) \delta_{jb} \delta(1-z_2) d\sigma_{ab}^{(1)}(z_1 p_1, z_2 p_2) \\
&\quad - \delta_{ia} \delta(1-z_1) \frac{\alpha_s}{2\pi \epsilon} P_{jb}^{(1)}(z_2) d\sigma_{ab}^{(1)}(z_1 p_1, z_2 p_2)] \\
&= d\hat{\sigma}_{ij}^{(2)}(p_1, p_2) \\
&\quad - \frac{\alpha_s}{2\pi \epsilon} \sum_a \int dz_1 P_{ia}^{(1)}(z_1) d\sigma_{aj}^{(1)}(z_1 p_1, p_2) \\
&\quad - \frac{\alpha_s}{2\pi \epsilon} \sum_b \int dz_2 P_{jb}^{(1)}(z_2) d\sigma_{bi}^{(1)}(p_1, z_2 p_2). \tag{3.35}
\end{aligned}$$

3.3 eP Cross-Sections

In this section the cross-section for the diagrams in figs.3.1-3.3 will be given. Detailed descriptions of the calculations are given in [43, 44, 39]. Here, the focus will be on the singularities in the calculations and how they are regularized [42].

For electron-proton scattering, the total cross-section is:

$$d\sigma_{eP}(P_1, P_2) = \sum_{ab} \int dx_1 dx_2 f_a^e(x_1) f_b^P(x_2) d\hat{\sigma}_{ab}(x_1 P_1, x_2 P_2), \tag{3.36}$$

where P_1 and P_2 are the momenta of the electron and proton respectively. The function $f_\gamma^e(x_1)$ describes the photon flux from the electron, when the photon takes a fraction x_1 from the electron's momentum. Similarly $f_b^P(x_2)$ describes the flux of flavour b when it takes a fraction x_2 from the proton's momentum. The sum runs over the parton flavours, which give a contribution to the partonic subprocess, $\hat{\sigma}_{ab}$ at NLO.

For heavy quarks produced in pointlike photoproduction there is the following $2 \rightarrow 2$ process, which is depicted in figs.3.1 and 3.4:

$$\gamma g \rightarrow Q\bar{Q} \quad (3.37)$$

and the following $2 \rightarrow 3$ processes, depicted in figs. 3.2 and 3.3:

$$\gamma g \rightarrow Q\bar{Q}g \quad (3.38)$$

$$\gamma q \rightarrow Q\bar{Q}q \quad (3.39)$$

$$\gamma \bar{q} \rightarrow Q\bar{Q}\bar{q} \quad (3.40)$$

Kinematics for the $2 \rightarrow 2$ Process

For the two-body interaction, the notation with barred symbols is used. The incoming massless momenta are \bar{p}_1 and \bar{p}_2 , and the outgoing heavy quark momenta are \bar{k}_1 and \bar{k}_2 , such that the process may be written $\bar{p}_1 + \bar{p}_2 \rightarrow \bar{k}_1 + \bar{k}_2$. The momentum fractions of the incoming partons are \bar{x}_1 and \bar{x}_2 , such that:

$$\bar{p}_{1,2} = \bar{x}_{1,2}P_{1,2} \quad (3.41)$$

where $P_{1,2}$ are the beam momenta. The two-body invariants are, as in eq. (1.97) the modified Mandelstam variables:

$$\begin{aligned} \bar{s} &= (\bar{p}_1 + \bar{p}_2)^2 = 2\bar{p}_1\bar{p}_2 \\ \bar{t} &= (\bar{p}_1 - \bar{k}_1)^2 - m^2 = -2\bar{p}_1\bar{k}_1 \\ \bar{u} &= (\bar{p}_1 - \bar{k}_2)^2 - m^2 = -2\bar{p}_1\bar{k}_2. \end{aligned} \quad (3.42)$$

Here m is the heavy quark mass. Then $\bar{s} + \bar{t} + \bar{u} = 0$ and $\bar{s} = \bar{x}_1\bar{x}_2S$, where $S = (P_1 + P_2)^2$ is the overall center of mass energy squared. In the center of mass frame of the $2 \rightarrow 2$ process, the four-momenta can be written as:

$$\begin{aligned} \bar{p}_{1,2} &= \bar{E}(1, 0, 0, \pm 1) \\ \bar{k}_{1,2} &= (\bar{E}, \pm \bar{k}_T, 0, \pm \bar{k}_L) \end{aligned} \quad (3.43)$$

and

$$\begin{aligned} \bar{s} &= \bar{E}^2 \\ \bar{t} &= -2\bar{E}(\bar{E} - \bar{k}_L) \\ \bar{u} &= -2\bar{E}(\bar{E} + \bar{k}_L). \end{aligned} \quad (3.44)$$

The heavy quark velocity $\bar{\beta}$ is:

$$\bar{\beta} = \sqrt{1 - \frac{4m^2}{\bar{s}}}. \quad (3.45)$$

In this system the scattering angle $\bar{\theta}$ is also defined. Then

$$\begin{aligned} \bar{t} &= -\frac{1}{2}\bar{s}(1 - \bar{\beta} \cos \bar{\theta}) \\ \bar{u} &= -\frac{1}{2}\bar{s}(1 + \bar{\beta} \cos \bar{\theta}) \end{aligned} \quad (3.46)$$

Kinematics for the $2 \rightarrow 3$ Processes

For the $2 \rightarrow 3$ processes unbarred symbols are used. The incoming momenta are p_1 and p_2 and the outgoing heavy quark and antiquark momenta are k_1 and k_2 respectively, while the outgoing light parton has momentum k , such that $p_1 + p_2 \rightarrow k_1 + k_2 + k$. The momentum fractions of the incoming partons are denoted x_1 and x_2 such that

$$p_{1,2} = x_{1,2}P_{1,2}. \quad (3.47)$$

For the three-body processes there are five independent invariants:

$$\begin{aligned} s &= 2p_1p_2 \\ t_1 &= (p_1 - k_1)^2 - m^2 = -2p_1k_1 \\ t_2 &= (p_2 - k_2)^2 - m^2 = -2p_2k_2 \\ u_1 &= (p_1 - k_2)^2 - m^2 = -2p_1k_2 \\ u_2 &= (p_2 - k_1)^2 - m^2 = -2p_2k_1. \end{aligned} \quad (3.48)$$

Then $s = x_1x_2S$. It is also convenient to define

$$\begin{aligned} v_1 &= -2p_1k \\ v_2 &= -2p_2k \end{aligned} \quad (3.49)$$

and

$$\begin{aligned} w_1 &= 2k_1k \\ w_2 &= 2k_2k \end{aligned} \quad (3.50)$$

These variables are not independent, since

$$\begin{aligned} s + t_1 + u_1 + v_1 &= s + t_2 + u_2 + v_2 = 0, \\ s + t_1 + u_2 - w_2 &= s + t_2 + u_1 - w_1 = 0. \end{aligned} \quad (3.51)$$

3.3.1 A Description of the Calculation

In order to perform the calculation of the diagrams in figs.3.1-3.3 all singularities have to be dealt with. There are two types of singularities present, ultra-violet (UV) and infra-red (IR). The UV singularities are present in the diagrams in fig. 3.5 and the IR singularities are present in both the virtual diagrams in fig. 3.4 and in the real emission diagrams in figs.3.2 and 3.3. To make the cross-section UV safe, the poles are canceled by renormalizing the coupling α_s and the masses of the light parton in the loop, as described in section 1.1.1 and appendix A. The UV-singularities will not be considered in the following. The IR divergencies come in two types: soft and collinear. When computing the diagrams with dimensional regularization in $n = 4 - 2\epsilon$ dimensions all IR divergencies appear as $1/\epsilon$ poles. All diagrams with an emitted gluon (real or virtual) give rise to a soft singularity when the gluon energy becomes zero. Also, for the real diagrams with emissions from the incoming particles there are collinear singularities when the emitted parton is at an angle θ such that $y \equiv \cos \theta = \pm 1$.

The $\gamma g \rightarrow Q\bar{Q}g$ processes

For the real emission diagrams for the $\gamma g \rightarrow Q\bar{Q}g$ process (fig. 3.2) the cross-section is given by [42]:

$$d\sigma_{\gamma g}^{(r)} = \mathcal{M}_{\gamma g}^{(r)}(s, v_1, v_2, t_1, t_2) d\phi_3. \quad (3.52)$$

The three-body phase-space $d\phi_3$ can be expressed in terms of the two-body phase-space $d\phi_2(s)$ as:

$$d\phi_3 = \left(1 - \frac{\pi^2}{3}\epsilon^2\right) (4\pi)^{\epsilon-2} \Gamma(1+\epsilon) \frac{s^{1-\epsilon}}{2\pi} (1-x)^{1-2\epsilon} (1-y^2)^{-\epsilon} dy \sin^{2\epsilon} \theta_2 d\theta_2 d\phi_2(xs) \quad (3.53)$$

where $\Gamma(n)$ is Euler's gamma function described in appendix A.

The leading soft singularity in the invariant cross section, eq. (3.52), behaves as $1/(1-x)^2$ and the collinear singularity for $y = -1$ behaves as $1/(1-y^2)$. Therefore is the function

$$f_{\gamma g}(x, y, \theta_1, \theta_2) = s^2(1-x)^2(1-y^2) \mathcal{M}_{\gamma g}^{(r)}(s, v_1, v_2, t_1, t_2) \quad (3.54)$$

regular for $y = -1$ and $x = 0$. When substituting eqs. (3.53) and (3.54) into eq. (3.52), the real emission cross section becomes:

$$\begin{aligned} d\sigma_{\gamma g}^{(r)} &= \left(1 - \frac{\pi^2}{3}\epsilon^2\right) (4\pi)^{\epsilon-2} \Gamma(1+\epsilon) \frac{s^{-1-\epsilon}}{2\pi} (1-x)^{-1-2\epsilon} (1-y^2)^{-1-\epsilon} \\ &\times dy \sin^{2\epsilon} \theta_2 d\theta_2 d\phi_2(xs) f_{\gamma g}(x, y, \theta_1, \theta_2). \end{aligned} \quad (3.55)$$

This expression can be expanded in ϵ , using

$$(1-x)^{-1-2\epsilon} = -\frac{\tilde{\beta}^{-4\epsilon}}{2\epsilon}\delta(1-x) + \left(\frac{1}{1-x}\right)_{\tilde{\rho}} - 2\epsilon \left(\frac{\log(1-x)}{1-x}\right)_{\tilde{\rho}} + \mathcal{O}(\epsilon^2) \quad (3.56)$$

$$(1-y^2)^{-1-\epsilon} = -[\delta(1+y) + \delta(1-y)]\frac{(2\omega)^{-\epsilon}}{2\epsilon} + \frac{1}{2} \left[\left(\frac{1}{1-y}\right)_{\omega} + \left(\frac{1}{1+y}\right)_{\omega} \right] + \mathcal{O}(\epsilon), \quad (3.57)$$

where the distributions in round brackets are defined according to the prescriptions:

$$\begin{aligned} \int_{\tilde{\rho}}^1 h(x) \left(\frac{1}{1-x}\right)_{\tilde{\rho}} dx &= \int_{\tilde{\rho}} \frac{h(x) - h(1)}{1-x} dx \\ \int_{\tilde{\rho}}^1 h(x) \left(\frac{\log(1-x)}{1-x}\right)_{\tilde{\rho}} dx &= \int_{\tilde{\rho}} [h(x) - h(1)] \frac{\log(1-x)}{1-x} dx \\ \int_{1-\omega}^1 h(y) \left(\frac{1}{1-y}\right)_{\omega} dy &= \int_{1-\omega} \frac{h(y) - h(1)}{1-y} dy \\ \int_{-1}^{-1+\omega} \left(\frac{1}{1+y}\right)_{\omega} dy &= \int_{-1}^{-1+\omega} \frac{h(y) - h(-1)}{1+y} dy \end{aligned} \quad (3.58)$$

for any test function $h(x)$. Here $\tilde{\beta} = \sqrt{1-\tilde{\rho}}$ and $\tilde{\rho}$ and ω are parameters which should be chose within the ranges

$$\frac{4m^2}{s} \leq \tilde{\rho} < 1, \quad 0 < \omega \leq 2. \quad (3.59)$$

When substituting eqs. (3.56) and (3.57) into eq. (3.55), the soft and collinear singular pieces and the regular piece in the real cross section may be separated. The real cross section then becomes:

$$d\sigma_{\gamma g}^{(r)} = d_{\gamma g}^{(s)} + d\sigma_{\gamma g}^{(c-)} + d\sigma_{\gamma g}^{(f)}. \quad (3.60)$$

where (s) denotes the soft piece, (c-) denotes the collinear piece for $y = -1$ and (f) denotes the regular piece.

Here the collinear part is:

$$\begin{aligned} d\sigma_{\gamma g}^{(c-)} &= (4\pi)^{-2+\epsilon} \Gamma(1+\epsilon) d\phi_2(xs) \frac{s^{-1-\epsilon}}{2\pi} dy \sin^{-2\epsilon} \theta_2 d\theta_2 \left[\left(\frac{1}{1-x}\right)_{\tilde{\rho}} - \epsilon \left(\frac{\log(1-x)}{1-x}\right)_{\tilde{\rho}} \right] \\ &\times \left[-\frac{(2\omega)^{-\epsilon}}{2\epsilon} \delta(1+y) \right] f_{\gamma g}(x, y, \theta_1, \theta_2). \end{aligned} \quad (3.61)$$

In the collinear limit $y = -1$, it has been shown that $f_{\gamma g}(x, -1, \theta_1, \theta_2)$ may be expressed as [39]:

$$f_{\gamma g}(x, -1, \theta_1, \theta_2) = f_{\gamma g}^{(c-)}(x, \theta_1) + \tilde{f}_{\gamma g}^{(c-)}(x, \theta_1, \theta_2) \quad (3.62)$$

where $\tilde{f}_{\gamma g}^{(c-)}(x, \theta_1, \theta_2)$ has the property that

$$\int_0^\pi \tilde{f}_{\gamma g}^{(c-)}(x, \theta_1, \theta_2) \sin^{-2\epsilon} \theta_2 d\theta_2 = 0. \quad (3.63)$$

The function $f_{\gamma g}^{(c-)}$ is given by

$$f_{\gamma g}^{(c-)}(x, \theta_1) = 64\pi 3\alpha_s^{(b)} s(1-x) \left[\frac{x}{1-x} + \frac{1-x}{x} + x(1-x) \right] \mathcal{M}_{\gamma g}^{(b)}(xs, t_1) \quad (3.64)$$

The term in the square bracket is the DGLAP splitting function $P_{gg}(x)$, defined in eq. 1.90. Substituting eqs. (3.62) and (3.64) into eq. (3.61) and performing the y and θ_2 integration, such that $\tilde{f}_{\gamma g}^{(c-)}(x, \theta_1, \theta_2)$ drops out, the collinear piece become:

$$\begin{aligned} d\sigma_{\gamma g}^{(c-)} &= -\frac{s}{\bar{\epsilon}} \left(\frac{2}{\omega} \right)^\epsilon \frac{3\alpha_s^{(b)}}{\pi} \left[\left(\frac{1}{1-x} \right)_{\bar{\rho}} - 2\epsilon \left(\frac{\log(1-x)}{1-x} \right)_{\bar{\rho}} \right] \\ &\quad \times (1-x) P_{gg}(x) \mathcal{M}_{\gamma g}^{(b)}(xs, t_1) d\phi_2(xs) \end{aligned} \quad (3.65)$$

which comes from the small ϵ limit of the $\Gamma(1+\epsilon)$ term. Here, $\mathcal{M}_{\gamma g}^{(b)}(xs, t_1) d\phi_2(xs)$ is the Born term in eq. (3.34), expressed in $2 \rightarrow 3$ variables.

In eq. (3.65) there is a $1/\bar{\epsilon}$ pole which has to be regularized. From eq. (3.35), the total short distance cross-section for the process $\gamma g \rightarrow Q\bar{Q}g$ at NLO then becomes

$$\begin{aligned} d\hat{\sigma}_{\gamma g}(p_1, p_2) &= d\hat{\sigma}_{\gamma g}^{(1)} + d\hat{\sigma}_{\gamma g}^{(2)}(p_1, p_2) \\ &= d\sigma_{\gamma g}^{(b)} + d\sigma_{\gamma g}^{(2)} + \frac{\alpha_s}{2\pi \bar{\epsilon}} dz_2 P_{gg}^{(1)}(z_2) \mathcal{M}_{\gamma g}^{(b)}(z_2 s, t) d\phi_2(x) \\ &= d\sigma_{\gamma g}^{(b)} + d\sigma_{\gamma g}^{(v)} + d\sigma_{\gamma g}^{(r)} + \frac{\alpha_s}{2\pi \bar{\epsilon}} dz_2 P_{gg}^{(1)}(z_2) \mathcal{M}_{\gamma g}^{(b)}(z_2 s, t) d\phi_2(x) \\ &= d\sigma_{\gamma g}^{(b)} + d\sigma_{\gamma g}^{(v)} + d\sigma_{\gamma g}^{(s)} + d\sigma_{\gamma g}^{(c-)} + d\sigma_{\gamma g}^{(f)} \\ &\quad + \frac{\alpha_s}{2\pi \bar{\epsilon}} dz_2 P_{gg}^{(1)}(z_2) \mathcal{M}_{\gamma g}^{(b)}(z_2 s, t) d\phi_2(x) \end{aligned} \quad (3.66)$$

where eq. (3.60) has been used in the last step. The collinear singularities in eq. (3.65) are now canceled by the $1/\bar{\epsilon}$ pole explicitly present here. Therefore, the last term here has the properties needed for a subtraction term: it cancels the singularities locally and it is integrated over the 1 parton subspace. The remaining soft singularities in $d\hat{\sigma}_{\gamma g}^{(s)}$ are canceled by the singularities in the virtual contribution $d\sigma_{\gamma g}^{(v)}$, such that the term

$$d\sigma_{\gamma g}^{(sv)} = d\hat{\sigma}_{\gamma g}^{(s)} + d\sigma_{\gamma g}^{(v)} \quad (3.67)$$

is finite for $\epsilon \rightarrow 0$.

The $\gamma\bar{q} \rightarrow Q\bar{Q}\bar{q}$ Processes

For the process $\gamma q(\bar{q}) \rightarrow Q\bar{Q}q(\bar{q})$, the diagrams contributing to the calculation are the diagrams in fig. 3.3. The calculation of these diagrams is performed in the same steps as for the $\gamma g \rightarrow Q\bar{Q}g$, described above. The difference is that in this process, there are no soft singular piece, since there is no gluon emission present. On the other hand, there is a collinear singular piece associated with the incoming photon, where $y = 1$, not present in the previously described process. Following the same steps in going from eq. (3.52) to eq. (3.60), this cross section can be expressed as

$$d\sigma_{\gamma q}^{(r)} = d\sigma_{\gamma q}^{(c+)} + d\sigma_{\gamma q}^{(c-)} + d\sigma_{\gamma q}^{(f)}. \quad (3.68)$$

Here, the collinear pieces becomes

$$\begin{aligned} d\sigma_{\gamma q}^{(c\pm)} &= (4\pi)^{-2+\epsilon}\Gamma(1+\epsilon)\frac{s^{-1-\epsilon}}{4\epsilon}\left(\frac{2}{\omega}\right)^\epsilon\left[\left(\frac{1}{1-x}\right)_{\bar{\rho}} - 2\epsilon\left(\frac{\log(1-x)}{1-x}\right)_{\bar{\rho}}\right] \\ &\times f_{\gamma q}^{(c\pm)}(x, \theta_1)d\phi_2(xs) \end{aligned} \quad (3.69)$$

where the functions $f_{\gamma q}^{(c\pm)}(x, \theta_1)$ are given by

$$f_{\gamma q}^{(c+)}(x, \theta_1) = 32\pi\alpha_{\text{EM}}e_q^2s(1-x)P_{q\gamma}(x)\mathcal{M}_{q\bar{q}}^{(b)}(xs, t_2) \quad (3.70)$$

$$f_{\gamma q}^{(c-)}(x, \theta_1) = 32\pi\alpha_s s(1-x)P_{gq}(x)\mathcal{M}_{\gamma g}^{(b)}(xs, t_1). \quad (3.71)$$

Here e_q is the charge of the emitted light quark and $\mathcal{M}_{q\bar{q}}^{(b)}(s, t)$ is the Born invariant cross section for $q\bar{q} \rightarrow Q\bar{q}$. The $1/\epsilon$ singularity in eq. (3.69) has to be regularized.

The $\gamma q \rightarrow Q\bar{Q}q$ cross-section in eq. (3.35) is:

$$\begin{aligned} d\sigma_{\gamma q}^{(2)}(p_1, p_2) &= d\hat{\sigma}_{\gamma q}^{(2)}(p_1, p_2) - \frac{\alpha_s}{2\pi}\frac{1}{\bar{\epsilon}}\int dz_1 P_{q\gamma}^{(1)}(z_1)\mathcal{M}_{q\bar{q}}^{(b)}(z_1 p_1, p_2)d\phi_2(z_1 s) \\ &\quad - \frac{\alpha_s}{2\pi}\frac{1}{\bar{\epsilon}}\int dz_2 P_{gq}^{(1)}(z_2)\mathcal{M}_{\gamma g}^{(b)}(p_1, z_2 p_2)d\phi_2(z_2 s) \end{aligned} \quad (3.72)$$

For $\gamma\bar{q} \rightarrow Q\bar{Q}\bar{q}$, the contributions are equivalent, with the substitution $q \leftrightarrow \bar{q}$.

The total short distance cross section for this process then becomes:

$$\begin{aligned} d\hat{\sigma}_{\gamma q}(p_1, p_2) &= d\hat{\sigma}_{\gamma q}^{(2)}(p_1, p_2) \\ &= d\sigma_{\gamma q}^{(2)}(p_1, p_2) + \frac{\alpha_s}{2\pi}\frac{1}{\bar{\epsilon}}\int dz_1 P_{q\gamma}^{(1)}(z_1)\mathcal{M}_{q\bar{q}}^{(b)}(z_1 p_1, p_2)d\phi_2(z_1 s) \\ &\quad + \frac{\alpha_s}{2\pi}\frac{1}{\bar{\epsilon}}\int dz_2 P_{gq}^{(1)}(z_2)\mathcal{M}_{\gamma g}^{(b)}(p_1, z_2 p_2)d\phi_2(z_2 s)d\sigma_{\gamma q}^{(2)}(p_1, p_2) \\ &= d\sigma_{\gamma q}^{(c+)} + d\sigma_{\gamma q}^{(c-)} + d\sigma_{\gamma q}^{(f)} \\ &\quad + \frac{\alpha_s}{2\pi}\frac{1}{\bar{\epsilon}}\int dz_1 P_{q\gamma}^{(1)}(z_1)\mathcal{M}_{q\bar{q}}^{(b)}(z_1 p_1, p_2)d\phi_2(z_1 s) \\ &\quad + \frac{\alpha_s}{2\pi}\frac{1}{\bar{\epsilon}}\int dz_2 P_{gq}^{(1)}(z_2)\mathcal{M}_{\gamma g}^{(b)}(p_1, z_2 p_2)d\phi_2(z_2 s) \end{aligned} \quad (3.73)$$

The collinear singularities for $y = \pm 1$ are canceled by the first and second integral respectively, which are used as the subtraction terms.

3.4 Calculating Total and Differential Cross-sections at NLO

In order to evaluate the integral 3.20 numerically, the Monte Carlos methods described in chapter 2 cannot be used. The reason for this is that in the MC method, the integral being evaluated is treated as a probability distribution. In the NLO cross-section the function being integrated over is not positive everywhere. Therefore it cannot be treated as a probability distribution.

To numerically compute both the total NLO cross-section and also differential cross-sections, a method using weights may be used. Writing the integral symbolically as:

$$\sigma_{\text{NLO}}^{\text{sub}} = \int_{m+1} d\phi_{m+1} \mathcal{R}_{\text{sub}}(\phi_{m+1}) + \int_m d\phi_m \mathcal{V}_{\text{sub}}(\phi_m) + \int_m d\phi_m \mathcal{B}(\phi_m) \quad (3.74)$$

where the integrands are functions of sets of phase-space variables ϕ_i for m and $m + 1$ parton final states. To evaluate the integral, the phase-space coordinates are randomly and uniformly sampled over their whole range. Each sampled point $\phi_{m+1}^{(i)}$ or $\phi_m^{(j)}$ is then given a weight $w^{(i)} = \mathcal{R}_{\text{sub}}(\phi_{m+1}^{(i)})$ or $w_{\text{V}}^{(j)} = \mathcal{V}_{\text{sub}}(\phi_m^{(j)})$ and $w_{\text{B}}^{(j)} = \mathcal{B}(\phi_m^{(j)})$. The weights $w_{\text{V}}^{(j)}$ are in general negative, while the other weights are positive. The estimate of the total cross-section then becomes a weighted sum over all the sampled points in respective phase-space:

$$\begin{aligned} \sigma_{\text{NLO}}^{\text{sub}} &\simeq \sum_{\text{Sampled points } i} \mathcal{R}_{\text{sub}}(\phi_{m+1}^{(i)}) + \sum_{\text{Sampled points } j} (\mathcal{V}_{\text{sub}}(\phi_m^{(j)}) + \mathcal{B}(\phi_m^{(j)})) \quad (3.75) \\ &= \sum_i w^{(i)} + \sum_j (w_{\text{V}}^{(j)} + w_{\text{B}}^{(j)}) \end{aligned}$$

The differential distributions may then be obtained by filling histograms which are binned in phase-space, with the weights $w^{(i)}$, $w_{\text{V}}^{(j)}$ and $w_{\text{B}}^{(j)}$.

3.5 Dipole Subtraction

Another way of finding subtraction terms is the so called Catani-Seymour subtraction [41]. Instead of using the forms in eq. (3.22) and (3.23), one may use the dipole factorization formula:

$$|\mathcal{M}_{m+1}(k_1, \dots, k_{m+1})|^2 \rightarrow |\mathcal{M}_m(\tilde{k}_1, \dots, \tilde{k}_m)|^2 \otimes V_{ij} + \text{non singular terms} \quad (3.76)$$

where the non singular terms are regular for $k_i \cdot k_j \rightarrow 0$. As for the collinear splitting functions, the dipole splitting functions are universal, i.e. process independent. These dipole splitting functions describe the probability of two particles splitting into three, and include an emitter, an emitted particle and a spectator. The parton momenta \tilde{k}_i are defined by:

$$\begin{aligned}\tilde{k}_i^2 &= 0 \\ \tilde{k}_1 + \dots + \tilde{k}_m &= k_1 + \dots + k_{m+1}\end{aligned}\tag{3.77}$$

The first condition demands that the outgoing partons are on mass-shell (it has to be modified for heavy quarks), and the second condition conserves four-momentum.

The subtraction terms may then be written:

$$\int_{m+1} d\sigma_{m+1}^{\text{Sub}} = \sum_{\text{dipoles } ij} \int_m d\phi_m d\sigma^{\text{Born}} \times \int_1 dV_{ij}\tag{3.78}$$

where the sum goes over all dipoles in the $m + 1$ final state. In a $2 \rightarrow 1$ process there is one dipole, in a $2 \rightarrow 2$ process there are 2 dipoles etc.

Chapter 4

Monte Carlo at Next-to-leading Order

In this chapter, the next-to-leading order (NLO) calculation described in chapter 3, will be supplemented with a parton shower to all orders in α_s . In chapter 3 it is described how the intermediate divergencies in the NLO calculation are regulated with the subtraction method. The resulting cross-section may be written in the form:

$$\sigma_{\text{NLO}}^{\text{sub}} = \int_{m+1} d\phi_{m+1} \mathcal{R}_{\text{sub}}(\phi_{m+1}) + \int_m d\phi_m \mathcal{V}_{\text{sub}}(\phi_m) + \int_m d\phi_m \mathcal{B}(\phi_m) \quad (4.1)$$

where \mathcal{R}_{sub} and \mathcal{V}_{sub} denote the real emissions and virtual contribution respectively, both with the all IR divergencies subtracted, and \mathcal{B} denotes the Born term. Here, $d\Phi(i)$ denotes the phase-space for i final state partons.

When adding a parton shower to this NLO calculation, some $m + 1$ particle final state configurations will also be generated by the m particle final state configuration, together with the first branching in the parton shower. If not done properly, these configurations will then be doubly counted. In this chapter it will be explained how the subtraction method may be modified when adding a parton shower to the NLO-calculation. This will lead to the need to construct so called Monte Carlo subtraction terms, which will be used to cancel any intermediate IR divergencies, as well as the double counting of some configurations. The concepts of modified subtraction will be introduced in the framework of the toy model presented in chapter 3.1. The NLO matrix-element combined with a parton shower is called an MC@NLO. The goal of this chapter is to find the Monte Carlo subtraction terms needed to combine the process of heavy quarks produced in photoproduction, with the HERWIG parton shower, which was described in chapter 2.3. The construction of an MC@NLO for this process is the topic of this thesis. As such, it will be the first MC@NLO for a process in electron proton scattering.

4.1 A Toy Monte Carlo at Next-to-leading Order

In this section the toy model introduced in chapter 3.1 will be supplied by a parton shower, based on the Monte Carlo methods described in chapter 2. The NLO cross-section in the toy model, is given by:

$$\sigma_{\text{NLO}} = B + a \left(\frac{B}{2\epsilon} + V \right) + a \int_0^1 \frac{R(x)}{x} dx \quad (4.2)$$

The system may undergo any number of further emissions in a parton shower, with emission probabilities controlled by the Sudakov formfactor. For this toy model, it is defined as:

$$\Delta(x_1, x_2) = \exp \left[-a \int_{x_1}^{x_2} dz P_\gamma(z) \right], \quad (4.3)$$

where $P_\gamma(z)$ is a splitting function giving the probability that a particle emits a photon taking a fraction z of the particle's energy. The Sudakov formfactor gives the probability of having no emission between the energies x_1 and x_2 . The function $zP_\gamma(z)$ is monotonic and has the following properties:

$$0 \leq zP_\gamma(z) \leq 1, \quad \lim_{z \rightarrow 0} zP_\gamma(z) = 1, \quad \lim_{z \rightarrow 1} zP_\gamma(z) = 0. \quad (4.4)$$

The third condition means that no further emission is possible if the photon takes the full energy of the emitting particle, and the second condition implies that the emission becomes very likely for small z . As before, a has the meaning of a coupling, and when $a \rightarrow 0$ the Sudakov formfactor tends to 1, i.e. the probability for a branching tends to 0. When $a \rightarrow \infty$ then $\Delta(x_1, x_2) \rightarrow 0$, which means a branching becomes inevitable.

The conditions in eq. (4.4) mean that the function $G(z) = 1/z$ is larger than, or equal to $P_\gamma(z)$, which means that this function can be used in the veto algorithm, described in appendix B, to generate a final state parton-shower. To do this the maximum energy x_M available for the first branching has to be defined as well as a cut-off scale x_0 . In this way, the emissions are ordered in x .

Matching the NLO-Matrix Element and the Parton Shower

When generating Monte Carlo events in a parton shower, one needs a starting scale as well as a well defined initial parton configuration. In conventional Monte Carlos, with a leading order matrix element, this is always the case. In the NLO cross-section, there is no well defined parton configuration, nor a well defined starting scale x_{max} . This comes from the fact that two different configurations are calculated. In the toy-model, the real emission part gives a 2 parton configuration from which the parton-shower then begins with an $x_{\text{max}} < 1$, while the Born and virtual parts of the calculation gives a

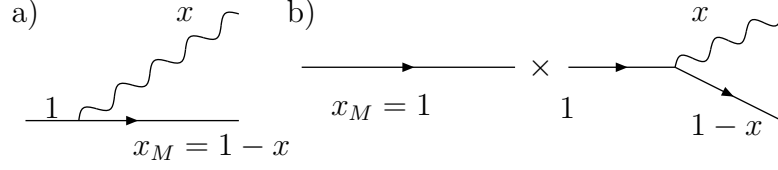


Figure 4.1: A pictorial view of double counting. a) shows the real emission matrix element contributions. Some of those contributions can also be produced by the virtual or, as shown in b), the Born contribution supplemented by one emitted photon in the parton shower. Therefore some of these configuration risk to be doubly counted. The maximum energy available for photon radiation in the parton shower is in a) $x_{\max}(x) < 1$ and in b) $x_{\max} = 1$. How to deal with double counting is explained in the text.

1 parton configuration, with $x_{\max} = 1$, as is the case for the LO MC. If one just adds the parton shower onto the NLO-configuration produced, one risks to double count some configurations, since some of the 2 particle configurations coming from the real emissions may also be produced by the 1 particle configurations combined with the first emission from the parton shower. This is illustrated in fig.4.1.

For a leading order Monte Carlo, the probability of having the two particle configuration is given by the Born term times the parton-shower at the first order in the coupling a :

$$\begin{aligned} \mathcal{P}(\text{First branching})_{\text{MC@LO}}(x) &= B \otimes \mathcal{P}(\text{Branching at } x) = aBP_\gamma(x)\Delta(x_{\max}, x) \\ &= aBP_\gamma(x) + \mathcal{O}(a^2), \end{aligned} \quad (4.5)$$

where, in the toy model, $x_{\max} = 1$. Here, the Sudakov formfactor has been expanded in the coupling, such that

$$\Delta(x_1, x_2) = 1 - a \int_{x_1}^{x_2} P_\gamma(z)dz + \mathcal{O}(a^2) \quad (4.6)$$

and only the first term has been kept.

At NLO, in order to provide a well defined parton state for the parton shower to begin from, the subtraction method described in chapter 3.1 may be modified, such that the first emission in the parton shower is subtracted from the real emissions:

$$\sigma_R^{\text{msub}} = a \int_0^1 \left(\frac{R(x)}{x} - BP_\gamma(x) \right) dx \quad (4.7)$$

This integral is regular by the second condition in eq. (4.4). Here, $aBP_\gamma(x)$ is called a Monte Carlo subtraction term and it should be added to the virtual part to cancel the divergencies there:

$$\begin{aligned} \sigma_V^{\text{msub}} &= \int_0^1 \left(a\frac{B}{2\epsilon} + V \right) \delta(x)dx + \int_0^1 aBP_\gamma(x)dx = a \left(\frac{B}{2\epsilon} + V \right) + aB \int_0^1 P_\gamma(x)dx \\ &= aV + aB \left(\frac{1}{2\epsilon} + \int_0^1 P_\gamma(x)dx \right) = aV + aB \int_0^1 \left(P_\gamma(x) - \frac{1}{x} \right) dx \end{aligned} \quad (4.8)$$

which is regular. In the last step, dimensional regularization, described in appendix A, has been used backwards. The total NLO cross-section, given by modified subtraction is then:

$$\begin{aligned} \sigma_{\text{NLO}}^{\text{msub}} &= a \int_0^1 \left(\frac{R(x)}{x} - BP_\gamma(x) \right) dx \\ &+ \int_0^1 \left((B + aV)\delta(x) + aB \left(P_\gamma(x) - \frac{1}{x} \right) \right) dx. \end{aligned} \quad (4.9)$$

A subtle, but important, difference between the modified subtraction method and the normal subtraction method, is emerging when the expectation value of an observable before the parton shower is applied, is taken into account. In Monte Carlo event generators, the expectation value of many observables will be dependent on the parton shower. The parton-shower is dependent on its starting scale x_{max} as well as its cut-off scale x_0 . This means that in general, the expectation value of an observable O is dependent upon these scales as well. In modified subtraction, the expectation value of an observable $O(x, x_{\text{max}})$, before the parton shower, is thus:

$$\begin{aligned} \langle O(x, x_{\text{max}}) \rangle &= a \int_0^1 O(x, x_{\text{max}}(x)) \left(\frac{R(x)}{x} - BP_\gamma(x) \right) dx \\ &+ \int_0^1 O(x, 1) \left((B + aV)\delta(x) + aB \left(P_\gamma(x) - \frac{1}{x} \right) \right) dx \end{aligned} \quad (4.10)$$

The dependence on the starting scale x_{max} of the observables is what makes modified subtraction different from normal subtraction. In the toy model, what is subtracted from the real emission is $aO(x, x_{\text{max}}(x))BP_\gamma(x)$, where $x_{\text{max}}(x) < 1$, and what is added to the real part is $aO(x, 1)BP_\gamma(x)$, which is not necessarily equal. This difference will not contribute to the total NLO cross-section, since it only depends on the parton shower, which does not alter the total cross-section. The difference between these two terms is then compensated in the parton shower evolution, by later branchings.

In the modified subtraction, the subtraction term used is directly dependent upon the parton shower, which means that if they are combined with another parton shower, configurations will be doubly counted. Also, only the parts of phase-space which are actively filled by the parton shower should be subtracted. If, for example, the parton shower contains a dead region, $x_{\text{dead}} \leq x \leq 1$, where no emissions are allowed, the real emissions should not be modified in this region. The Monte Carlo subtraction term then becomes:

$$BP_\gamma(x)\theta(x - x_{\text{dead}}). \quad (4.11)$$

4.2 MC@NLO for eP scattering

In order to construct an MC@NLO for electron proton scattering, the Monte Carlo subtraction terms has to be found. These terms are dependent both on which process they

are used for and the parton shower. In this section, the NLO calculation presented in chapter 3 will be modified such that it can be matched with the HERWIG parton shower, described in chapter 2.3. In order to construct the Monte Carlo subtraction terms in QCD, some further subtleties not present in the toy model, has to be considered.

Not only real emissions are doubly counted in the parton shower. The DGLAP splitting functions also contain virtual resummation to all orders in α_s , and the one loop contribution will therefore reproduce the NLO virtual contribution when the parton shower is attached to the Born term. These are therefore also subtracted.

For technical reasons, two kinds of variable transformations are needed. The HERWIG parton shower is defined in the showering variables ξ and z , while the NLO matrix element is defined in the kinematic variables described in chapter 3.3. In order to subtract the first parton shower branching from the real emissions, the HERWIG showering variables therefore need to be expressed in terms of the real emission $2 \rightarrow 3$ configuration invariants.

These terms are then added back to the virtual contribution. Therefore, the invariants for the $2 \rightarrow 2$ configuration also need to be expressed in terms of $2 \rightarrow 3$ invariants. In general, there is no unique projection of the $2 \rightarrow 2$ variables onto the $2 \rightarrow 3$ ones. However, one subtlety of the parton shower fixes this projection. When the outgoing partons radiate in the final state parton shower, they get pushed off mass-shell, by recoils. At the end of the parton shower, the momentum of all partons are reshuffled in a way such that four momenta are conserved. In HERWIG there are two ways of doing this, one which keeps longitudinal momentum of the $Q\bar{Q}$ pair fixed and one which keeps the rapidity of the pair fixed. This extra constraint fixes the projection of the $2 \rightarrow 2$ variables onto the $2 \rightarrow 3$ ones.

In the HERWIG parton shower there are both dead zones and dead regions as defined in chapter 2.3.1. In these kinematic regions, the parton shower does not branch and they should therefore not be subtracted from the matrix element. As in the toy-model these regions are taken out of the MC subtraction by θ -functions.

The MC subtraction terms will have a similar form as the NLO subtraction terms found in the collinear factorization in chapter 3.2.2 (and as in the toy model). For each possible branching by the parton shower they will include a DGLAP splitting function for the branching, multiplied by a Born cross-section for the process without branching. To this the θ -functions for the dead regions are attached.

In the following subsection, item number 3 above will be addressed, by defining the $2 \rightarrow 2$ kinematic variables in terms of the $2 \rightarrow 3$ ones. Also, the momentum reshuffling will be considered there. Then, in section 4.2.2, the HERWIG variables will be expressed in terms of the $2 \rightarrow 3$ variables. In section 4.2.3 the MC subtraction terms for heavy quarks produced in photoproduction will be written down.

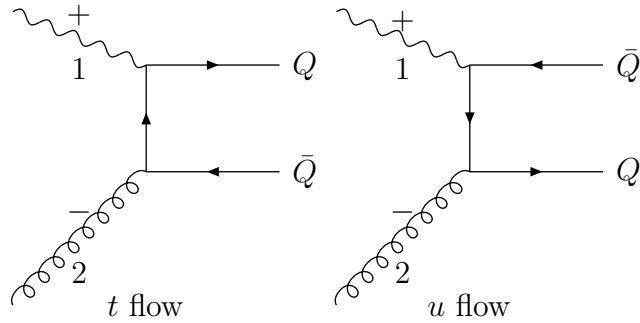


Figure 4.2: An over view of some of the notations used in this chapter. The electron-side is denoted $+$. From there particle 1 is coming. The proton side is denoted $-$ and there particle 2 is radiating. When the $+$ -side is interacting with the colour-line connected with the heavy quark it is a t -channel process, and when it interacts with the colour-line associated with the heavy antiquark it is a u channel process.

4.2.1 Projecting the $2 \rightarrow 2$ configuration onto the $2 \rightarrow 3$ configuration

The partonic subprocesses relevant for heavy quarks produced in photoproduction at next-to-leading order ($\mathcal{O}(\alpha_{\text{EM}}\alpha_s)$) are the two body process

$$\gamma g \rightarrow Q\bar{Q} \quad (4.12)$$

and the three-body subprocesses

$$\begin{aligned} \gamma g &\rightarrow Q\bar{Q}g \\ \gamma q &\rightarrow Q\bar{Q}q \end{aligned} \quad (4.13)$$

A Monte Carlo parton shower generates arbitrarily complicated multi-parton configurations starting from the external colour lines of a hard subprocess. After showering, each external parton line in the hard process has become a jet. The parton momenta have to be replaced by the jet momenta in such a way that energy-momentum is conserved, without seriously affecting the dynamics. This process is called momentum reshuffling. This process comes from the Monte Carlo event generator and has to be taken into account when the MC is to be matched with an NLO calculation. In collinear factorization, the partons described by the hard subprocess are on mass-shell initially, but the parton shower may drive them off mass-shell by momentum reshuffling. The momenta of the partons in the hard interaction are changed by the parton shower and the over all kinematics must be adjusted to restore energy-momentum conservation.

The details of the relation between $2 \rightarrow 2$ and $2 \rightarrow 3$ kinematics depends upon the particular form of the momentum reshuffling. In the HERWIG generator, initial and final state radiation is treated differently in the reshuffling, which means that the event

projection is different depending on if the radiation is coming from an incoming or an outgoing parton. Further, there are also two different reshuffling schemes implemented in HERWIG, one which conserves the longitudinal momentum of the $Q\bar{Q}$ pair (the p -scheme), and one that conserves the rapidity of the $Q\bar{Q}$ pair (the y -scheme). Only the incoming momentum fractions x_1 and x_2 are affected by the momentum reshuffling, and therefore it is only important for initial state radiation, since final state radiation does not alter these variables.

The event projection amounts to expressing the $2 \rightarrow 2$ process invariants \bar{s} , \bar{t} and \bar{u} and momentum fractions $\bar{x}_{1,2}$ in terms of the $2 \rightarrow 3$ invariants s , $t_{1,2}$ and $u_{1,2}$ and momentum fractions $x_{1,2}$. In terms of the center of mass variables in eq. (3.43) this means finding $\bar{x}_{1,2}$, \bar{E} and \bar{k}_L . The kinematic variables associated with the invariants in this section are defined in chapter 3.3. In fig. 4.2, some of the notation used throughout this chapter, is shown.

Final State Radiation

If a gluon is emitted from the heavy quark, this gluon ends up in a jet also containing the heavy quark. The final state then consists of this jet and the heavy antiquark. The three-momenta of the heavy antiquark and of the heavy quark jet are then rescaled by momentum reshuffling. In the center of mass frame of the hard process, the heavy antiquark gets the momentum:

$$k_2 = (\sqrt{m^2 + \alpha^2 \bar{k}^2}, -\alpha \bar{k}_T, 0, \alpha \bar{k}_L) \quad (4.14)$$

where $\bar{k}^2 = \bar{k}_T^2 + \bar{k}_L^2 = \bar{E}^2 - m^2$ and α is a rescaling factor given by the energy conservation constraint

$$2\bar{E} = \sqrt{m^2 + (\alpha \bar{k})^2} + \sqrt{(k + k_1)^2 + (\alpha \bar{k})^2}. \quad (4.15)$$

In the case of radiation from the heavy quark, this gives:

$$\begin{aligned} \bar{E} &= \frac{1}{2}\sqrt{s} \\ \bar{k}_L &= \bar{E} \left(\frac{t_2 - u_1}{s - w_1} \right) \frac{\bar{\beta}}{\beta_2}, \end{aligned} \quad (4.16)$$

where β_2 is the velocity of the heavy antiquark in the center of mass frame of the heavy quark-antiquark pair:

$$\beta_2 = \sqrt{1 - \frac{4sm^2}{(s - w_1)^2}} \quad (4.17)$$

For emission from the heavy antiquark, the labels 1 and 2 are interchanged. This means that the relation between $2 \rightarrow 2$ and $2 \rightarrow 3$ invariants depends upon which outgoing leg

is the emitter. Therefore, the $2 \rightarrow 2$ invariants need a label for which outgoing leg is emitting. The relevant relations are then:

$$\begin{aligned}
\bar{s}_Q &= \bar{s}_{\bar{Q}} = s \\
\bar{t}_Q &= -\frac{1}{2}s \left[1 - \left(\frac{t_2 - u_1}{s - w_1} \right) \frac{\bar{\beta}}{\beta_2} \right] \\
\bar{t}_{\bar{Q}} &= -\frac{1}{2}s \left[1 - \left(\frac{t_1 - u_2}{s - w_2} \right) \frac{\bar{\beta}}{\beta_1} \right] \\
\bar{u}_Q &= -s - \bar{t}_Q \\
\bar{u}_{\bar{Q}} &= -s - \bar{t}_{\bar{Q}}
\end{aligned} \tag{4.18}$$

In the soft limit, when $w_{1,2} \rightarrow 0$, $t_{1,2} \rightarrow \bar{t}$ and $u_{1,2} \rightarrow \bar{u}$, there $\bar{t}_{Q,\bar{Q}} \rightarrow \bar{t}$ and $\bar{u}_{Q,\bar{Q}} \rightarrow \bar{u}$ as expected.

The incoming partons are not affected by the final state radiation, so $\bar{p}_1 = p_1$, $\bar{p}_2 = p_2$. Therefore $\bar{s}_{Q,\bar{Q}} = s$ above. Also, the incoming momentum fractions are then unchanged for final state radiation.

Initial State Radiation

In the case of emission from the incoming partons, the invariant mass of the heavy quark pair is unchanged by momentum reshuffling, and since in the $2 \rightarrow 2$ system $\bar{s} = (\bar{p}_1 + \bar{p}_2)^2 = (\bar{k}_1 + \bar{k}_2)^2$:

$$\bar{s} = (k_1 + k_2)^2 = s + v_1 + v_2 \tag{4.19}$$

However, the pair receives longitudinal and transverse boosts. To relate the other variables it is convenient to consider the momentum difference between the heavy quark and antiquark. In the $2 \rightarrow 2$ center of mass frame it is:

$$\bar{k}_1 - \bar{k}_2 = 2(0, \bar{k}_T, 0, \bar{k}_L) \tag{4.20}$$

This does not contain an energy component, and therefore the longitudinal boost is simply rescaling the longitudinal component by the boost factor

$$\gamma_L = \sqrt{1 + \frac{(k_1 + k_2)_L^2}{(k_1 + k_2)^2}} \tag{4.21}$$

The transverse boost does not affect the longitudinal component, meaning

$$(k_1 - k_2)_L = \gamma_L (\bar{k}_1 - \bar{k}_2)_L = 2\gamma_L \bar{k}_L \tag{4.22}$$

The longitudinal components can be extracted with the use of the following combination:

$$\frac{x_2 p_1 - x_1 p_2}{\sqrt{x_1 x_2 s}} = (0, 0, 0, 1) \tag{4.23}$$

Multiplying this quantity with the momentum difference yields:

$$\bar{k}_L = -\frac{(x_2 p_1 - x_1 p_2)(k_1 - k_2)}{2\gamma_L \sqrt{x_1 x_2 s}} \quad (4.24)$$

and

$$\gamma_L = \sqrt{1 + \frac{[(x_2 p_1 - x_1 p_2)(k_1 + k_2)]^2}{x_1 x_2 s (k_1 + k_2)^2}} = \sqrt{1 + \frac{(x_2 p_1 - x_1 p_2)^2}{x_1 x_2 s}} \quad (4.25)$$

Expressing everything in terms of invariants then gives:

$$\begin{aligned} \bar{E} &= \frac{1}{2} \sqrt{s + v_1 + v_2} \\ \bar{k}_L &= \bar{E} \frac{x_2(t_1 - u_1) + x_1(t_2 - u_2)}{2s \sqrt{x_+^2 - \frac{x_1 x_2 v_1 v_2}{s^2}}} \end{aligned} \quad (4.26)$$

where

$$x_{\pm} = \frac{1}{2} \left(\frac{s + v_2}{s} x_1 \pm \frac{s + v_1}{s} x_2 \right) \quad (4.27)$$

These results are independent on which incoming parton is radiating. For consistency, however, the labels $\bar{t} = \bar{t}_+$ or \bar{t}_- depending on if the parton 1 or 2 is radiating. The $2 \rightarrow 2$ invariants expressed in the $2 \rightarrow 3$ invariants are then:

$$\begin{aligned} \bar{s}_{\pm} &= s + v_1 + v_2 \\ \bar{t}_{\pm} &= -\frac{1}{2}(s + v_1 + v_2) \left[1 - \frac{x_2(t_1 - u_1) + x_1(t_2 - u_2)}{2s \sqrt{x_+^2 - \frac{x_1 x_2 v_1 v_2}{s^2}}} \right] \\ \bar{u}_{\pm} &= -\bar{s}_{\pm} - \bar{t}_{\pm} \end{aligned} \quad (4.28)$$

As before, in the soft limit where $v_{1,2} \rightarrow 0$, $t_{1,2} \rightarrow \bar{t}$ and $u_{1,2} \rightarrow \bar{u}$ then $\bar{t}_{\pm} \rightarrow \bar{t}$ and $u_{\pm} \rightarrow \bar{u}$ as expected. In the case of collinear emission from leg 1 where $v_1 \rightarrow 0$, $t_2 \rightarrow \bar{t}$, $u_2 \rightarrow \bar{u}$, $t_1 + w_1 \rightarrow \bar{t}$ and $u_1 + w_2 \rightarrow \bar{u}$, then $\bar{t}_{\pm} \rightarrow \bar{t}$ and $\bar{u}_{\pm} \rightarrow \bar{u}$. The same holds for collinear emission from leg 2.

The momentum fraction carried by the incoming partons are affected by initial state radiation. From the first equation in eq. (4.28) it can be concluded that the sum of the momentum fractions has to be rescaled, thus

$$\bar{x}_{1i} \bar{x}_{2i} = \frac{s + v_1 + v_2}{s} x_1 x_2 \quad (4.29)$$

The values of \bar{x}_{1i} and \bar{x}_{2i} separately depends on the momentum reshuffling scheme.

In the p -scheme, the longitudinal momentum of the heavy quark pair is preserved, which means that

$$\bar{x}_{1i} - \bar{x}_{2i} = \frac{s + v_2}{s} x_1 - \frac{s + v_1}{s} x_2 \quad (4.30)$$

and therefore

$$\begin{aligned} \bar{x}_{1i} &= x_- + \sqrt{x_+^2 - \frac{x_1 x_2 v_1 v_2}{s^2}} \\ \bar{x}_{2i} &= \bar{x}_{1i} - 2x_- \end{aligned} \quad (4.31)$$

In the y -scheme the rapidity of the heavy quark pair is preserved, which implies that

$$\frac{\bar{x}_{1i}}{\bar{x}_{2i}} = \frac{x_1(s + v_2)}{x_2(s + v_1)} \quad (4.32)$$

giving:

$$\begin{aligned} \bar{x}_{1i} &= x_1 \sqrt{\frac{(s + v_1 + v_2)(s + v_2)}{s(s + v_1)}} \\ \bar{x}_{2i} &= x_2 \sqrt{\frac{(s + v_1 + v_2)(s + v_1)}{s(s + v_2)}} \end{aligned} \quad (4.33)$$

Now, all $2 \rightarrow 2$ kinematic variables are expressed in terms of the $2 \rightarrow 3$ ones. The next step is to also express the HERWIG showering variables in the same variables.

4.2.2 HERWIG Showering Variables in the Form of $2 \rightarrow 3$ invariants

Also when HERWIG shower variables are to be related to the $2 \rightarrow 3$ invariants, the momentum reshuffling has to be considered.

Final-state Radiation

For emission of a gluon from the heavy Quark, the HERWIG variables are the angular variable

$$\xi = \frac{k \cdot k_1}{k^0 k_1^0} \quad (4.34)$$

and the energy fraction

$$z = \frac{k_1^0}{E_0} = 1 - \frac{k^0}{E_0} \quad (4.35)$$

where all energies are being evaluated in the showering frame where $E_0^2 = -\bar{t}/2$ or $E_0^2 = -\bar{u}/2$, depending on the colour flow as shown in fig. 4.2. The invariant quantities are the jet virtuality

$$(k_1 + k)^2 - m^2 = w_1 = 2z(1 - z)\xi E_0^2 \quad (4.36)$$

and the '+' momentum fraction of the gluon with respect to the jet axis,

$$\zeta_1 \equiv \frac{k \cdot n_2}{(k_1 + k) \cdot n_2} = (1 - z) \frac{1 + (1 - z\xi)/\tilde{\beta}_1}{1 + \tilde{\beta}_1} \quad (4.37)$$

where $\tilde{\beta}_1$ is heavy-quark jet velocity in the showering frame

$$\tilde{\beta}_1 = \sqrt{1 - \frac{w_1 + m^2}{E_0^2}} \quad (4.38)$$

and n_2 is a light-like vector which goes along the direction of the heavy antiquark in the heavy quark-antiquark center of mass frame:

$$n_2 = k_2 - \frac{s - w_1}{2s}(1 - \beta_2)(p_1 + p_2), \quad (4.39)$$

where β_2 is defined as above in eq. (4.17). Inserting eq. (4.39) into eq. (4.37), gives

$$\zeta_1 = \frac{(s + w_1)w_2 + (s - w_1)[(w_1 + w_2)\beta_2 - w_1]}{(s - w_1)\beta_2[(s + w_1) + (s - w_1)\beta_2]}. \quad (4.40)$$

The variables $z_Q^{(t)}$ and $\xi_Q^{(t)}$, corresponding to the emission from the heavy quark with the t -flow colour structure, can be obtained by solving eqs. (4.36), (4.37) and (4.40) for z and ξ with $E_0^2 = -\bar{t}_Q/2$ as given in eq. (4.18). Similarly, solving with $E_0^2 = -\bar{u}_Q/2$, for the u -colour flow, gives $z_Q^{(u)}$ and $\xi_Q^{(u)}$. The result is

$$\begin{aligned} z_Q^{(l)} &= 1 - \tilde{\beta}_1 \zeta_1 - \frac{w_1}{(1 + \tilde{\beta}_1)|\bar{l}_Q|} \\ \xi_Q^{(l)} &= \frac{w_1}{z_Q^{(l)}(1 - z_Q^{(l)})|\bar{l}_Q|} \end{aligned} \quad (4.41)$$

where $l = t, u$. Interchanging the labels 1 and 2 and using \bar{l}_Q instead of \bar{l}_Q gives $z_Q^{(t,u)}$ and $\xi_Q^{(t,u)}$, corresponding to emissions from the heavy antiquark. Thereby are the HERWIG showering variables expressed in terms of the $2 \rightarrow 3$ invariants for the final state.

The transverse momentum of the emitted gluon, relative to the jet axis is

$$k_T^2 = \zeta_1 [(1 - \zeta_1)w_1 - \zeta_1 m^2]. \quad (4.42)$$

For small values of ξ and m^2/E_0^2 it becomes

$$k_T \simeq \sqrt{2}z(1 - zQ) \quad (4.43)$$

where $Q = E_0\sqrt{\xi}$ is the HERWIG evolution variable.

Initial State Radiation

The case of initial state radiation is somewhat simpler than radiation from the final state, since the jet axis coincides with the beam axis. For emission from parton 1, the jet virtuality is

$$(p_1 - k)^2 = v_1 = -2\frac{1-z}{z^2}\xi E_0^2, \quad (4.44)$$

and the '+' component of the gluon momentum is

$$\frac{k \cdot p_2}{p_1 \cdot p_2} = -\frac{v_2}{s} = \frac{1}{2}(1-z)(2-\xi). \quad (4.45)$$

Solving eqs. (4.44) and (4.45) for z and ξ with $E_0^2 = -\bar{t}_+/2$ or $E_0^2 = -\bar{u}_+/2$ as given in eq. (4.28), the variables $z_+^{(t,u)}$ and $\xi_+^{(t,u)}$ are obtained¹. These variables corresponds to radiation from the incoming parton 1. The solutions are:

$$\begin{aligned} z_+^{(l)} &= \frac{|\bar{l}_+|}{v_1} \left[1 - \sqrt{1 - 2\frac{v_1}{|\bar{l}_+|} \left(1 + \frac{v_2}{s}\right)} \right] \\ \xi_+^{(l)} &= 2 \left[1 + \frac{v_2}{s(1 - z_+^{(l)})} \right] \end{aligned} \quad (4.46)$$

where $\bar{l}_+ = \bar{t}_+, \bar{u}_+$.

For radiation from the incoming parton 2, the variable v_1 and v_2 are interchanged. Then the solution is denoted by $z_-^{(l)}$ and $\xi_-^{(l)}$.

4.2.3 The Monte Carlo Subtraction Terms for $\gamma^*P \rightarrow Q\bar{Q}$

In this section, the cross-section in HERWIG for the first branching, giving a $2 \rightarrow 3$ configuration, will be found. This is what will be subtracted from the real emission part of the NLO calculation, i.e. this is the Monte Carlo subtraction term. Schematically, the first branching in HERWIG may be written in the following way:

$$d\sigma|_{\text{MC}} = d\sigma_{\text{Born}} \otimes d\mathcal{P}(\text{First branching}) \otimes \Theta(\text{Dead regions})\Theta(\text{Dead zones}) \quad (4.47)$$

where $d\sigma_{\text{Born}}$ denotes the total Born cross-section, and $d\mathcal{P}(\text{First branching})$ denotes the probability of the first branching according to the parton shower. For final state radiation in HERWIG it is given by (as in eq. (2.36)):

$$d\mathcal{P}_a(\xi, z) = \frac{\alpha_s}{2\pi} P_{ba}(z) \frac{d\xi}{\xi} dz \quad (4.48)$$

¹In principle, if both incoming partons are gluons, there is also the possibility that $E_0^2 = \bar{s}_+/2$, and the corresponding variables are denoted $z_+^{(s)}$ and $\xi_+^{(s)}$. However, this is never the case in pointlike photoproduction.

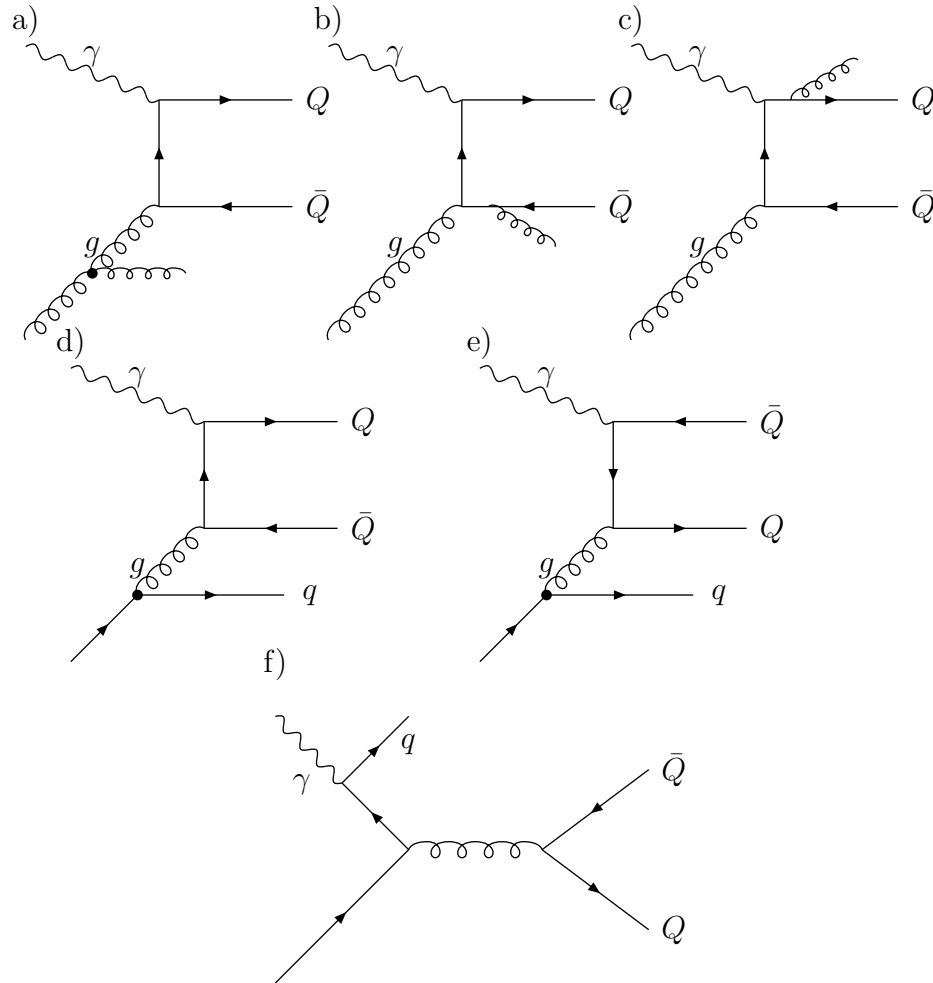


Figure 4.3: Diagrams depicting the non-vanishing contributions in the Monte Carlo subtraction terms. Diagrams a), b) and c) depict the γg initial state, diagrams d) and e) and the γq initial state and diagram f) the $\gamma \bar{q}$ initial state.

for a particular branching $a \rightarrow bc$, and for the initial state it is (as in eq. (2.21)):

$$d\mathcal{P}_a(\xi, z) = \frac{\alpha_s}{2\pi} P_{ac}(z) \frac{f_c(x/z)}{f_a(x)} \frac{d\xi}{\xi} \frac{dz}{z} \quad (4.49)$$

where the parton density functions $f(x)$ come from the backward evolution. The total Born cross-section can be written in the factorized form:

$$d\sigma_{\text{Born}} = f_a(x_1) f_b(x_2) d\hat{\sigma}_{ab}|_{\text{Born}} dx_1 dx_2 \quad (4.50)$$

where $d\hat{\sigma}_{ab}|_{\text{Born}}$ is the partonic cross-section at Born level for incoming partons a and b . The dead regions and dead zones in eq. (4.47) are defined in chapter 2.3.1. Equations (4.47)-(4.50) give the general structure of the Monte Carlo subtraction term. In order to construct the actual MC subtraction term, each possible branching needs to be added and all variables ξ , z and x_i has to be expressed in the invariants of the $2 \rightarrow 3$ configuration found in the previous subsections.

The resulting MC subtraction term $d\sigma|_{\text{MC}}$ is therefore the sums:

$$d\sigma|_{\text{MC}} = \sum_p \sum_L \sum_l d\sigma_{\gamma p}^{(L,l)}|_{\text{MC}}, \quad (4.51)$$

where the first sum p runs over the incoming partons from the proton side. This is either a gluon or a light quark. The index L runs over the emitting legs and assumes the values $+, -, Q$ and \bar{Q} , as shown in fig. 4.2. The index l runs over the colour structures and takes the values t and u .

The terms $d\sigma_{\gamma p}^{(L,l)}|_{\text{MC}}$ may then be written [45]:

$$d\sigma_{\gamma p}^{(+,l)}|_{\text{MC}} = \frac{1}{z_+} f_\gamma^e(\bar{x}_{1i}/z_+^{(l)}) f_p^P(\bar{x}_{2i}) d\hat{\sigma}_{\gamma p}^{(+,l)}|_{\text{MC}} d\bar{x}_{1i} d\bar{x}_{2i}, \quad (4.52)$$

$$d\sigma_{\gamma p}^{(-,l)}|_{\text{MC}} = \frac{1}{z_-} f_\gamma^e(\bar{x}_{1i}) f_p^P(\bar{x}_{2i}/z_-^{(l)}) d\hat{\sigma}_{\gamma p}^{(-,l)}|_{\text{MC}} d\bar{x}_{1i} d\bar{x}_{2i}, \quad (4.53)$$

$$d\sigma_{\gamma p}^{(Q,l)}|_{\text{MC}} = f_\gamma^e(\bar{x}_{1f}) f_p^P(\bar{x}_{2f}) d\hat{\sigma}_{\gamma p}^{(Q,l)}|_{\text{MC}} d\bar{x}_{1f} d\bar{x}_{2f}, \quad (4.54)$$

$$d\sigma_{\gamma p}^{(\bar{Q},l)}|_{\text{MC}} = f_\gamma^e(\bar{x}_{lf}) f_p^P(\bar{x}_{2f}) d\hat{\sigma}_{\gamma p}^{(\bar{Q},l)}|_{\text{MC}} d\bar{x}_{lf} d\bar{x}_{2f}, \quad (4.55)$$

The functions $f_\gamma^e(\bar{x})$ is the photon flux coming from the electron and $f_p^P(x)$ is the PDF for parton p in the proton. Here, $d\hat{\sigma}_{\gamma p}^{(L,l)}|_{\text{MC}}$ denotes the branching probabilities in equations (4.48) and (4.49), *not* including the PDFs in the initial state radiation. All variables in eq. (4.55) are defined in terms of the $2 \rightarrow 3$ invariants.

| ab | $\gamma g \rightarrow Q\bar{Q}$ | $\gamma q \rightarrow Q\bar{Q}$ | $\gamma\bar{q} \rightarrow Q\bar{Q}$ |
|------------|---------------------------------|---------------------------------|--------------------------------------|
| γg | $-(t), -(u), Q(u), \bar{Q}(t)$ | $-(t), -(u)$ | $-(t), -(u)$ |
| $q\bar{q}$ | | | $+(t)$ |

Table 4.1: Short-distance contributions to MC subtraction terms, from Born processes $\gamma g \rightarrow Q\bar{Q}$, $\gamma q \rightarrow Q\bar{Q}$ and $\gamma\bar{q} \rightarrow Q\bar{Q}$. Each entry lists the emitting legs (+, -, Q , \bar{Q}). For each emitting leg, the information about the contributions l , according to the possible colour flows (corresponding to $E_0^2 = |\bar{l}|/2$) is given in parentheses.

The parton shower branchings contributing to $d\hat{\sigma}_{\gamma p}^{(L,l)}|_{\text{MC}}$ are shown in fig. 4.3 and listed in table 4.1. These give,

1. for γg initial state, shown in figs. 4.3 a), b) and c):

$$d\hat{\sigma}_{\gamma g}^{(-,t)}|_{\text{MC}} = \frac{\alpha_s}{4\pi} \frac{d\xi_-^{(t)}}{\xi_-^{(t)}} dz_-^{(t)} P_{gg}(z_-^{(t)}) d\hat{\sigma}_{\gamma g}^{(t)}|_{\text{Born}} \Theta\left((z_-^{(t)})^2 - \xi_-^{(t)}\right) \quad (4.56)$$

$$d\hat{\sigma}_{\gamma g}^{(Q,u)}|_{\text{MC}} = \frac{\alpha_s}{2\pi} \frac{d\xi_Q^{(u)}}{\xi_Q^{(u)}} dz_Q^{(u)} P_{qq}(z_Q^{(u)}) d\hat{\sigma}_{\gamma g}^{(u)}|_{\text{Born}} \Theta\left(1 - \xi_Q^{(u)}\right) \Theta\left((z_Q^{(u)})^2 - \frac{2m^2}{|\bar{u}_Q|\xi_Q^{(u)}}\right)$$

$$d\hat{\sigma}_{\gamma g}^{(\bar{Q},t)}|_{\text{MC}} = \frac{\alpha_s}{2\pi} \frac{d\xi_{\bar{Q}}^{(t)}}{\xi_{\bar{Q}}^{(t)}} dz_{\bar{Q}}^{(t)} P_{gg}(z_{\bar{Q}}^{(t)}) d\hat{\sigma}_{\gamma g}^{(t)}|_{\text{Born}} \Theta\left(1 - \xi_{\bar{Q}}^{(t)}\right) \Theta\left((z_{\bar{Q}}^{(t)})^2 - \frac{2m^2}{|\bar{t}_{\bar{Q}}|\xi_{\bar{Q}}^{(t)}}\right),$$

2. for γq initial state, shown in fig. 4.3 d) and e):

$$d\hat{\sigma}_{\gamma q}^{(-,t)}|_{\text{MC}} = \frac{\alpha_s}{4\pi} \frac{d\xi_-^{(t)}}{\xi_-^{(t)}} dz_-^{(t)} P_{gq}(z_-^{(t)}) d\hat{\sigma}_{\gamma q}^{(t)}|_{\text{Born}} \Theta\left((z_-^{(t)})^2 - \xi_-^{(t)}\right) \quad (4.57)$$

$$d\hat{\sigma}_{\gamma q}^{(-,u)}|_{\text{MC}} = \frac{\alpha_s}{4\pi} \frac{d\xi_-^{(u)}}{\xi_-^{(u)}} dz_-^{(u)} P_{gq}(z_-^{(u)}) d\hat{\sigma}_{\gamma q}^{(u)}|_{\text{Born}} \Theta\left((z_-^{(u)})^2 - \xi_-^{(u)}\right),$$

3. and for $\gamma\bar{q}$ initial state, depicted in fig. 4.3 f):

$$d\hat{\sigma}_{\gamma\bar{q}}^{(+,t)}|_{\text{MC}} = \frac{\alpha_s}{2\pi} \frac{d\xi_+^{(t)}}{\xi_+^{(t)}} dz_+^{(t)} P_{\gamma\rightarrow q\bar{q}}(z_+^{(t)}) d\hat{\sigma}_{q\bar{q}}^{(t)}|_{\text{Born}} \Theta\left((z_+^{(t)})^2 - \xi_+^{(t)}\right). \quad (4.58)$$

The colour indices t and u are defined in fig. 4.4. If the emitting parton is a gluon, it is colour connected to both the heavy quark and antiquark and the result is then a superposition of equal parts t and u flow, which gives the extra factor 1/2 in those terms. Here $P_{\gamma\rightarrow q\bar{q}}$ denotes the splitting probability of a photon into a quark-antiquark pair.

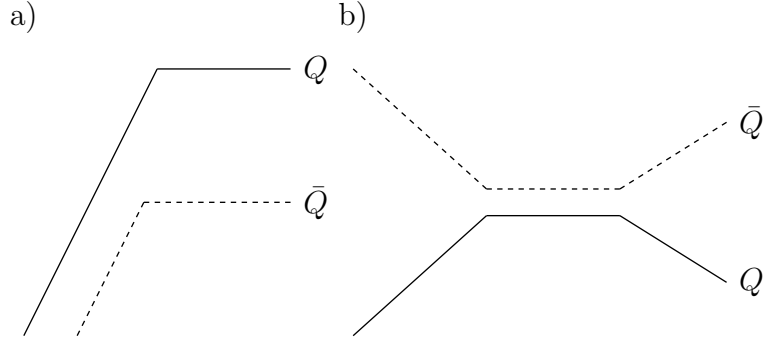


Figure 4.4: a) A diagram depicting the colour flow in the diagrams a) through e) in figure 4.3. In the large N_C limit the two colourlines representing the gluon are connected to the heavy quark and antiquark respectively. b) A diagram depicting the colourflow in diagram f) in fig. 4.3. The t colour flow is defined as emissions from the full line connecting the gluon with the heavy quark, and a u flow is defined as an emission from the dashed colour line.

4.2.4 Local Cancellation of IR Singularities

The subtraction terms given above makes sure that no configurations get doubly counted when the HERWIG parton shower is attached to the NLO matrix element. However, the MC subtraction term also has to act as a local counter term, canceling all soft and collinear singularities in the real emission integral. As is shown in section A.5 of reference [40], this is not the case in the limit of soft gluon emissions. To remedy this, the MC subtraction term is modified in the following way:

$$d\sigma|_{\text{MC}} \rightarrow \mathcal{G}(x)d\sigma|_{\text{MC}} + (1 - \mathcal{G}(x)) \mathcal{M}_{\gamma g}^{(\text{soft})} \quad (4.59)$$

where $\mathcal{M}_{\gamma g}^{(\text{soft})}$ denotes the real matrix element in the soft limit, which is only present for the γg process. Here $\mathcal{G}(x)$ is a function that controls the transition between the subtraction of the parton shower branching and the soft part of the real matrix element. This function must smoothly approach zero in the soft limit:

$$\lim_{x \rightarrow 1} \mathcal{G}(x) = 0 \quad (4.60)$$

where $1 - x$ is the energy fraction taken by the gluon in the splitting. The function $\mathcal{G}(x)$ is then parametrized in such a way that no IR safe observable in the Monte Carlo is affected by it.

To test that the MC subtraction terms cancel the IR singularities in the real part of the matrix element, the ratio

$$R(x, y) = \frac{\mathcal{G}(x)d\sigma|_{\text{MC}} + (1 - \mathcal{G}(x)) \mathcal{M}_{\gamma g}^{(\text{soft})}}{\mathcal{M}_{\gamma p}^{(\text{real})}(x, y)}, \quad (4.61)$$

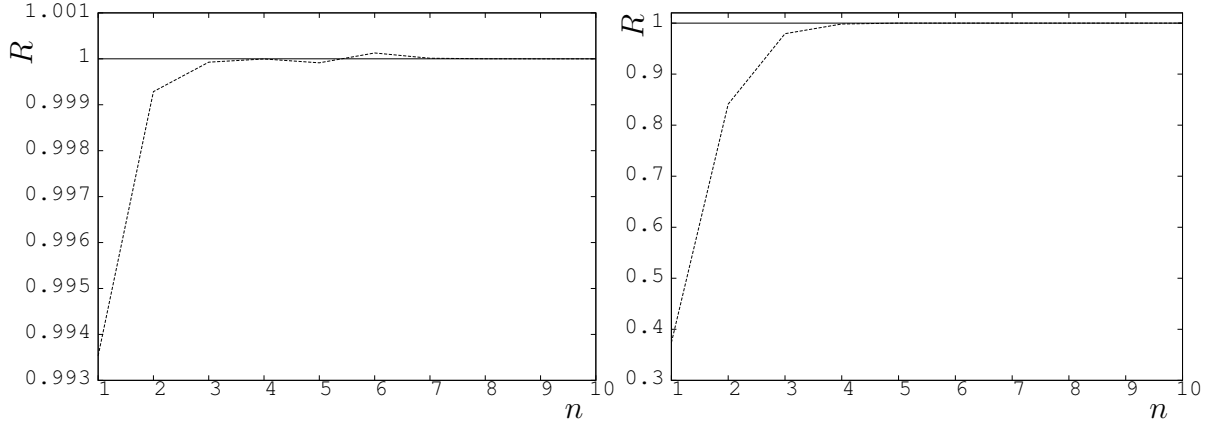


Figure 4.5: The MC subtraction terms approaching the soft (left) and collinear (right) limits for the γg -processes.

is defined. Here $\mathcal{M}_{\gamma p}^{(\text{real})}$ denotes the real part of the matrix element. As was described in chapter 3.3.1, the soft pole is at $x = 1$ and the collinear poles are at $y = \pm 1$. To test the behaviour of $R(x, y)$ close to the poles, it is taken at different values of x_n and y_n according to:

$$\begin{aligned} x_n &= 1 - 10^{-n} \\ y_n^{(-)} &= -1 + 10^{-n} \\ y_n^{(+)} &= 1 - 10^{-(n)} \end{aligned} \quad (4.62)$$

where n is an integer.

In fig. 4.5 the ratio $R(x_n, y_n)$ is plotted as a function of n for the γg processes with a heavy quark mass of 5 GeV. It is plotted for the soft limits present in figs. 4.3 a), b) and c) to the left and for the collinear limits present in fig. 4.3 a) to the right. There it is seen that the MC subtraction terms is smoothly approaching the matrix element in these limits.

In fig. 4.6 the ratio R is plotted for the γq processes, for the collinear limits present in figs. 4.3 d) and e) to the left and the one in fig. 4.3 f) to the right. There it is also seen that the MC subtraction terms is smoothly approaching the matrix element in these limits.

4.3 Generating MC@NLO Events

The MC@NLO cross-section, before the parton shower, may be written on the form

$$\sigma_{\text{NLO}}^{\text{msub}} = I_{\text{R}} + I_{\text{BV}} = \int_3 \mathcal{R}_{\text{msub}}(\phi_3) d\phi_3 + \int_2 (\mathcal{V}_{\text{msub}}(\phi_2) + \mathcal{B}(\phi_2)) d\phi_2 \quad (4.63)$$

In order to generate Monte Carlo events according to this, the two types of events, in the two integrals, has to be generated separately. This is done in a similar way as for the

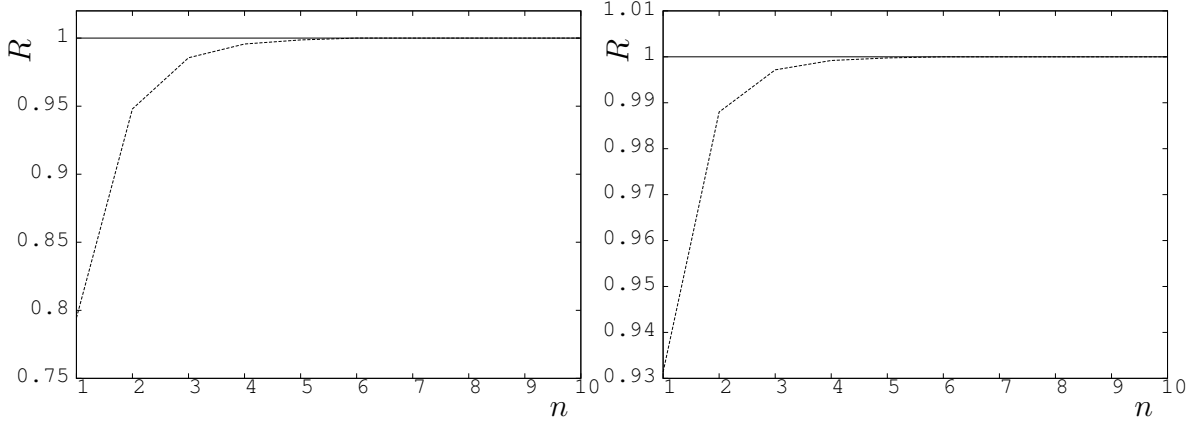


Figure 4.6: The MC subtraction terms approaching the collinear limits for the $\gamma q/\bar{q}$ -processes. On the left for radiation collinear to the proton and on the right to the photon.

NLO-calculation, which was explained in chapter 3.4. This will produce configurations $\phi_3^{(i)}$ with weights $\mathcal{R}_i(\phi_3^{(i)})$ and $\phi_2^{(j)}$ with weights $\mathcal{V}_i(\phi_2^{(j)}) + \mathcal{B}_i(\phi_2^{(j)})$. Some of these weights are negative. In order to feed these weighted configurations into the Monte Carlo event generator, they have to be unweighted. To do this, the integrals

$$J_R = \int_3 |\mathcal{R}_{\text{msub}}(\phi_3)| d\phi_3 \quad (4.64)$$

$$J_{\text{BV}} = \int_2 |\mathcal{V}_{\text{msub}}(\phi_2) + \mathcal{B}(\phi_2)| d\phi_2$$

are also computed. Then, if one wants to generate N_{tot} events, a number N_R of these will be generated from the distribution $\mathcal{R}(\phi_3)$ and a number N_{BV} from the distribution $\mathcal{V}_i(\phi_2^{(j)}) + \mathcal{B}_i(\phi_2^{(j)})$. These numbers are given by:

$$N_R = N_{\text{tot}} \frac{J_R}{J_{\text{BV}} + J_R} \quad (4.65)$$

$$N_{\text{BV}} = N_{\text{tot}} \frac{J_{\text{BV}}}{J_{\text{BV}} + J_R}$$

This results in N_{tot} events distributed according to eq. (4.63). The sign of the weight for each configuration are kept track of, such that some of the resulting events will have a weight of -1 . These events are then written onto a file, which is used as input by the Monte Carlo event generator.

A complication to this procedure is emerging for those diagrams in the calculation where one of the incoming partons is a light quark. In order to chose the flavour of the light quark, the evaluation of the integrals are repeated for all possible flavours. The flavour of the light quark is then selected for each event by its relative contribution to the cross-section.

4.4 Other Matching Schemes of NLO-Matrix Element and Parton Showers

There are other methods than the one presented here to combine a matrix element at NLO with a parton shower. Two such methods are the POWHEG method and the CKKW(-L) method.

In the POWHEG method (Positive Weight Hardest Emission Generator)[46, 47], the matching with the parton shower is performed by expressing the real emission probability in the NLO matrix element with a Sudakov formfactor. The probability is then on the form of a Born cross-section times a Sudakov form factor. The NLO matrix element can be written:

$$\begin{aligned} d\sigma &= B(p_1, \dots, p_m) d\phi_m + V(p_1, \dots, p_m) d\phi_m \\ &+ \left(R(p_1, \dots, p_{m+1}) d\phi_{m+1} - \sum_i C_i(p_1, \dots, p_{m+1}) d\phi_{m+1} \mathcal{P}_i \right) \end{aligned} \quad (4.66)$$

where the Born and Virtual terms generate m final state partons, and the real emissions generate $m + 1$ partons, weighted with R and with counter terms C_i . \mathcal{P}_i is a projection of the $m + 1$ parton phase-space onto the m parton one. The counter terms works as subtraction terms with the projection in a similar way as in eqs. (3.22), (3.23) and (3.76). Assume that the Born state is described by variables $(v) = (v_1, \dots, v_l)$, and that the final state with a real emission is described by $(v, r) = (v_1, \dots, v_l, r_1, r_2, r_3)$ where the variables r_i are associated with the radiated parton. If one assumes that the projection of the phase-space is $d\phi_{m+1} \rightarrow d\phi_v d\phi_r$, where $d\phi_v$ is the Born phase-space and $d\phi_r$ is the product $\prod_i dr_i$ of r_i . The NLO cross-section may then be rewritten as:

$$\begin{aligned} d\sigma &= B(v) d\phi_v + V(v) d\phi_v + (R(v, r) d\phi_v d\phi_r - C(v, r) d\phi_v d\phi_r \mathcal{P}) \\ &= (V(v) + (R(v, r) - C(v, r)) d\phi_r \mathcal{P}) + B(v) d\phi_v \left(1 + \frac{R(v, r)}{B(v)} (1 - \mathcal{P}) d\phi_r \right) \end{aligned} \quad (4.67)$$

Defining the Sudakov formfactor:

$$\Delta_R^{(\text{NLO})}(p_\perp) \equiv \exp \left(- \int d\phi_r \frac{R(v, r)}{B(v)} \theta(k_\perp(v, r) - p_\perp) \right) \quad (4.68)$$

and the ‘‘Born’’ term:

$$\bar{B}(v) \equiv B(v) + V(v) + \int (R(v, r) - C(v, r)) d\phi_r \quad (4.69)$$

the probability of the first (hardest) emission can be written as:

$$d\sigma = \bar{B}(v) d\phi_v \left(\Delta_R^{(\text{NLO})}(0) + \Delta_R^{(\text{NLO})}(p_\perp) \frac{R(v, r)}{B(v)} d\phi_r \right) \quad (4.70)$$

4.4 Other Matching Schemes of NLO-Matrix Element and Parton Showers 89

expanding the Sudakov here to first order in the coupling (or in R) gives the exact NLO prediction. One can interpret this as first is a Born configuration generated according to $\bar{B}(v)$, and then the first emission is generated according to the Sudakov formfactor. The subsequent emissions may then be generated by a parton shower where all other emissions are softer than the first one. This is the case either in a p_\perp ordered parton shower, like the one in PYTHIA, or in a shower with a p_\perp veto on the first emission, which is implemented e.g. in HERWIG. This method is guaranteed to only give events with positive weight (as long as the Born term is larger than the absolute value of the virtual contribution).

In the CKKW or CKKW-L methods [48, 49], tree-level matrix elements are matched with the parton shower by expanding the Sudakov formfactor of the parton shower in orders of α_s . The principle is that one has a matrix element generator which generates a Born-level process with n extra final state partons (jets) according to the exact tree-level matrix element. Onto these configurations is then the parton shower added. The main difference between the matrix element generator and the parton shower, is that the former produces inclusive states at a fixed value of α_s , while the latter produces exclusive states with a running α_s . The matrix element is regulated with a cut-off scale ρ_{MS} , at which the merging with the parton shower takes place. To get a consistent matching at this scale, the matrix element configurations are analyzed as if they were produced by the parton shower with a running coupling, and are then reweighted with Sudakov form factors with the running α_s . In principle, the same procedure may be used for matching with matrix elements at any order in the coupling. To do this, both α_s and the Sudakov form factors has to be expanded in the coupling, in order for the reweighting of the scales to be performed. This method has been implemented with the ARIADNE parton shower for electron-positron scattering.

Chapter 5

Phenomenological Comparisons at Parton-level

In this chapter, some parton level results will be shown from the new MC@NLO program presented in chapter 4. This MC@NLO simulates heavy quarks produced in photoproduction. It will be compared to the fixed order next-to-leading (NLO) calculation, described in chapter 3, and the leading-order calculation (LO). These calculations are implemented in the FMNR program [42]. Comparisons will also be made to the HERWIG [15] event generator, described in chapter 2, which contains a LO matrix element calculation supplemented with parton showers radiating to all orders. MC@NLO is the NLO-calculation matched with the HERWIG parton shower.

There are mainly two reasons to describe perturbative QCD at higher orders. Firstly, the hard parton dynamics are expected to be better described at higher orders, which will be shown in section 5.1. At LO, only the two outgoing heavy quarks will be present in the final state. By momentum conservation they will always be back-to-back in the transverse plane. At NLO, there may also be a third particle present in the final state, a light quark or a gluon. Also, in a Monte Carlo, the parton shower gives rise to a multi-parton final state. The impact of events with negative weights in MC@NLO will be investigated in section 5.1.1. When calculating the matrix element at NLO, the dependency on quark distributions within the photon is smaller. This will be investigated in section 5.1.2.

Secondly, when calculating the matrix element at higher orders, the dependencies on non-physical scales in the strong coupling and in the parton density functions are expected to be smaller. This is a statement from perturbative QCD, that when the scale is large enough, the next term in the perturbative expansion should be smaller than the previous one. How this works for beauty and charm production at parton level will be shown in section 5.2.

The parameter settings used in all distributions in this chapter is summarized in table 5.1.

| | |
|-------------|--|
| m_b | 4.75 GeV |
| m_c | 1.5 GeV |
| Fact. Scale | $\frac{1}{2}(m_{\perp}(Q) + m_{\perp}(Q))$ |
| Ren. Scale | $m_{\perp}(Q) + m_{\perp}(Q)$ |
| Proton PDF | Cteq6.6 |
| Photon PDF | GRV |

Table 5.1: Parameter settings used for the partonic cross-sections.

| MC@NLO | Pointlike | Hadronic | Total |
|-------------|-----------|-----------|-----------|
| Beauty [pb] | 4931±8 | 1507±2 | 6438±8 |
| Charm [nb] | 634.3±0.7 | 176.5±0.4 | 810.8±0.8 |
| FMNR | | | |
| Beauty | 4930±2 | 1505± 2 | 6435±3 |
| Charm | 633.4±0.4 | 176.2±0.4 | 809.6±0.6 |
| HERWIG | | | |
| Beauty | 3634±2 | 1456.±0.7 | 5090±2 |
| Charm | 474.8±0.2 | 246.8±0.1 | 721.6±0.2 |
| LO | | | |
| Beauty | 3622±0.04 | - | - |
| Charm | 548.8±0.1 | - | - |

Table 5.2: Total Cross-sections for MC@NLO, FMNR and HERWIG and the Born cross-section (LO). The difference in the latter two comes from different definitions of α_s , where HERWIG is using two loop α_s and LO is using one loop.

5.1 Parton Dynamics

When looking at parton dynamics resulting from different types of calculations, it is interesting to look both at the behaviour of individual particles as well as at the correlated behaviour of two partons.

For the first category, plots of transverse momentum and pseudo rapidity of the produced heavy quarks are shown in figs. 5.1 and 5.2, for beauty and charm production respectively. The pseudo-rapidity is defined as:

$$\eta = -\ln \left[\tan \left(\frac{\theta}{2} \right) \right], \quad (5.1)$$

where θ is the particle's angle relative to the proton beam-axis. Here, the interval $-1 < \eta < 1$ is called the central region, $\eta > 1$ is called the forward region, and $\eta < -1$ is called the backwards region. The proton remnant end up in the very forward region

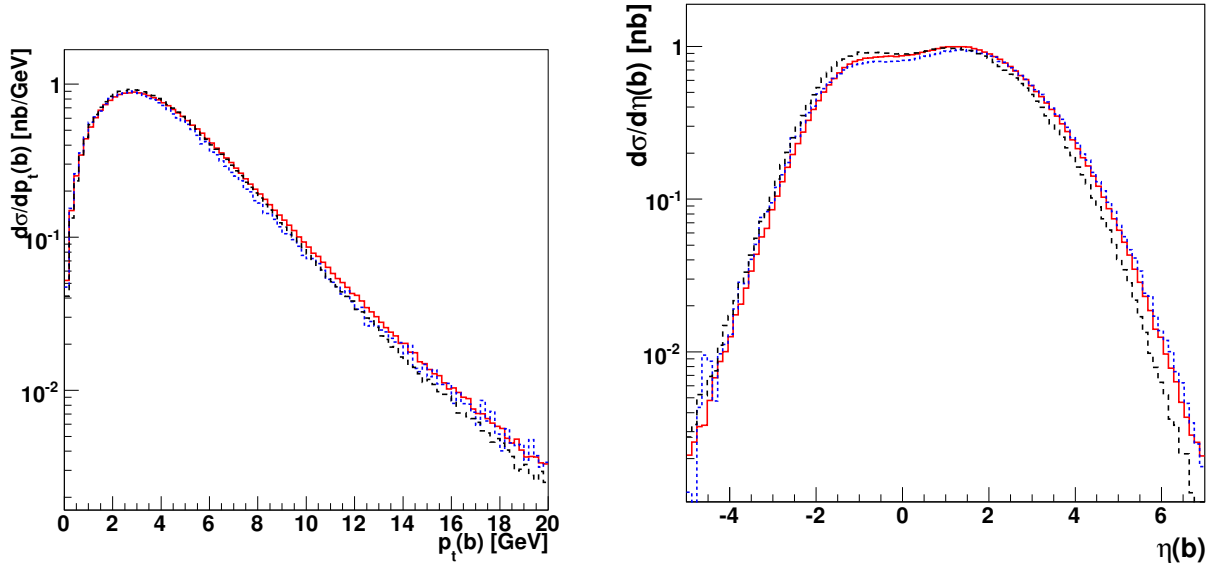


Figure 5.1: The spectra of the transverse momentum and the rapidity of the produced b-quarks in MC@NLO, in FMNR (NLO) and in HERWIG (MC).

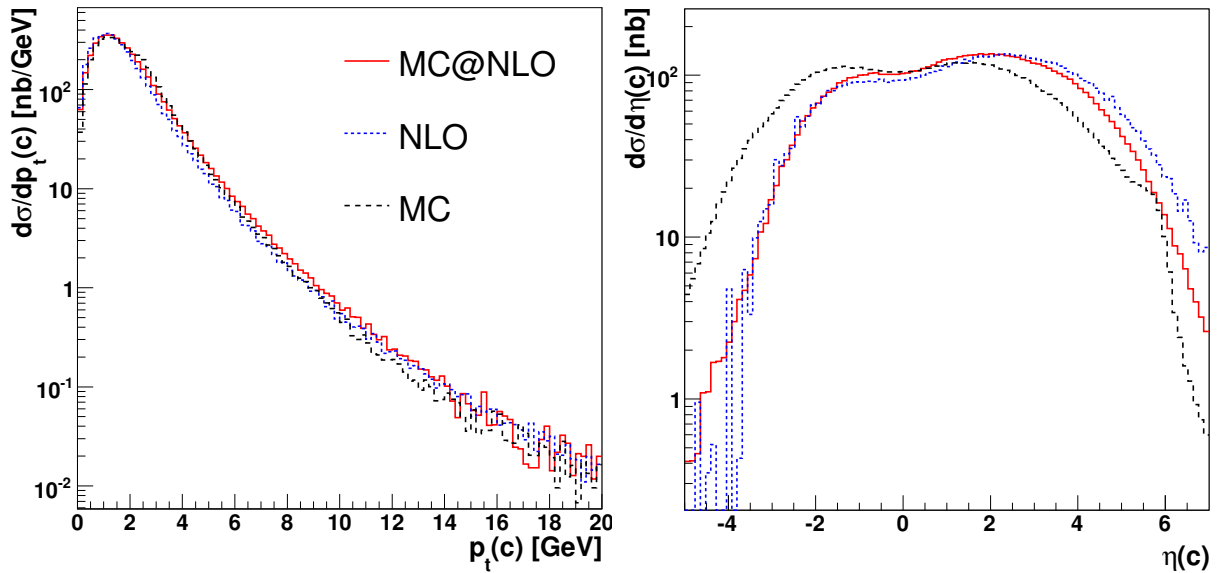


Figure 5.2: The spectra of the transverse momentum and the rapidity of the produced c-quarks in MC@NLO, in FMNR (NLO) and in HERWIG (MC).

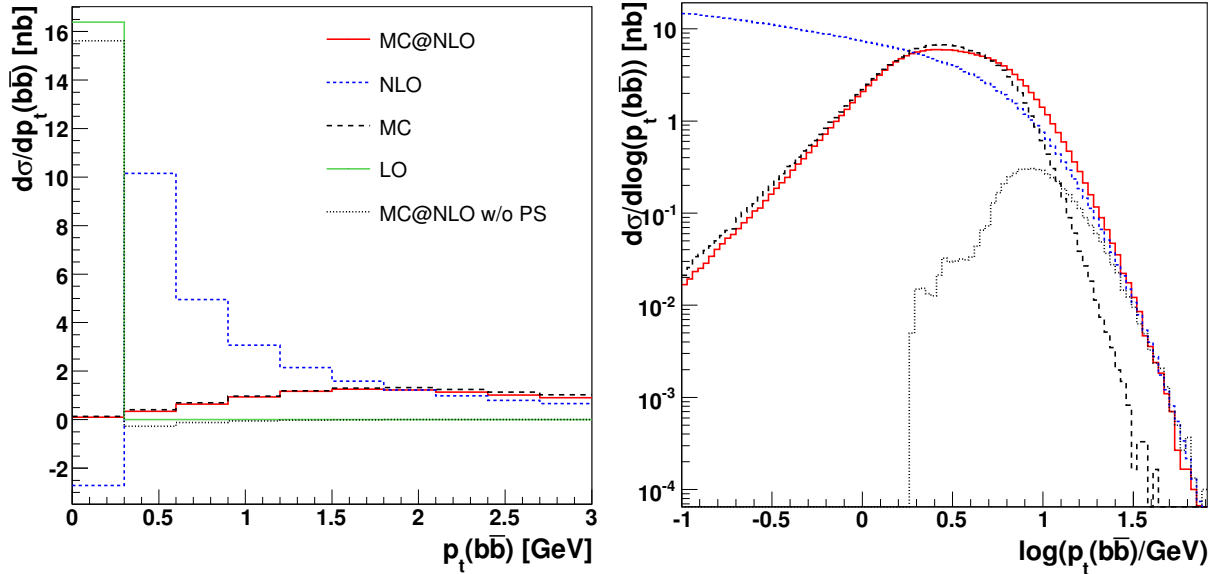


Figure 5.3: The p_{\perp} -distribution of the $b\bar{b}$ -pair.

while the scattered electron ends up in the very backwards region. In figs. 5.1 and 5.2 the p_{\perp} distributions of the heavy quarks are similar in all three programs. The η distribution of the b-quarks is also similar, HERWIG has a slightly larger cross-section in the backwards region and a slightly smaller one in the forward region. For charm production this difference is more pronounced.

One observable of correlations between partons is the combined transverse momentum of the heavy quarks. Conservation of transverse momentum means that the transverse momentum of the heavy quark-antiquark system must be balanced by higher order radiations. For leading order such radiations are not present, the heavy quark and its antiquark are back-to-back and their combined p_{\perp} is always zero. At next-to-leading order sometimes a light parton is also radiated (in the real emission part), which has a $p_{\perp} > 0$. However, at $p_{\perp}(Q\bar{Q}) = 0$ no real emission is possible. Here the virtual contributions will dominate, resulting in a negative cross-section for $p_{\perp}(Q\bar{Q}) = 0$, which is seen on the left hand side of fig. 5.3. When the LO matrix element is supplemented by a parton shower radiating partons to all orders, the p_{\perp} of the $Q\bar{Q}$ system is balanced by this radiation. The parton shower is however ordered in p_{\perp} such that radiation harder than the heavy quark mass are suppressed, something which is not the case for the real emission by the NLO calculation which is only limited by the total available energy. However, while the NLO-calculation is rising steeply for smaller $p_{\perp}(Q\bar{Q})$, the all loop resummation in the Sudakov formfactor in the parton shower produces a turnover in the p_{\perp} -spectrum. The same turnover is expected by MC@NLO, since it also produces higher order radiation with the same parton shower as the Monte Carlo, but it is also expected to be able to produce radiations by the real emissions in the matrix element which fills out the full phase space. This can be seen in the right hand side plot of figure 5.3 for beauty production and in

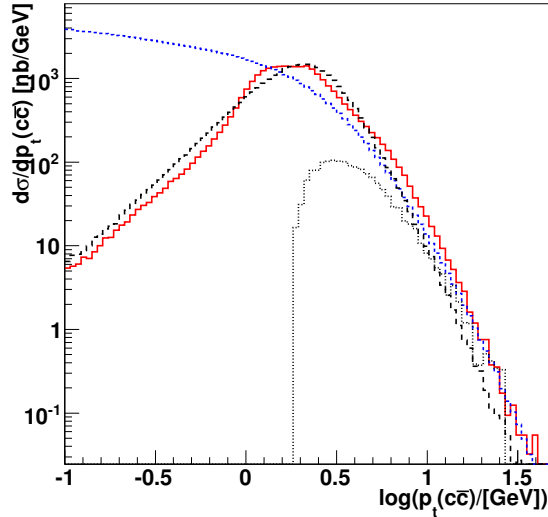


Figure 5.4: The p_{\perp} -distribution of the $c\bar{c}$ -pair.

fig. 5.4 for charm production. Here also the $p_{\perp}(Q\bar{Q})$ spectrum of the subtracted NLO matrix element in MC@NLO is shown, before the parton showers is added. It can be seen that it fills out exactly the parts of phase-space where the LO MC does not. The difference in the distributions from NLO and MC@NLO, before the parton shower, demonstrates the difference between NLO subtraction and modified subtraction, since $p_{\perp}(Q\bar{Q})$ clearly depend strongly on the parton shower.

Another observable of interest for higher order radiation is the azimuthal angle between the heavy quark and the hardest other parton, which is shown in fig. 5.5. Again, in leading order there are only two partons in the final state: the heavy quark and its antiquark, and they are always back-to-back, i.e. at $\Delta\phi = 180^\circ$. For the NLO calculation other angles are possible when a light particle is radiated. It is however not kinematically allowed for $\Delta\phi$ to be smaller than 90° in the three-particle scenario. If the angle between two of the partons is less 90° the third parton must be harder than one of the other two. Therefore, even at NLO no radiation is allowed such that $\Delta\phi < 90^\circ$. With a parton shower many more than three particles can be produced in the final state such that the hardest other parton may be at any azimuthal angle relative to the heavy quark.

5.1.1 Influence of Events with Negative Weights

One big difference between MC@NLO and conventional Monte Carlo event generators, is that in the former, some events have a negative weight -1 . This is explained in chapter 4.3. The presence of negative weights has an impact on the relative statistical error within

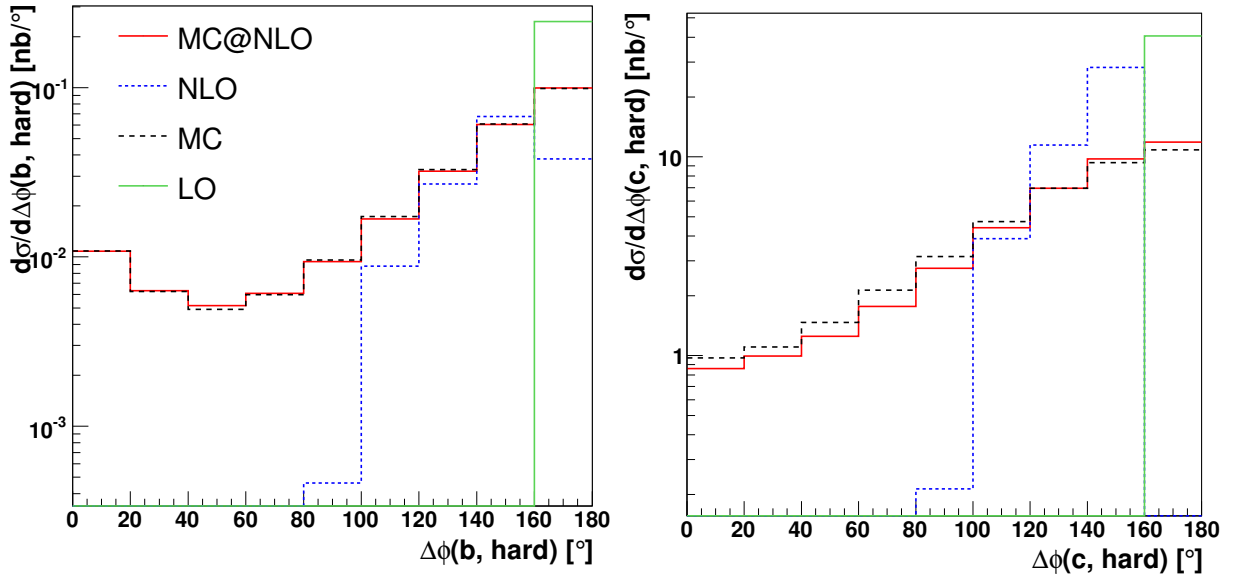


Figure 5.5: The distribution in difference in azimuthal angle between the produced heavy quark and the hardest other parton. For beauty production in the left plot and for charm production in the right.

| MC@NLO | Negative events [%] |
|--------|---------------------|
| Beauty | 25.3 |
| Charm | 36.5 |

Table 5.3: The fraction of events with negative weight in MC@NLO for Beauty and Charm production respectively.

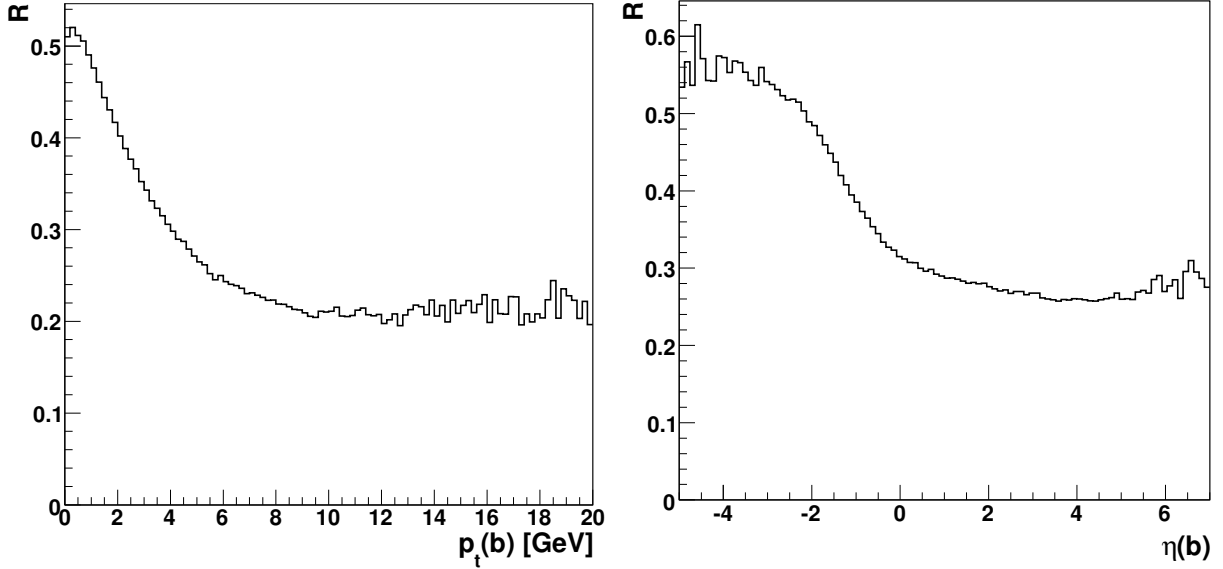


Figure 5.6: The MC@NLO distributions of events with negative weights divided by the distributions of events with positive weights as functions of p_{\perp} and η of the produced beauty quarks.

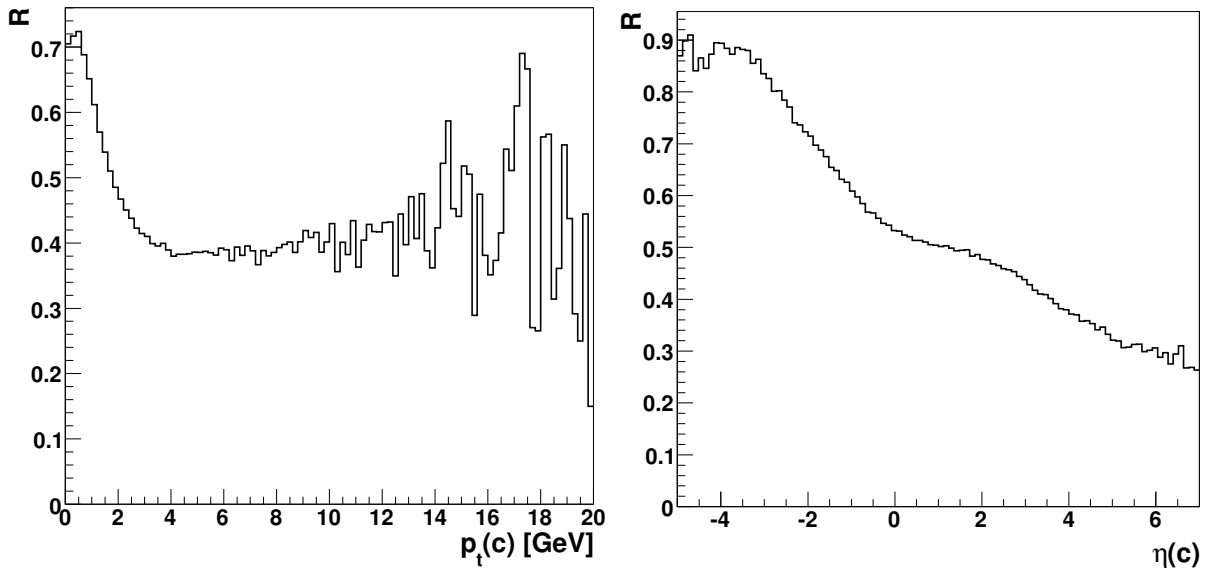


Figure 5.7: The MC@NLO distributions of events with negative weights divided by the distributions of events with positive weights as functions of p_{\perp} and η of the produced charm quarks.

a given histogram bin. It is:

$$\text{Relative Statistical Error} = \frac{\sqrt{N_+ + N_-}}{N_+ - N_-} \quad (5.2)$$

where N_+ and N_- are the numbers of entries with positive and negative weights respectively. If for example $N_- = 0.9N_+$ in a given bin, the relative error in the bin become $\sim 14/\sqrt{N_+} \simeq 13/\sqrt{N}$, with $N = N_+ - N_-$ being the total number of entries in the bin. This relative error is thus more than 10 times larger than it would be with all weights positive.

In table 5.3 the total fraction of negative events for different MC@NLO calculations are listed. In fig. 5.6 the p_\perp and η distributions of events with negative weights are divided with the distributions with positive weights for beauty production. In other words, the distribution in the ratio R , defined as:

$$R = \left| \frac{\frac{d\sigma}{dp_\perp}(b) \Big|_{\text{positive weight}}}{\frac{d\sigma}{dp_\perp}(b) \Big|_{\text{negative weight}}} \right| \quad (5.3)$$

for the p_\perp distribution and similarly for the distribution in η . Here, one can see that the negative weights are around 50% for small $p_\perp(b)$ but their fraction is then decreasing to about 20% for larger $p_\perp(b)$. In the distribution of $\eta(b)$ the negative events are most important in the backwards region $\eta(b) \simeq -4$ where they lie around 55%, whereas in the forward region $\eta(b) > 0$ they are around 30% of the positive events.

In fig. 5.7 the same distributions are shown for charm production. Here, the shapes are similar to that for beauty production but the fraction of negative to positive events is as large as 90% in the very backwards region where $\eta(c) \simeq -4$. This means that in this region the resulting cross-section is much smaller than the separate distributions of positive and negative events, which could lead to precision problems if one does not use enough events.

5.1.2 Influence of the Photon

When calculating the matrix element at NLO, the dependency on quark distributions within the photon is smaller. The so-called quark excitations are namely included in the point-like calculation of the NLO matrix element, while they are included in the resolved part of the LO matrix element calculation. These notations are illustrated in fig. 5.8 and explained in the caption. Since the perturbative part of the resolved photon is included in the part with the pointlike photon in the NLO-calculation, it will be less dependent on the photon structure than the LO calculations. The photon PDFs are in general not very well known.

As can be seen in table 5.2, the contribution by the hadronic part of the calculation to the total cross-section in MC@NLO is $\sim 23\%$ and $\sim 22\%$ for beauty and charm production

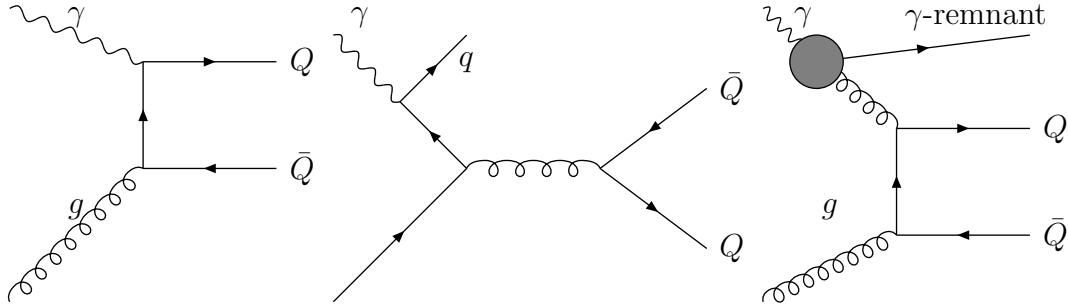


Figure 5.8: An illustration of the different components of the calculations. To the left is the photon directly interacting with the gluon, in the middle, it is split into a $q\bar{q}$ pair before the interaction and to the right, it is becoming a hadron, from which a parton may interact with the gluon coming from the proton. The left diagram is called “direct”, the left and the middle diagrams are together called “point-like”, the middle and the right diagrams are together called “resolved” and the right diagram by itself is called “hadronic”. In LO calculations, the direct and resolved parts are calculated separately, while in NLO calculations, the pointlike and hadronic parts are calculated separately.

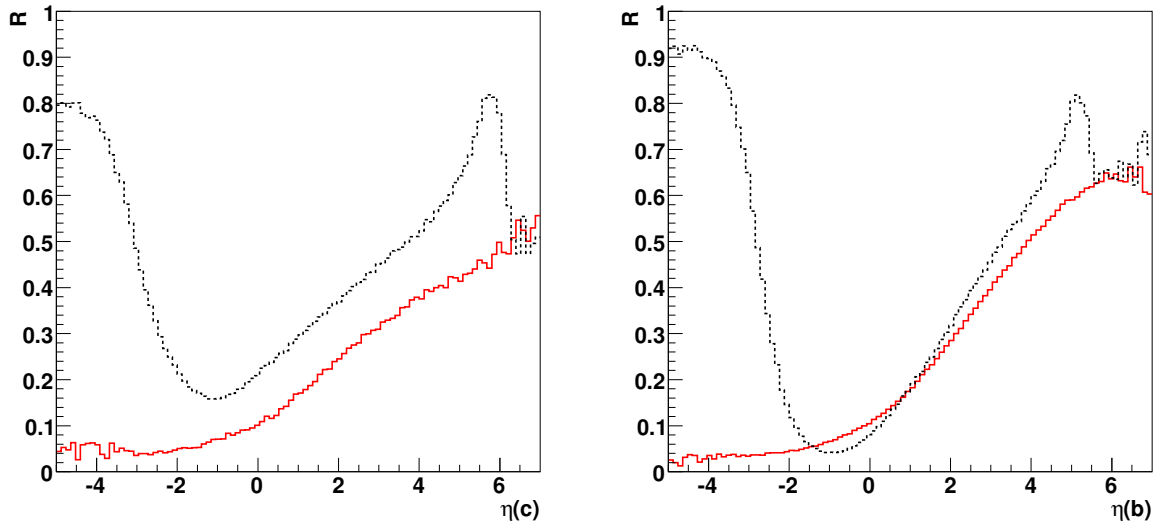


Figure 5.9: The ratio of the hadronic contribution to the total cross-section in MC@NLO (full red curve) and of the resolved contribution to the total cross-section in HERWIG (dashed black curve). The right hand figure show the distribution of b-quarks, and the left hand figure the distribution of c-quarks

| Ren. Scale Factor | Fact. Scale Factor | MC@NLO CS[pb] | LO CS[pb] |
|-------------------|--------------------|--------------------------|----------------------|
| 2 | 2 | 4431 ± 3 | 3015 ± 0.6 |
| 2 | 1 | 4292 ± 3 | 2745 ± 0.03 |
| 1 | 2 | 4934 ± 4 | 3622 ± 0.04 |
| 1 | 0.5 | 5578 ± 5 | 2778 ± 0.03 |
| 0.5 | 1 | 4635 ± 3 | 4159 ± 0.05 |
| 0.5 | 0.5 | 5547 ± 4 | 3499 ± 0.04 |

Table 5.4: The result for different scale choices in beauty production. The scale factors represent the number which multiplies the default scale $1/2(m_{\perp}(Q) + m_{\perp}(\bar{Q}))$.

respectively. For HERWIG, the resolved part contributes $\sim 29\%$ and $\sim 34\%$ respectively. The resolved and hadronic calculations are expected to move the heavy quarks closer to the proton in rapidity than in the direct and pointlike calculations respectively. In fig. 5.9 the ratio of the hadronic part of MC@NLO, to the total distribution, is shown as a function of rapidity of the heavy quark. There, one can see that for MC@NLO the hadronic contribution is only $\sim 5\%$ in the backwards region while it raises to $\sim 55\%$ in the forward region for charm production and to $\sim 65\%$ for beauty production. The resolved part for the HERWIG distribution dominates the cross-section with around 80% in both the forward and backward regions, while it contributes 20 – 40% in the central regions of the η spectrum of the heavy quark.

5.2 Scale Variations

To investigate how the cross-sections depend on the factorization scale μ_F in the PDFs and the renormalization scale μ_R in the definition of α_s , both scales have been varied independently. The variation is a factor of 2 up and down relative to the nominal value, which is:

$$\mu = \frac{1}{2} (m_{\perp}(Q) + m_{\perp}(\bar{Q})) . \quad (5.4)$$

This is the average transverse mass of the produced heavy quarks. The relative size of the scales lie in the interval $0.5 \leq \mu_F/\mu_R \leq 2$. This variation results in six independent calculations for each process. In tables 5.4 and 5.5 the resulting total cross-sections from MC@NLO and LO are shown. Here, one can see that the charm production cross-section has a stronger dependence on the scale choice than beauty-production. For the former case the difference between the largest and smallest cross-sections is a factor 2.2, while for beauty-production it is a factor 1.3. This is expected, since the mass of the b-quark is much larger than the mass of the c-quark, hence yielding larger scales. It is also shown that the scale dependence does get smaller at NLO than at LO. For charm production

| Ren. Scale Factor | Fact. Scale Factor | MC@NLO CS[nb] | LO CS[nb] |
|-------------------|--------------------|---------------|------------|
| 2 | 2 | 561.1±0.6 | 407.8±0.05 |
| 2 | 1 | 631.4±1.0 | 250.8±0.05 |
| 1 | 2 | 445.1±0.4 | 548.8±0.1 |
| 1 | 0.5 | 748.9±1.0 | 200.6±0.04 |
| 0.5 | 1 | 542.7±0.4 | 537.1±0.1 |
| 0.5 | 0.5 | 991.8±1.0 | 322.5±0.06 |

Table 5.5: The result for different scale choices in charm production. The scale factors represent the number which multiplies the default scale $1/2(m_{\perp}(Q) + m_{\perp}(\bar{Q}))$.

the largest to smallest LO cross-section differ by a factor 2.7, while for beauty production the factor is 1.5.

To see the difference between going from LO to NLO in more detail, one can look at the p_{\perp} and η distributions of the produced heavy quarks and vary the scales. In figure 5.10, the LO and NLO cross-sections are shown as distributions of p_{\perp} and η of the produced charmquarks. All six scale variations are included in the distributions and the resulting largest and smallest value in each bin is shown in the figure. In fig. 5.10 the ratio of the smallest value in each bin has been divided by the largest value, such that a large scale variation will yield a small ratio. In fig. 5.10 one can see that for large values of $p_{\perp}(c)$, the LO has a smaller scale dependence than the NLO calculation. This can be understood if one considers the scale choice. In the NLO calculation the average transverse mass of the heavy quark and anti-quark defines the scale. Event hough the heavy quark has a large transverse momentum the heavy antiquark may have a small p_{\perp} such that the scale is still relatively small. In the LO calculation the p_{\perp} of the heavy quark and antiquark are the same, which means that the scale in the LO calculation is always large for large values of $p_{\perp}(c)$. This does not mean that the LO calculation is more accurate for these values. In fig. 5.10 one can also see that the LO calculation is more dependent on the scale choice than the NLO calculation for $\eta(c) < 2$ while the dependeny is similar for $\eta(c) > 2$.

In figs. 5.12 and 5.11 similar comparisons between HERWIG and MC@NLO are shown. Here one can see the scale dependency is quite similar in the two programs for beauty production, while for charm production the difference is larger due to the small charm mass. Also here one can see that the LO MC calculation varies less for larger p_{\perp} of the heavy quark, especially in charm production. The MC@NLO prediction is less scale dependent over the whole η distributions of the heavy quarks.

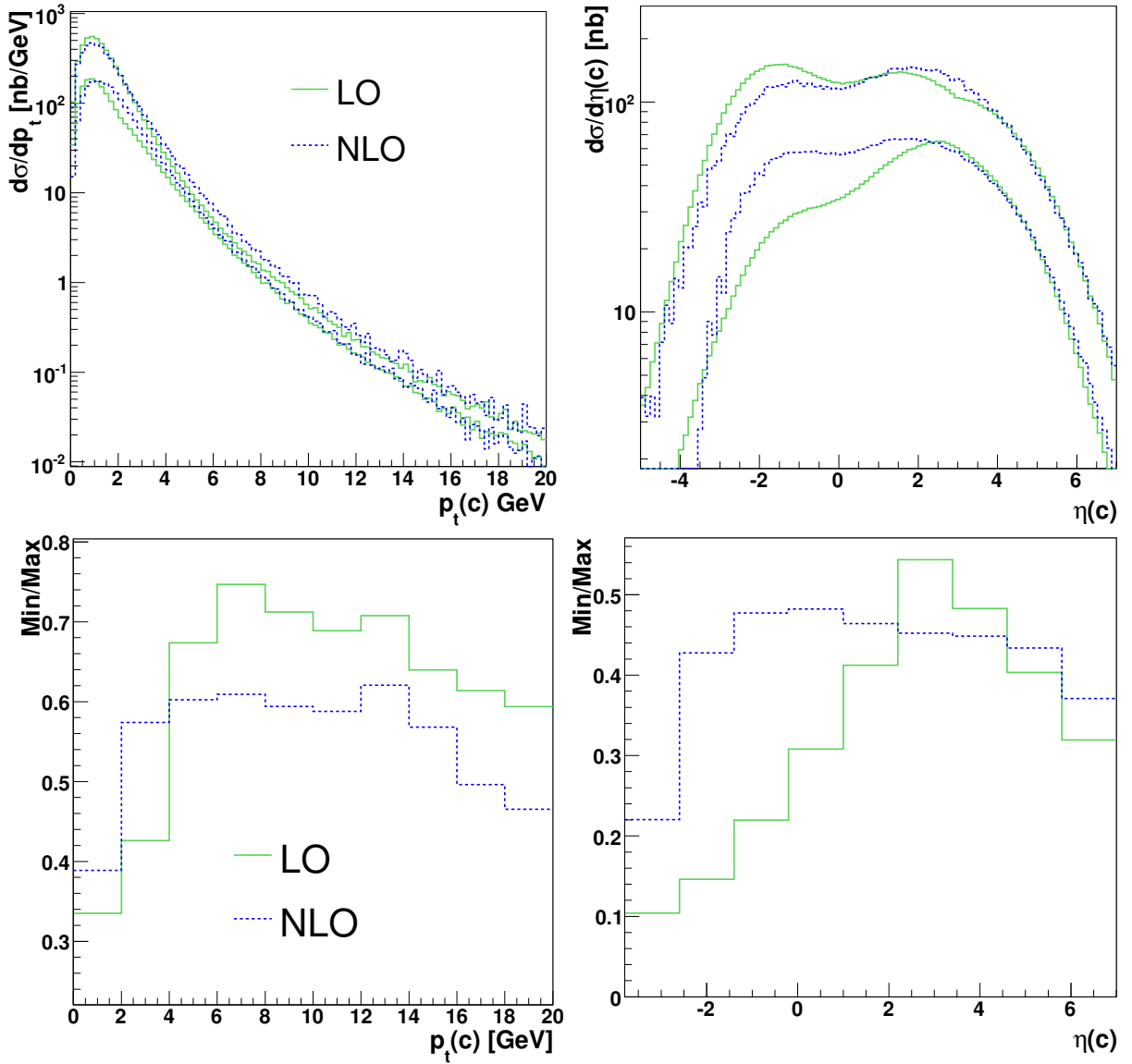


Figure 5.10: The p_{\perp} and η distribution of charmquarks with the FMNR program (NLO) and the Born approximation (LO). The scales are varied as described in the text. In the lower distributions, the smallest result in each bin has been divided by the largest. Thus, a small value corresponds to a large scale variation.

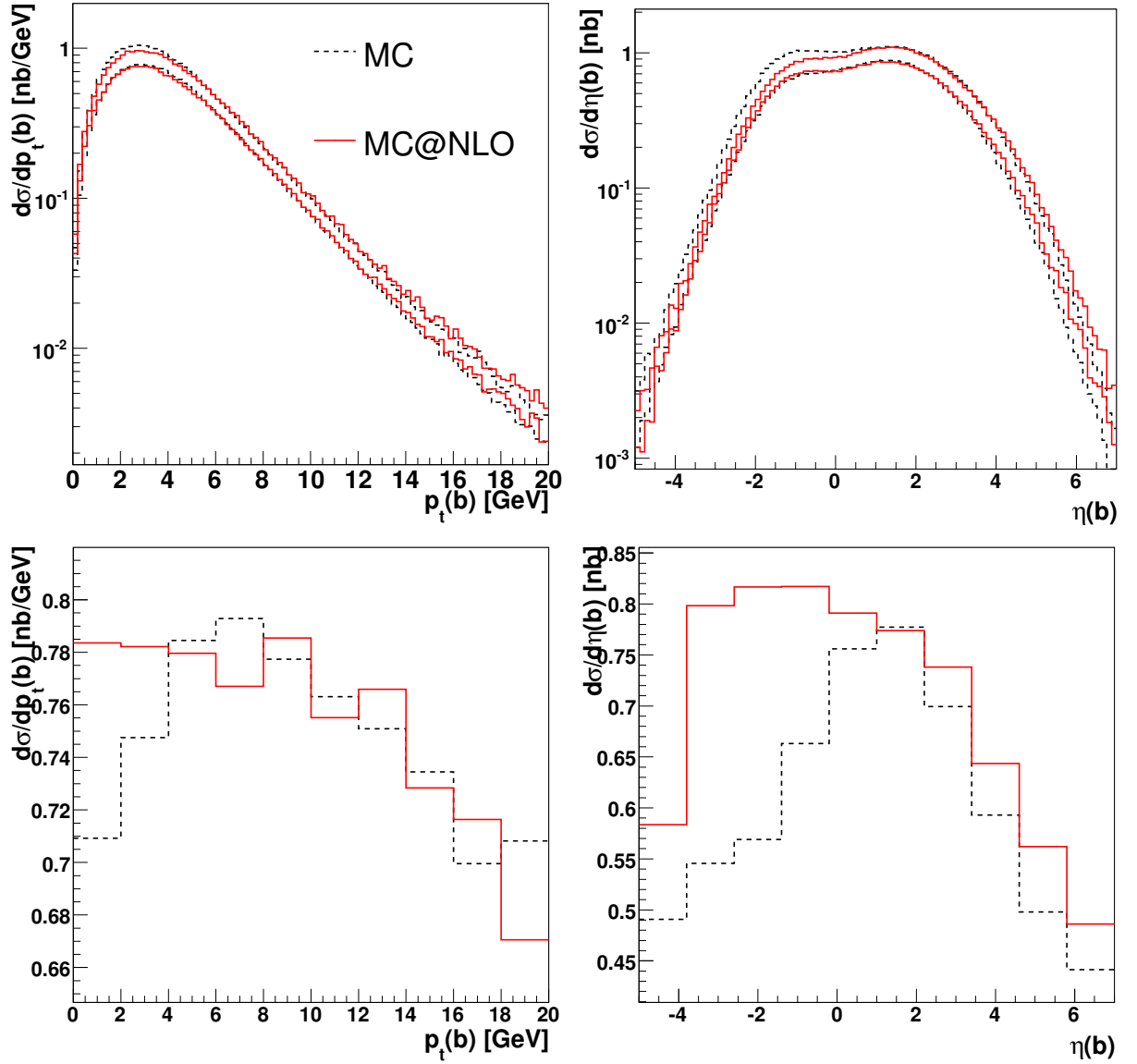


Figure 5.11: The distributions of p_{\perp} and η of b-quarks including six scale variations. The largest and smallest resulting value in each bin for both MC@NLO and HERWIG (MC) are shown. In the lower distributions, the smallest result in each bin has been divided by the largest. Thus, a small value corresponds to a large scale variation.

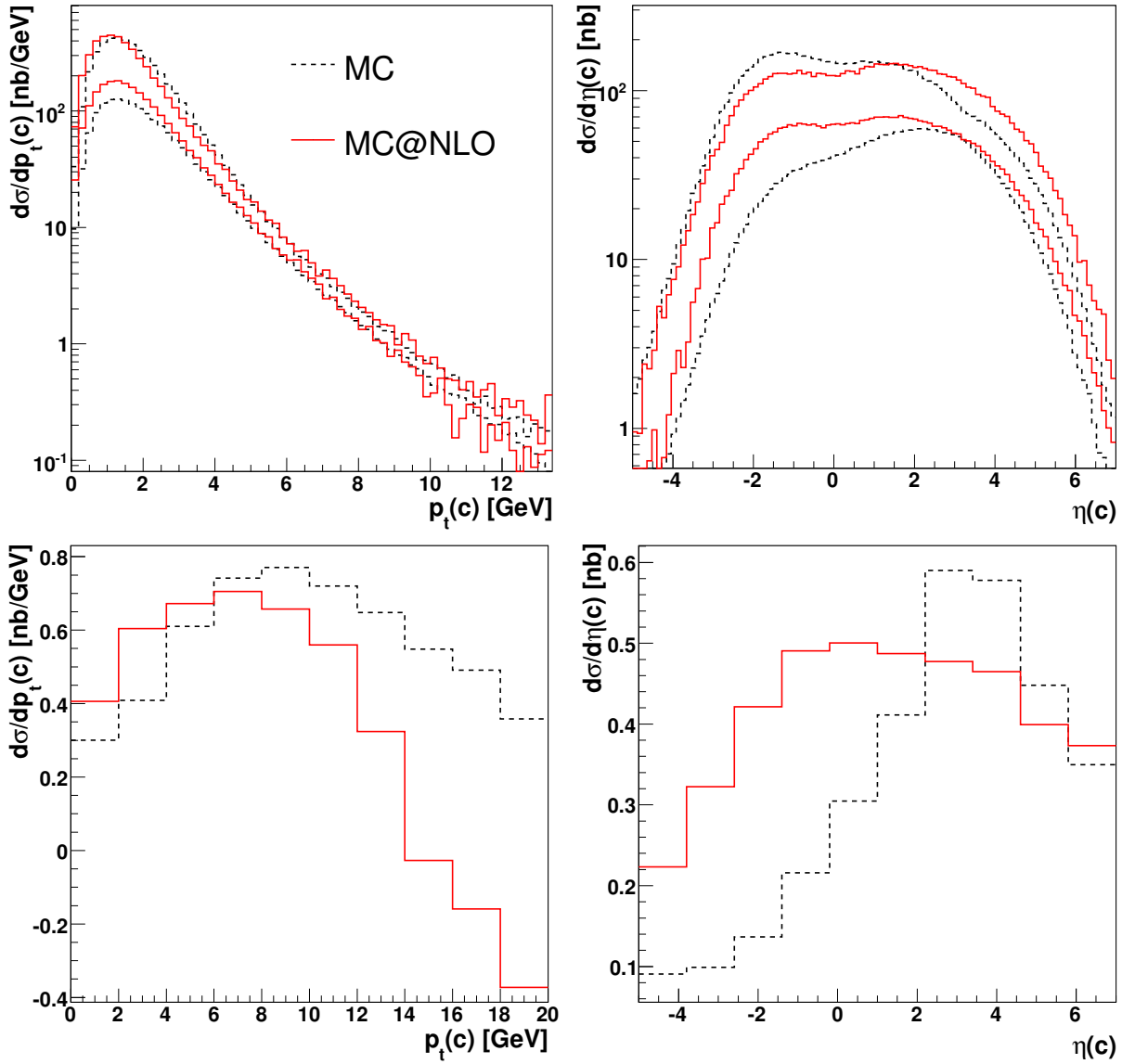


Figure 5.12: The distributions of p_{\perp} and η of c -quarks including six scale variations. The largest and smallest resulting value in each bin for both MC@NLO and HERWIG (MC) are shown. In the lower distributions, the smallest result in each bin has been divided by the largest. Thus, a small value corresponds to a large scale variation.

Chapter 6

Comparisons to Measurements of Heavy Quarks at HERA

When heavy-quarks are produced at HERA they hadronize before reaching the detectors H1 and ZEUS. Therefore, measuring heavy-quarks means measuring hadrons containing heavy valence quarks. In this chapter MC@NLO will be compared to measurements of the decay products of $D^{*\pm}$ mesons, which contain a valence charm-quark and of B mesons, which contain a valence beauty-quark. The MC@NLO prediction come with a full independent variation of the factorization and renormalization scales, as described in chapter 5. Comparisons are also made with the fixed order NLO-calculation FMNR [42] and HERWIG [15]. In this chapter, a selection of comparisons with measurements will be presented. The parameter settings of MC@NLO are described in chapter 5, table 5.1.

6.1 Comparisons to Measurements of $D^{*\pm}$ Mesons

The $D^{*\pm}$ mesons are detected through the so-called golden decay channel [50]:

$$D^{*\pm} \rightarrow D^0 \pi_{\text{slow}}^{\pm} \rightarrow K^{\mp} \pi^{\pm} \pi_{\text{slow}}^{\pm}. \quad (6.1)$$

Here the $D^{*\pm}$ meson decays strongly into a D^0 and a π^{\pm} . The small mass difference between the D^0 and $D^{*\pm}$ results in a pion created close to its mass-threshold. This pion will therefore be slow in the $D^{*\pm}$ center-of-mass system where it will have a speed of $v_{\pi} \sim 0.36c$. The D^0 is then decaying weakly into a K^{\mp} meson and into another π^{\pm} . The branching ratio for the golden decay channel is $\sim 2.6\%$ [51], which is comparatively low, but the advantage of this channel is that all the final state particles carry an electric charge, resulting in three charged tracks in the detectors. The three final-state mesons are then combined into $D^{*\pm}$ candidates and the signal is extracted.

The branching ratio of charm-quarks decaying into D^* mesons has in measurements been found to be $\Gamma(c \rightarrow D^*) = 0.235 \pm 0.007$ [52, 53]. These numbers are mainly extracted

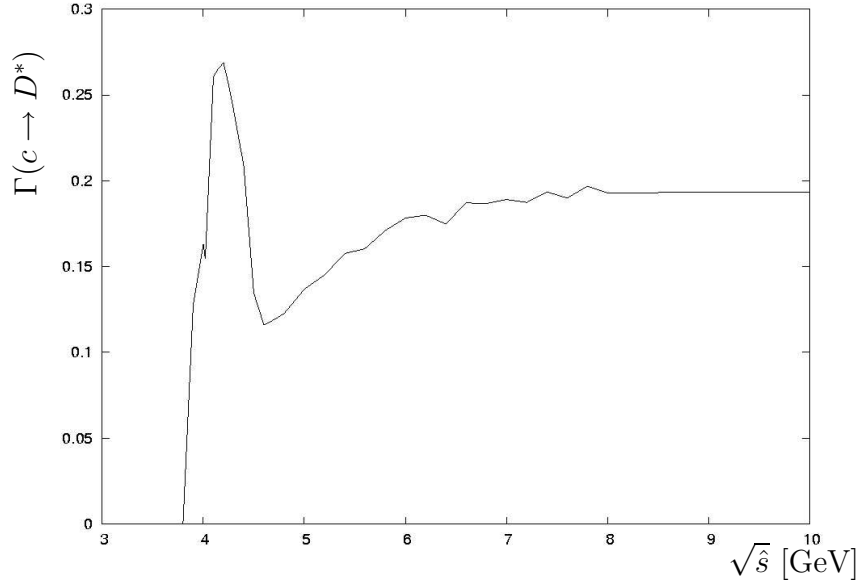


Figure 6.1: The branching ratio for $c \rightarrow D^*$ as a function of $\sqrt{\hat{s}}$ in HERWIG. Here the charm mass is $m_c = 1.5$ GeV.

from LEP data where electrons and positrons were colliding far from threshold energies for charm production. At HERA, where charm is produced by partonic interactions, heavy quarks are in general produced near the threshold, where $\hat{s} \simeq 4m_c^2$. Measurements of this branching ratio at HERA are however consistent with the LEP results, albeit with larger uncertainties.

In figure 6.1 the branching ratio $\Gamma(c \rightarrow D^*)$ in HERWIG is plotted as a function of \hat{s} with a charm mass of $m_c = 1.5$ GeV. There it can be seen, when going from low to high \hat{s} , that the branching ratio peaks at the mass resonance around twice the D^* mass $m_{D^*} = 4.02$ GeV, then goes down around the mass resonances of D_1 and D_2^* at 4.84-2.52 GeV, to finally level out around a branching ratio of ~ 0.195 . To get the total branching ratio of $c \rightarrow D^*$ in MC@NLO, the $\Gamma(c \rightarrow D^*)$ distribution has to be convoluted with the \hat{s} distribution and then integrated. This results in an integrated branching ratio of ~ 0.175 in MC@NLO, which is considerably smaller than the experimental one of 0.235. To compensate for this, all cross-sections from MC@NLO in this chapter has been scaled by a factor $1.34 \simeq 0.235/0.175$ ¹.

In this section MC@NLO will be compared to three $D^{*\pm}$ measurements. Two of these measurements are of inclusive D^* , and two of them include measurements of D^* mesons in jets. The three measurements are:

1. “Measurement of Inclusive and DiJet D^* -Meson Photoproduction at the H1 Experiment at HERA”, preliminary results by the H1 collaboration [50],

¹The alternative to this rescaling would be a complete retuning of all decays in the generator, which is outside the scope of this thesis.

| Analysis | H1-09 [50] | H1-06 [54] | ZEUS-05[55] |
|-------------------------|---------------------|------------------------|---------------------|
| \sqrt{s} | 318 GeV | 318 GeV | 318 GeV |
| Q^2 | $< 2 \text{ GeV}^2$ | $< 0.01 \text{ GeV}^2$ | $< 1 \text{ GeV}^2$ |
| y_{JB} | 0.1 – 0.8 | 0.29 – 0.65 | 0.19 – 0.87 |
| $p_t(D^*)$ | $> 1.8 \text{ GeV}$ | $> 2 \text{ GeV}$ | $> 3 \text{ GeV}$ |
| $\eta(D^*)$ | -1.5 – 1.5 | -1.5 – 1.5 | -1.5 – 1.5 |
| $\eta(\text{jet})$ | | -1.5 – 1.5 | -1.5 – 2.4 |
| $p_t(\text{jet}_{1,2})$ | | 4,3 GeV | |

Table 6.1: A summary of the cuts in the D^* meson measurements in this chapter.

| Visible C-S [nb] | Measured | MC@NLO |
|-----------------------|------------------|------------------|
| H1-09 | 38.60 ± 4.72 | 27.40 ± 3.13 |
| H1-06 inclusive D^* | 6.45 ± 0.83 | 6.45 ± 0.78 |
| H1-06 D^* +jets | 3.01 ± 0.44 | 2.88 ± 0.29 |
| ZEUS-05 | 6.80 ± 0.26 | 5.77 ± 0.42 |

Table 6.2: The resulting visible cross-sections from the cuts listed in table 6.1, for the different measurements as well for the MC@NLO predictions.

2. “Inclusive D^* -Meson Cross Sections and D^* -Jet Correlations in Photoproduction at HERA” by the H1 collaboration [54],
3. and “Inclusive jet cross sections and dijet correlations in $D^{*\pm}$ photoproduction at HERA” by the ZEUS collaboration [55].

To simplify the notation, these will be referred to as H1-09, H1-06 and ZEUS-05 respectively, after the year of their respective publication. The experimental cuts made for the D^* analyses are summarized in table 6.1. These cuts result in visible cross-sections listed in table 6.2, together with the theoretical predictions. There it can be seen that MC@NLO describe the H1-06 measurements very well and is slightly below the data in the other two.

To quantify the comparisons made in this chapter, χ^2/ndf has been calculated for each distribution shown. It is defined by:

$$\chi^2 = \sum_{\text{bins}} \frac{(\sigma_{\text{theory}} - \sigma_{\text{data}})^2}{\delta_{\text{theory}}^2 + \delta_{\text{data}}^2} \quad (6.2)$$

where σ is the cross-section (central value) and δ is the uncertainty in each bin. This is then divided by the number of bins. If the theory prediction is within one standard deviation of the data, $\chi^2/ndf < 1$. This is summarized in table 6.3 for each distribution.

| | |
|---|--------|
| H1-09 | MC@NLO |
| $p_t(D^*)$ | 1.32 |
| $\eta(D^*)$ | 1.86 |
| $\eta(D^*) p_t(D^*) > 4.5 \text{ GeV}$ | 0.97 |
| H1-06 inclusive | MC@NLO |
| $p_t(D^*)$ | 1.41 |
| $\eta(D^*)$ | 0.46 |
| $\eta(D^*) p_t(D^*) > 4.5 \text{ GeV}$ | 1.67 |
| H1-06 D^* +jet | MC@NLO |
| $p_t(D^*)$ | 2.49 |
| $\eta(D^*)$ | 0.52 |
| x_γ^{obs} | 1.94 |
| $\Delta\phi(D^*, \text{jet})$ | 0.67 |
| $\Delta\eta(D^*, \text{jet})$ | 0.28 |
| ZEUS-05 | MC@NLO |
| $p_t(D^*)$ | 0.94 |
| x_γ^{obs} | 1.05 |
| $\Delta\phi(D^*, \text{jet})$ | 1.37 |
| $p_t(\text{jj})$ | 1.01 |
| M_{jj} | 1.42 |
| $\eta(\text{untagged jet}) p_t(\text{jet}) > 9 \text{ GeV}$ | 0.78 |

Table 6.3: The χ^2/ndf for all distributions in $D^{*\pm}$ -measurements shown in this chapter.

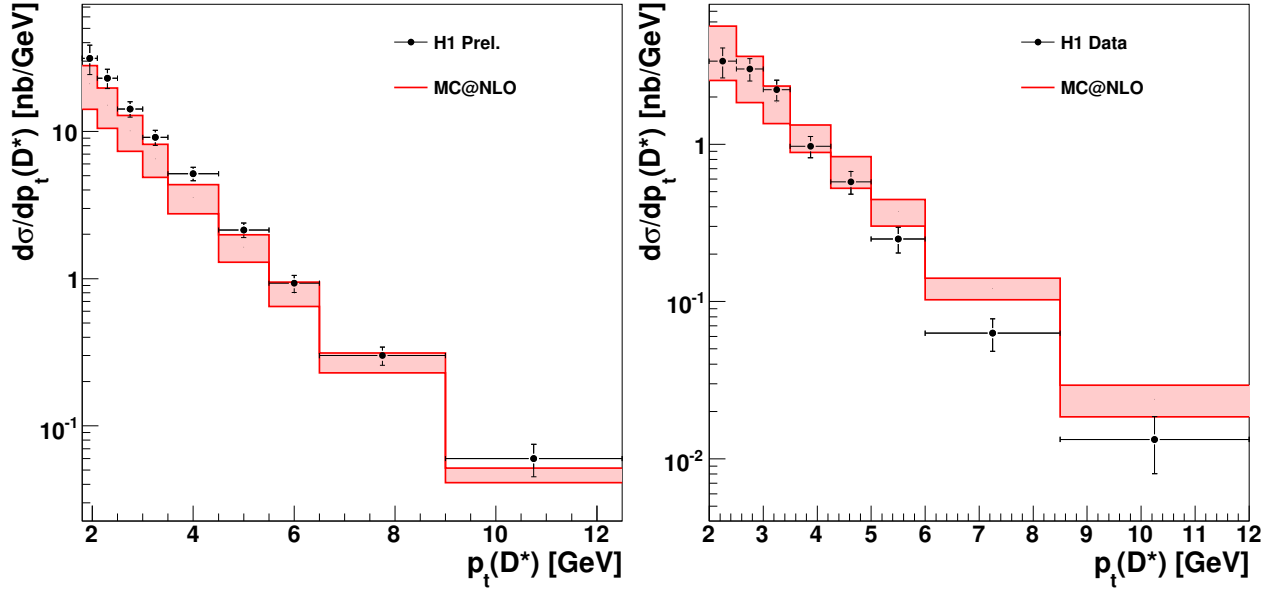


Figure 6.2: Distributions of $p_t(D^*)$ of inclusive D^* measurements from H1-09 (left) and H1-06 (right). The MC@NLO band includes full independent scale variations.

Comparisons to Inclusive Measurements of $D^{*\pm}$ -mesons.

In fig. 6.2 the $p_t(D^*)$ spectra are shown for inclusive D^* measurements. There it can be seen that MC@NLO describes both measurements well, within the scale variations. When looking at the distributions in pseudo-rapidity of the D^* mesons in fig. 6.3, one sees that the MC@NLO prediction is a bit below the data in the H1-09 measurement. This distribution still gives a $\chi^2/ndf = 1.86$, which means that the description is reasonable. The H1-06 measurement is well described. However, it can be seen in these distributions that the scale uncertainties in the MC@NLO prediction are rather large in comparison with the experimental uncertainties. In the $p_t(D^*)$ distributions, it can be seen that these scale uncertainties are reduced for larger $p_t(D^*)$. In this region the scales are larger, and therefore the dependence upon them are expected to be smaller.

In fig. 6.4 the $\eta(D^*)$ distribution is therefore shown for $p_t(D^*) > 4.5$ GeV. In this region the scales uncertainties in MC@NLO are at the same level as the experimental uncertainties. Here, both distributions are well described except for in one bin in the H1-06 measurement.

Comparisons to Measurements of $D^{*\pm}$ -mesons and Jets.

When demanding the existence of a hard jet, as well as a $D^{*\pm}$ meson, the scale dependencies in MC@NLO are expected to be smaller. In fig. 6.5, the $p_t(D^*)$ and $\eta(D^*)$ distributions from the H1-06 measurements are shown, when events with a hard jet with $p_t(\text{jet}) > 4$ GeV are chosen. As can be seen, the scale dependence is indeed reduced.

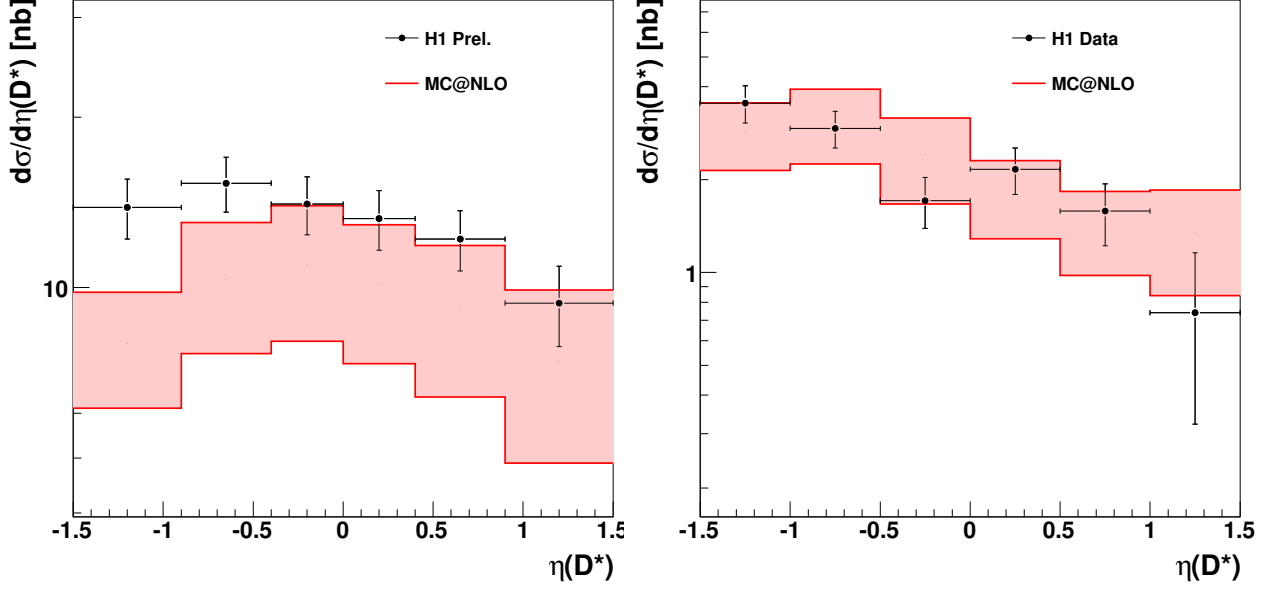


Figure 6.3: Distributions of $\eta(D^*)$ of inclusive D^* measurements from H1-09 (left) and H1-06 (right). The MC@NLO band includes full independent scale variations.

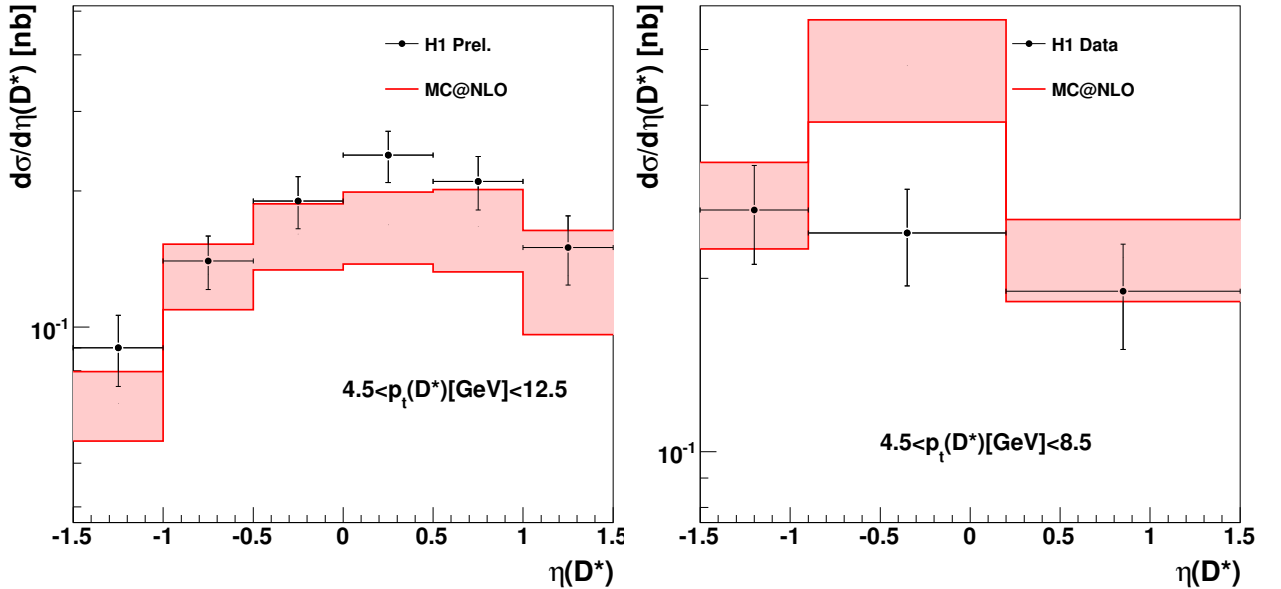


Figure 6.4: Distributions of $\eta(D^*)$ of inclusive D^* measurements from H1-09 (left) and H1-06 (right) for $p_t(D^*) > 4.5$ GeV. The MC@NLO band includes full independent scale variations.

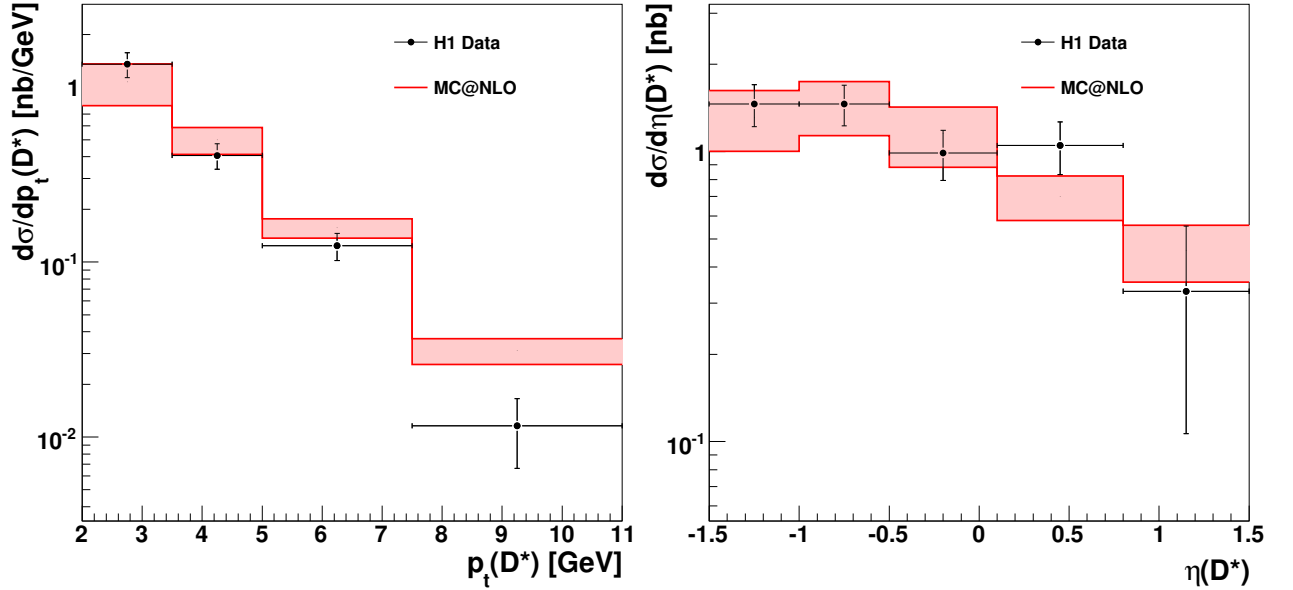


Figure 6.5: Distributions of $p_t(D^*)$ and $\eta(D^*)$ in the $D^* + \text{jets}$ measurements from H1-06. The MC@NLO band includes full independent scale variations.

The data are still well described, even though the $p_t(D^*)$ spectrum is a bit harder in MC@NLO than in the data. In fig. 6.6, the $p_t(D^*)$ spectrum from the ZEUS-05 measurement is shown². There the opposite is observed, that the MC@NLO prediction is slightly below the data for small $p_t(D^*)$, but describing the rest of the spectrum well.

Also, correlations between D^* mesons and jets have been measured in H1-06 and ZEUS-05. The relation:

$$x_\gamma^{\text{obs}}(\text{jet}_1, \text{jet}_2) = \frac{P_-(\text{jet}_1) + P_-(\text{jet}_2)}{\sum_{\text{All hadrons } i} P_-(i)} \quad (6.3)$$

is the fraction of total measured P_- taken by the two leading jets. All P_- in the collision is coming from the electron, and at LO the fraction x_γ^{obs} corresponds to the fraction of the virtual photon's energy which goes into the hard interaction. Therefore, the hadronic part of the calculation is expected to be more important for small values of x_γ^{obs} . In fig. 6.7, distributions in x_γ^{obs} are shown from H1-06 and ZEUS-05. There one can see that the contribution by the hadronic part of MC@NLO is larger in the H1-06 measurement, because of a stricter cut in Q^2 in this measurement. However, MC@NLO is slightly above the data for large x_γ^{obs} in this measurement, while the whole spectrum is well described in the ZEUS-05 measurement.

In chapter 5, some observables which are sensitive to higher order effects were described. One of these observables is the difference in azimuthal angle between the c-quark and the hardest other parton, which was shown in fig. 6.8. This corresponds to the difference in

²This distribution is not present in [55], but is a compilation of other distributions binned in $p_t(D^*)$.

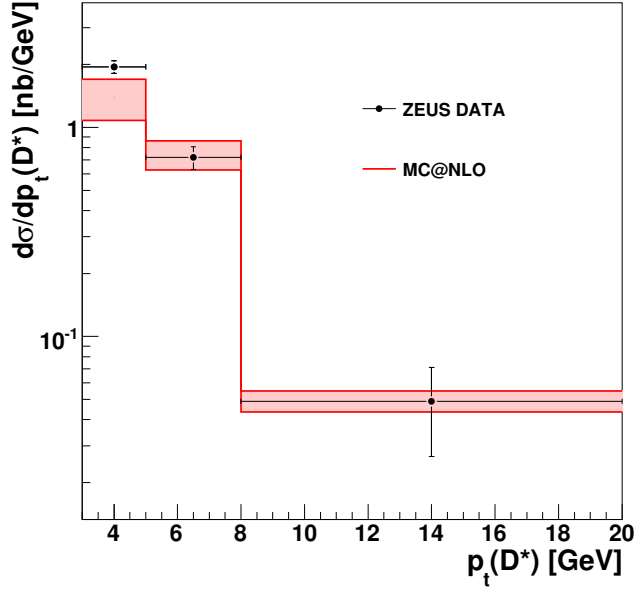


Figure 6.6: Distributions of $p_t(D^*)$ measurements from ZEUS-05. The MC@NLO band includes full independent scale variations.

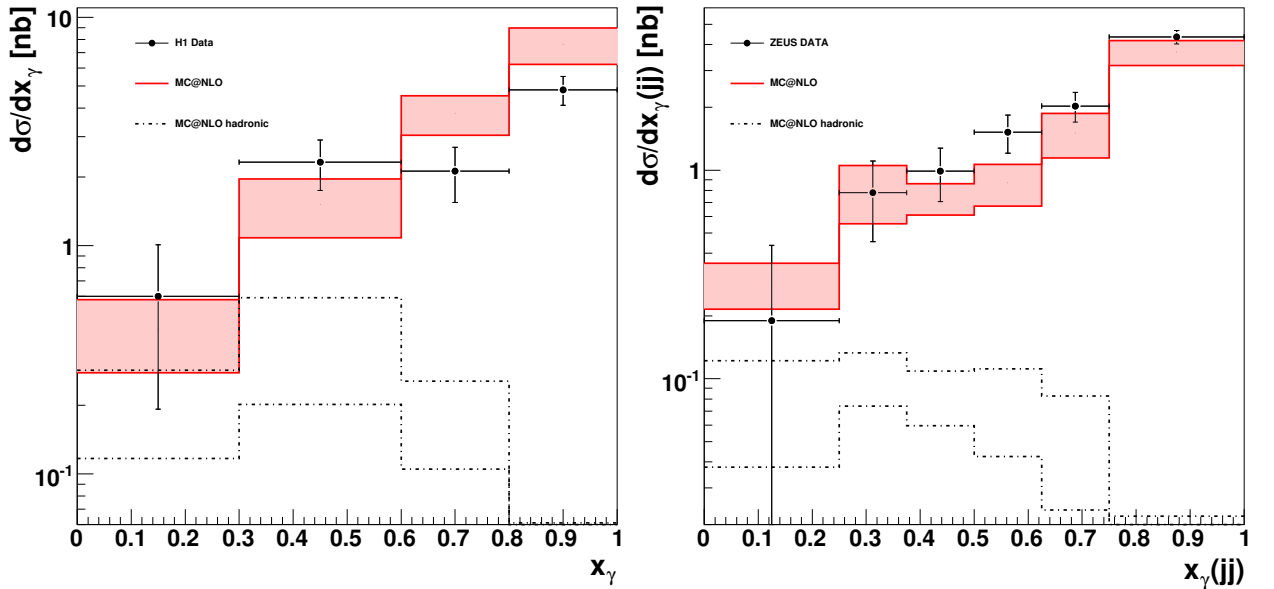


Figure 6.7: Distributions of $x_\gamma^{\text{obs}}(\text{jets})$ from H1-06 (left) and ZEUS-05 (right). The MC@NLO band includes full independent scale variations.

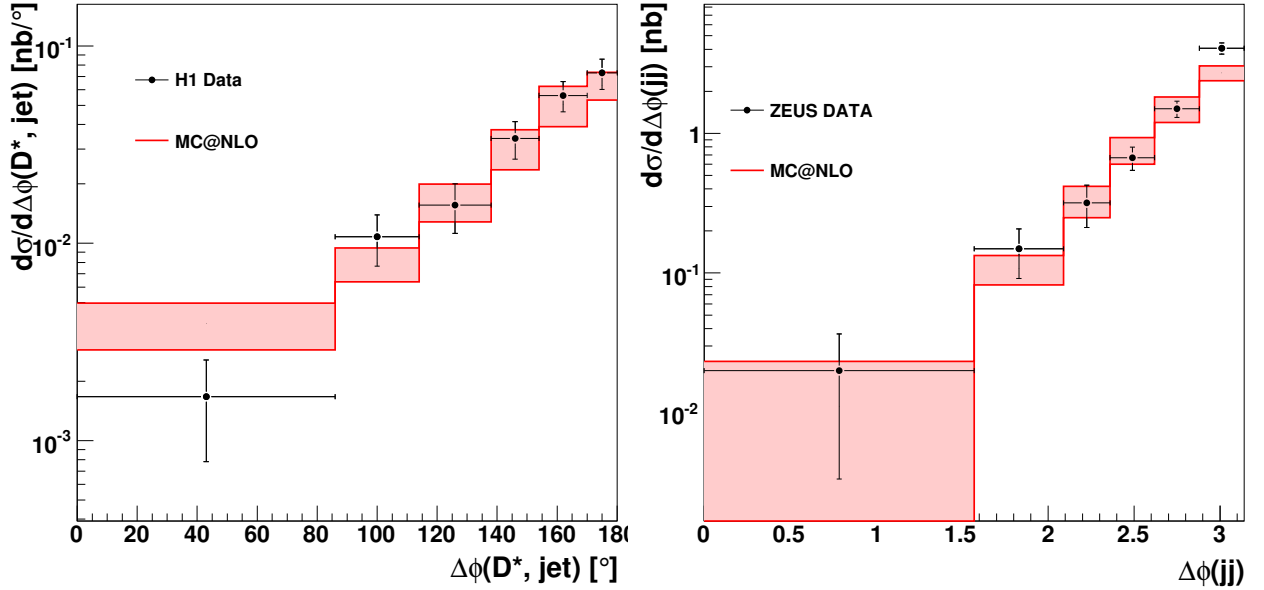


Figure 6.8: Distributions of $\Delta\phi$ from H1-06 (left) and ZEUS-05 (right). The MC@NLO band includes full independent scale variations.

azimuthal angle between the D^* meson and the hardest jet not containing the D^* in H1-06, or between the two hardest jets in ZEUS-05. These distributions are shown in fig. 6.8. There one can see that MC@NLO describes the data over the whole $\Delta\phi$ spectrum for both analyses.

Another observable which is sensitive to higher order effects at parton level is the combined p_t of the heavy quark antiquark pair, which was shown in fig. 5.4. At hadron level this corresponds to the combined p_t of the two leading jets, which was measured in ZEUS-05, as shown in fig. 6.9. In this figure, the distribution of the invariant mass of the two jets is also shown, defined by $M_{jj} = \sqrt{(p(\text{jet}_1) + p(\text{jet}_2))^2}$. At leading order this corresponds to the center of mass energy of the hard interaction. MC@NLO is shown to describe both these observables well.

Also, the difference in pseudo-rapidity between the D^* and the hardest other jet is sensitive to higher order radiations. At partonlevel, the two hardest emissions will more often be close to each other in rapidity in HERWIG than in NLO-calculations. As can be see in fig. 6.10, MC@NLO is describing the spectrum in $\Delta\eta(D^*, \text{jet})$ very well, with $\chi^2/ndf = 0.28$.

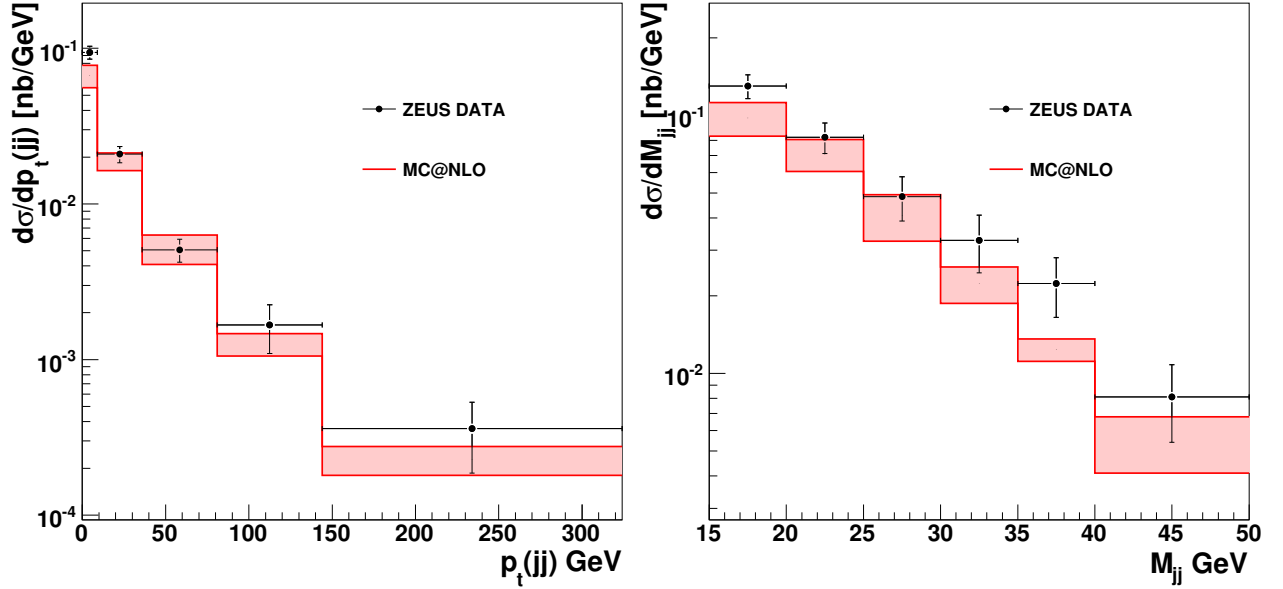


Figure 6.9: Distributions of $p_t(jj)$ and M_{jj} from ZEUS-05. The MC@NLO band includes full independent scale variations.

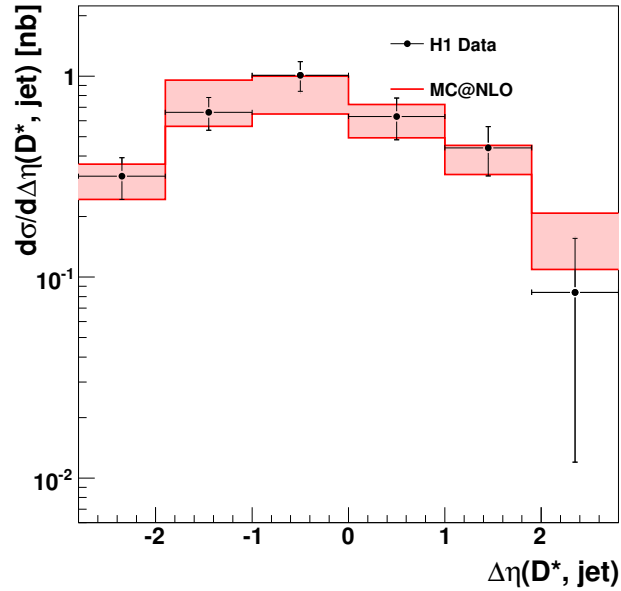


Figure 6.10: Distributions of $\Delta\eta(D^*, \text{jet})$ in H1-06. The MC@NLO band includes full independent scale variations.

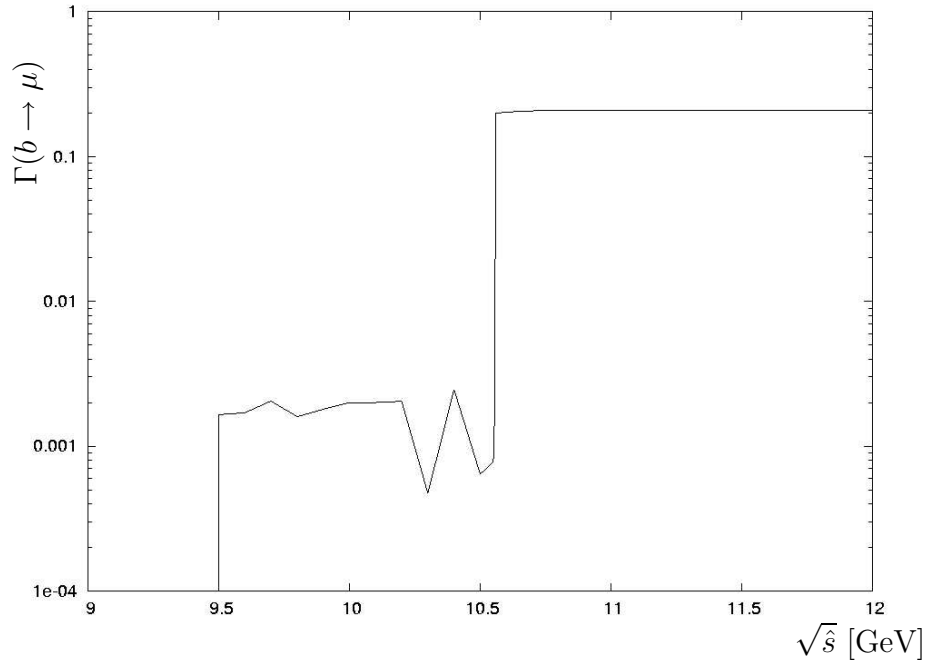


Figure 6.11: The branching ratio for $b \rightarrow \mu$ as a function of $\sqrt{\hat{s}}$ in HERWIG. Here the beauty mass is $m_b = 4.75$ GeV.

6.2 Comparisons to Beauty Measurements

When a beauty-quark is extracted from the proton, a jet is produced which is highly correlated in energy and momentum with the original quark, due to the large mass of the b-quark. The b-quark decays before it reaches the detector and is detected by its decay products. The b-quark decays weakly to lighter quarks, and the produced W^\pm boson may decay into muons. These muons will in general have a large momentum transverse to the jet-axis, so called $p_t^{\text{rel.}}$. Also, the vertex from which these muons are radiated will be displaced relative to the hard interaction of the event, and this displacement is proportional to the lifetime of the b-quark. Often, only the transverse component δ of this displacement is used in the b -tagging. These two methods of tagging the b-quarks may also be combined to further enhance the signal.

In fig. 6.11, the branching ratio $\Gamma(b \rightarrow \mu)$ in HERWIG is plotted as a function of \hat{s} with a beauty mass of $m_b = 4.75$ GeV. The threshold for $b\bar{b}$ -production is at $\hat{s} = 9.5$ GeV, while the threshold for B -hadron production is at $\hat{s} = 10.6$ GeV, above which the branching ratio is $\Gamma(b \rightarrow \mu) \sim 0.20$. When convoluting this with the MC@NLO calculation, one gets $\Gamma(b \rightarrow \mu) \sim 0.148$. The measured value is $\Gamma(b \rightarrow \mu) \sim 0.2205$ [51]. To compensate for this difference, all MC@NLO distributions in this section which depend on this branching ratio have been multiplied by a factor of 1.5.

In this section, comparisons will be made with three measurements at HERA. They are

| Analysis | ZEUS-08 | H1-05 | ZEUS-03 |
|-------------------------|---------------------|---------------------|---------------------|
| \sqrt{s} | 318 GeV | 318 GeV | 318 GeV |
| Q^2 | $< 1 \text{ GeV}^2$ | $< 1 \text{ GeV}^2$ | $< 1 \text{ GeV}^2$ |
| y_{JB} | 0.2 – 0.8 | 0.2 – 0.8 | 0.2 – 0.8 |
| $p_t(\mu)$ | $> 2.5 \text{ GeV}$ | $> 2.5 \text{ GeV}$ | $> 2.5 \text{ GeV}$ |
| $\eta(\mu)$ | -1.6 – 1.3 | -0.55 – 1.1 | -1.48 – 2.3 |
| $p_t(\text{jet}_{1,2})$ | 7, 6 | 7, 6 | 7, 6 |
| $\eta(\text{jet})$ | -2.5 – 2.5 | -2.5 – 2.5 | -2.5 – 2.5 |

Table 6.4: A summary of the cuts in the beauty analyses in this chapter.

| Visible C-S [pb] | Measured | MC@NLO |
|------------------|------------------------|------------------|
| ZEUS-08 | $38.6^{+5.78}_{-6.02}$ | 42.08 ± 4.91 |
| H1-05 | 38.4 ± 6.38 | 33.71 ± 2.89 |
| ZEUS-03 | 50.25 ± 6.45 | 48.39 ± 3.87 |

Table 6.5: The resulting visible cross-sections from the cuts listed in table 6.4, for the different measurements as well as for the MC@NLO predictions.

1. “Measurement of beauty photoproduction using decays into muons in dijet events at HERA”, by the ZEUS collaboration [56],
2. “Measurement of beauty production at HERA using events with muons and jets”, by the H1 collaboration [57],
3. and “Bottom photoproduction measured using decays into muons in dijet events in ep collisions at $\sqrt{s} = 318 \text{ GeV}$ ”, by the ZEUS collaboration [58].

These will be referred to as ZEUS-08, H1-05 and ZEUS-03 respectively. The first two uses the combined method of both p_t^{rel} and δ in the tagging of the b -quarks while in ZEUS-03 only p_t^{rel} is used. The experimental cuts made for the beauty analyses are summarized in table 6.4. These cuts result in the visible cross-sections listed in table 6.5, as well as the different theory predictions. There it can be seen that MC@NLO gives good predictions for all three visible cross-sections.

In fig. 6.12 the transverse momentum spectra of the selected muons is shown. There it can be seen that MC@NLO is describing all three data-sets well. Also, the scale variations are significantly smaller here, than for the comparisons with D^* mesons, due to the larger scale provided by the b -quark. Also, the experimental uncertainties are larger here. This means that the uncertainties from MC@NLO are at the same level as those of the measurements, or smaller. Also the rapidity distributions of the muons are well described by MC@NLO in all three data sets, as can be seen in fig. 6.13.

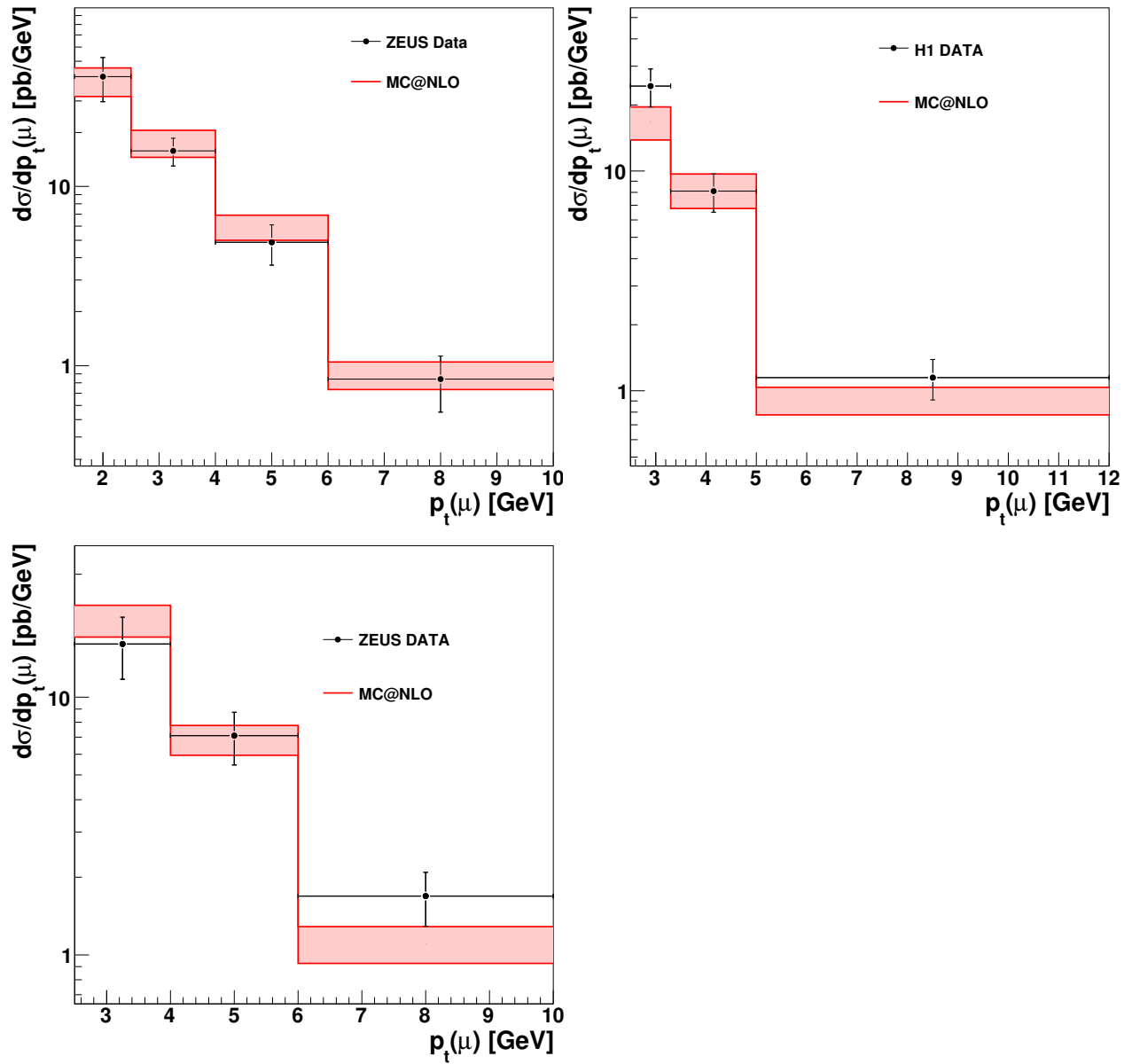


Figure 6.12: Distributions of $p_t(\mu)$ from the measurements ZEUS-08 (upper left), H1-05 (upper right) and ZEUS-03 (bottom). The MC@NLO band includes full independent scale variations.

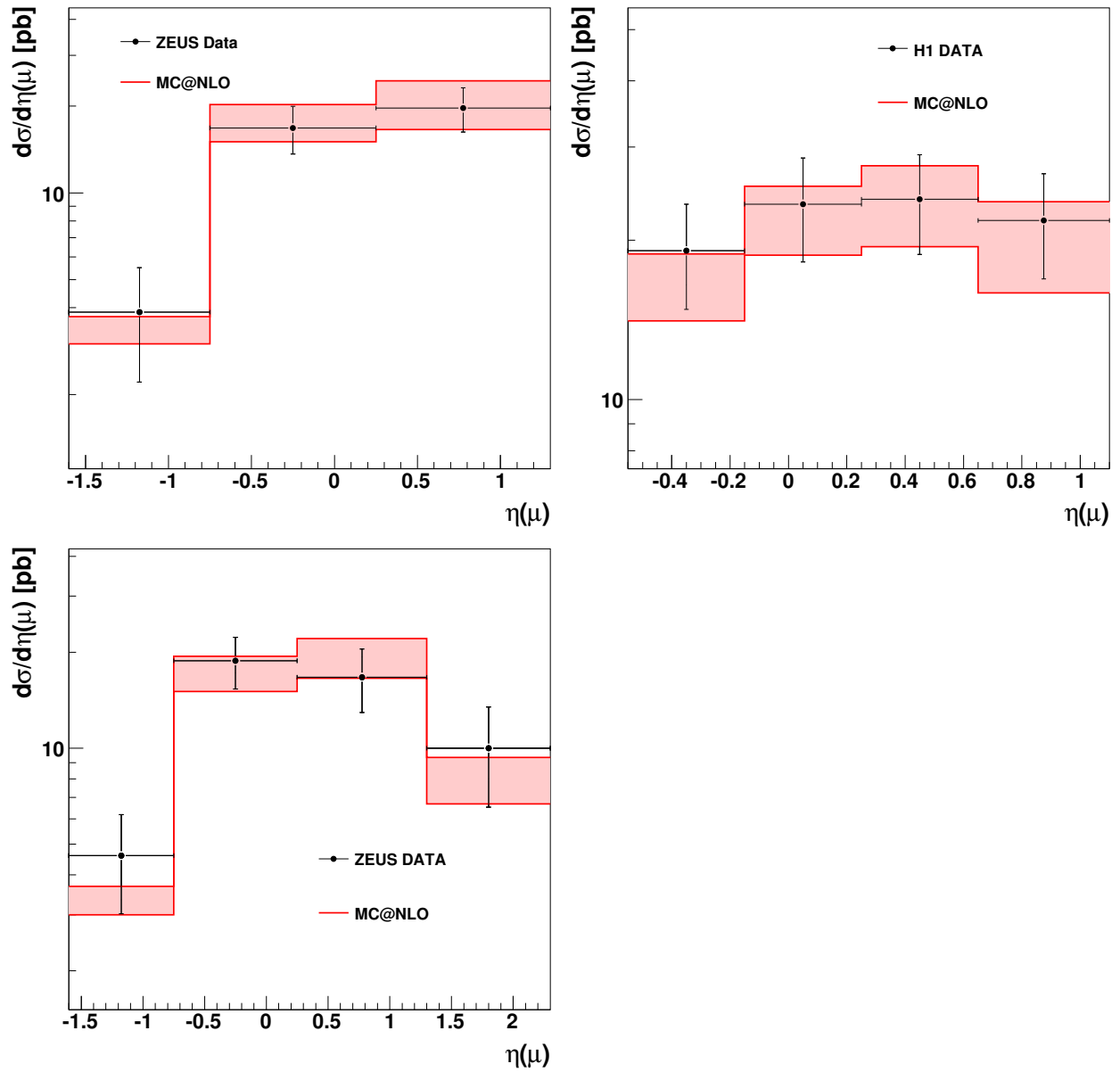


Figure 6.13: Distributions of $\eta(\mu)$ from the measurements ZEUS-08 (upper left), H1-05 (upper right) and ZEUS-03 (bottom). The MC@NLO band includes full independent scale variations.

| | |
|--|--------|
| ZEUS-08 | MC@NLO |
| $p_t(\mu)$ | 0.18 |
| $\eta(\mu)$ | 0.05 |
| $x_\gamma(\text{jets})$ | 0.59 |
| $\Delta\phi(\text{jets})$ | 1.22 |
| $\Delta\phi(\text{jets}) x_\gamma^{\text{obs}} < 0.75$ | 0.52 |
| H1-05 | MC@NLO |
| $p_t(\mu)$ | 0.89 |
| $\eta(\mu)$ | 0.11 |
| $x_\gamma(\text{jets})$ | 0.48 |
| ZEUS-03 | MC@NLO |
| $p_t(\mu)$ | 0.78 |
| $\eta(\mu)$ | 0.34 |
| $p_t(b - \text{jet})$ | 0.09 |
| $p_t(b)$ | 0.65 |
| $x_\gamma(\text{jets})$ | 0.17 |

Table 6.6: The χ^2/ndf for all distributions in the beauty measurements shown in this chapter.

In fig. 6.14 the p_t of the jet containing the b -quark is shown, as measured by ZEUS-03. This spectrum is then used to reconstruct the p_t spectrum of the b -quarks, with FMNR. As can be seen, both distributions are well described by MC@NLO. The $p_t(b)$ spectrum is not dependent upon the branching ratio $\Gamma(b \rightarrow \mu)$, described above.

Two types of correlations has been measured for beauty production. One is the x_γ^{obs} distributions of the leading two jets in the measurements, which are shown in fig. 6.15. MC@NLO are describing all these distributions well. As can be seen, the hadronic part of the calculation becomes significant for $x_\gamma^{\text{obs}} < 0.75$.

In fig. 6.16 the difference in azimuthal angle between the leading jets is shown from the ZEUS-08 measurement. MC@NLO is describing this distribution well. This observable has also been binned in large and small x_γ^{obs} . There it can be seen that for small $\Delta\phi$, MC@NLO is slightly below the data in the small x_γ^{obs} bin, which is compensated for large x_γ^{obs} .

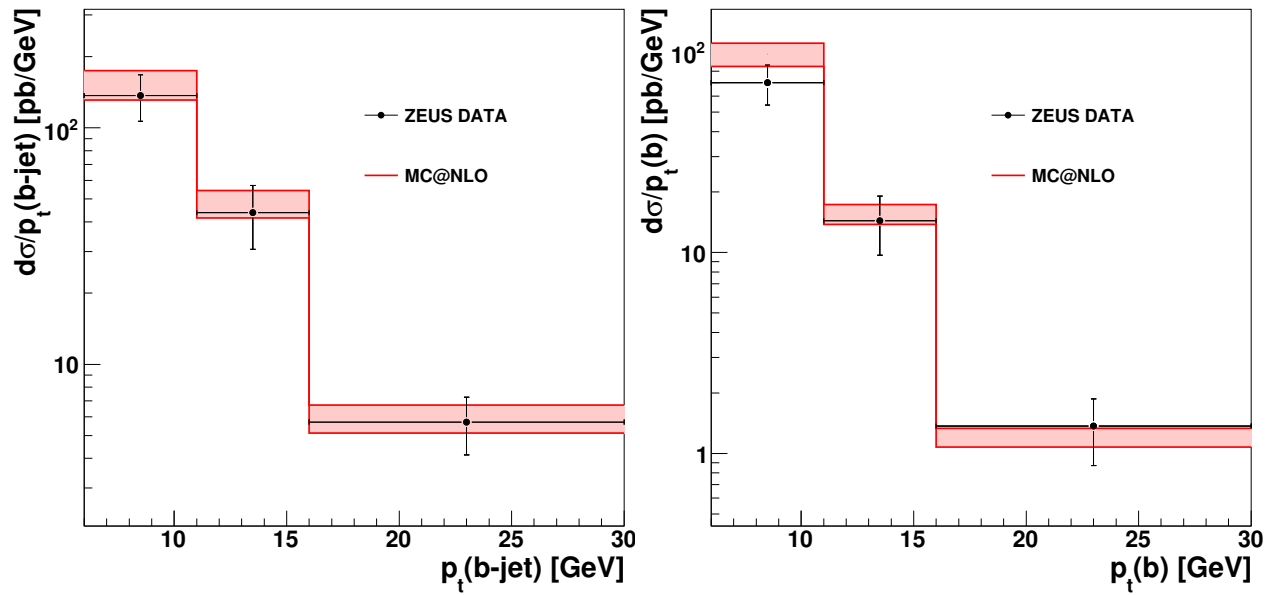


Figure 6.14: Distributions of $p_t(b - \text{jet})$ and $p_t(b)$ from the measurement ZEUS-03. The MC@NLO band includes full independent scale variations.

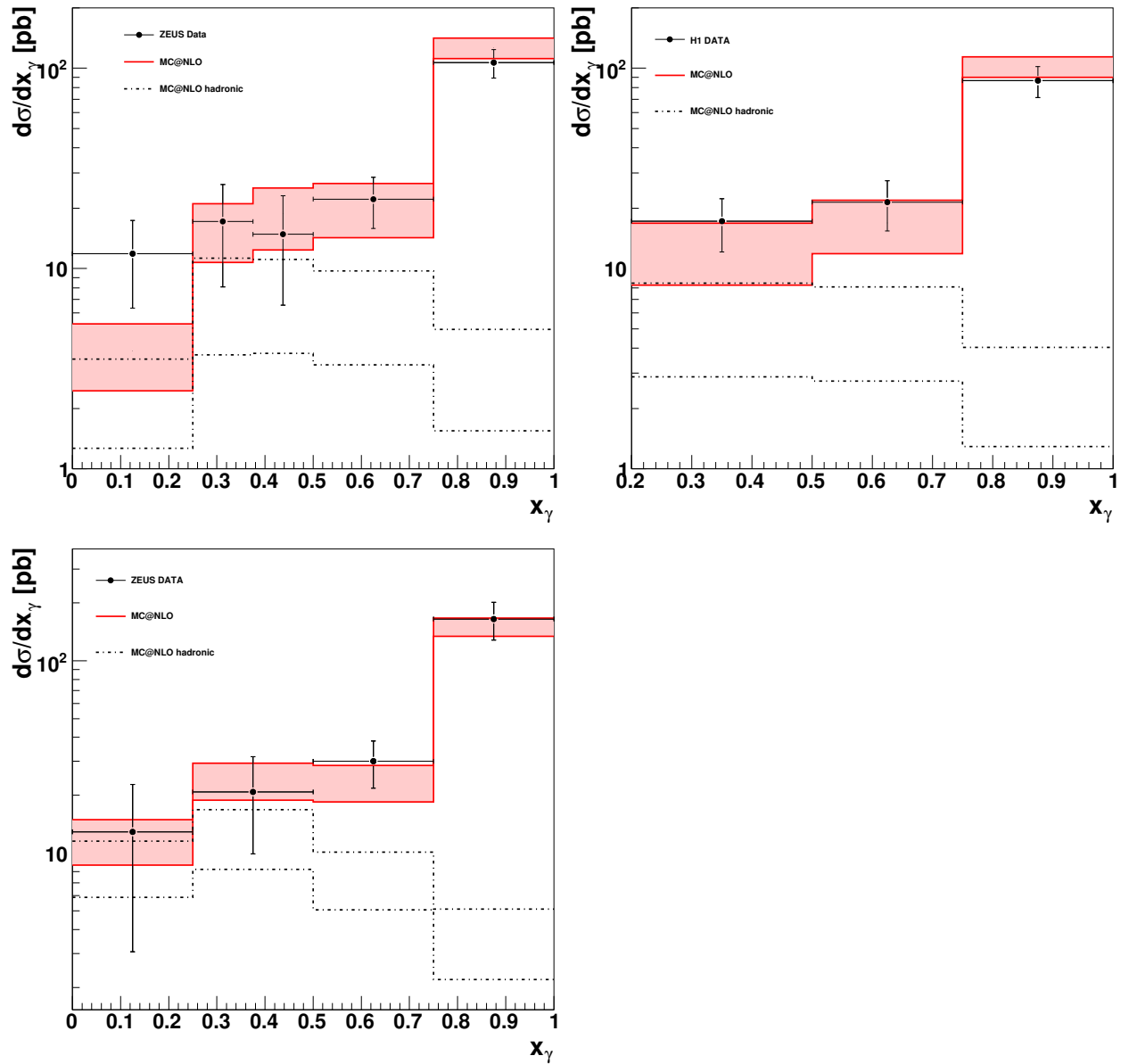


Figure 6.15: Distributions of x_γ^{obs} from the measurements ZEUS-08 (upper left), H1-05 (upper right) and ZEUS-03 (bottom). The MC@NLO band includes full independent scale variations.

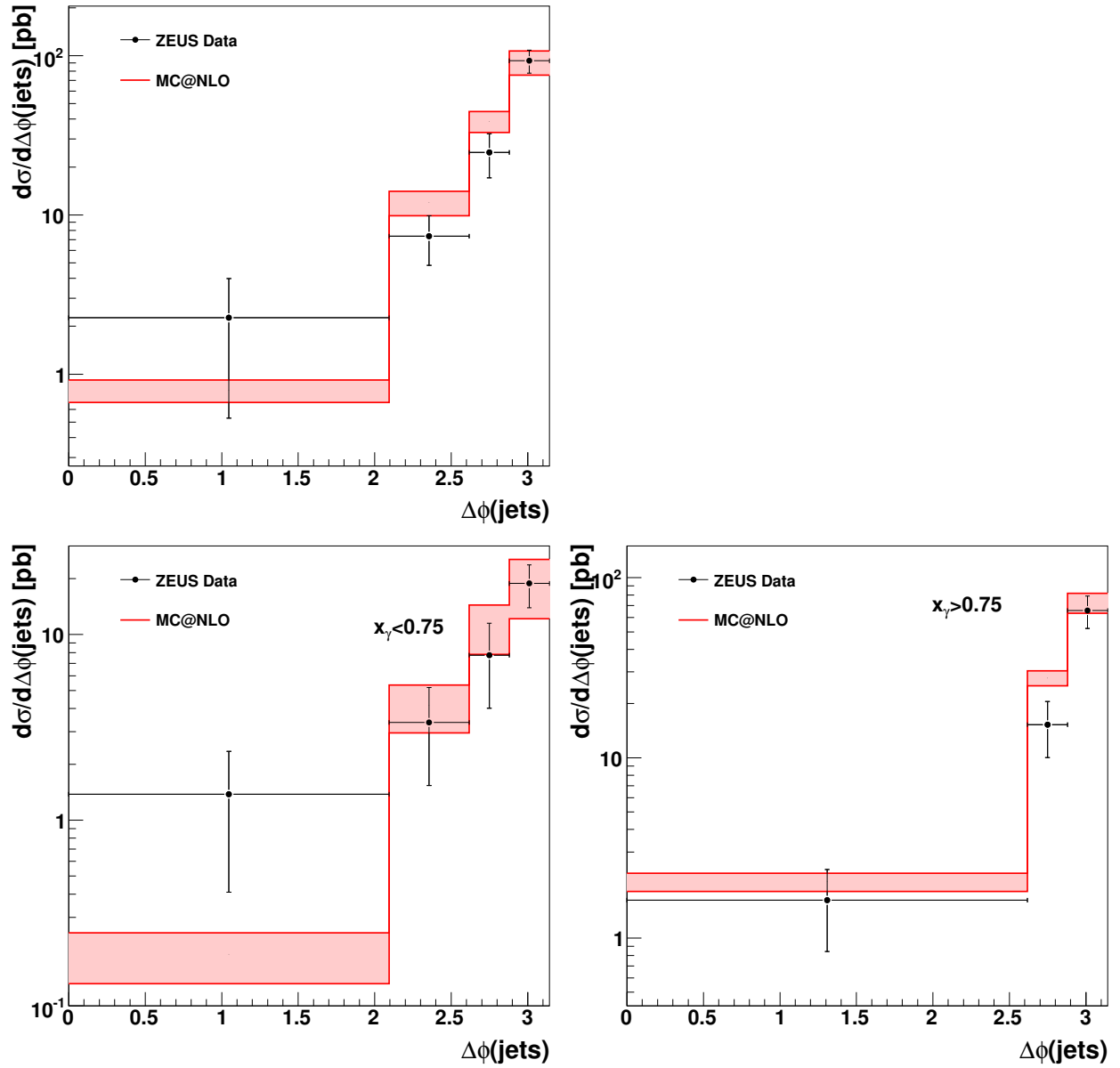


Figure 6.16: Distributions of $\Delta\phi(\text{jets})$, unbinned and binned in $x_\gamma^{\text{obs}}(\text{jets})$. The MC@NLO band includes full independent scale variations.

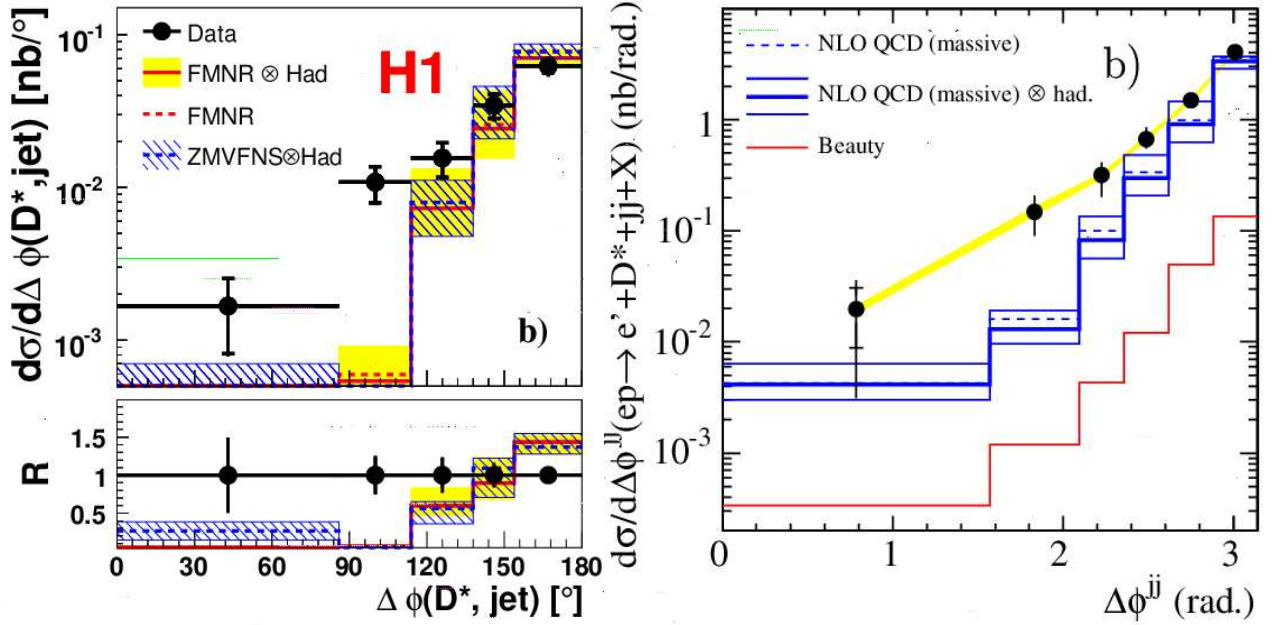


Figure 6.17: Distributions of $\Delta\phi$ from H1-06 [54] and from ZEUS-05 [55] as compared to the NLO calculation in the FMNR program.

6.3 Comparisons with Other Calculations

In fig. 6.17 it is again shown the $\Delta\Phi$ distributions from the H1-06 and the ZEUS-05 measurements. This time they have been compared with the FMNR program, which has been attached to the Lund string fragmentation model to provide hadrons. There it can be seen that for this observable, which were well described by MC@NLO in fig. 6.8 cannot be described by the FMNR program for small azimuthal separations between the D^* and the jet or between the jets. Sometimes, the a hard parton ends up in a hadron outside of the visible region, which makes it possible for FMNR to have a small value of $\Delta\Phi$. As can be seen in the plots, these are suppressed compared to the data.

6.4 Conclusions

In this chapter, MC@NLO has been compared to six measurements, three of D^* mesons and three of beauty production. All data has been shown to be described within one sigma by MC@NLO. However, the distributions from the program need large factors to compensate for wrong branching ratios. That both the $p_t(b - \text{jet})$, which is compensated by this factor, and $p_t(b)$, which is not, are well described by MC@NLO indicates that this approach is acceptable.

For inclusive measurements of D^* mesons the uncertainties in MC@NLO are found to be

large, compared to the experimental uncertainties. These uncertainties are reduced for large $p_t(D^*)$ or when a hard jet is required in the measurement.

For beauty production, the uncertainties given by MC@NLO are at most at the same level as the experimental uncertainties, and often much smaller.

Chapter 7

Summary and Outlook

In chapter 6 it is shown that the MC@NLO program constructed in this thesis is able to describe all available data of heavy flavours produced in photoproduction at HERA, including some observables which the FMNR NLO program is not able to describe. Also, in chapter 5, the uncertainty due to scale variations has been shown to be smaller in MC@NLO than in HERWIG, and it comes with a full fragmentation package well fitted with the parton shower, something which is not the case for FMNR.

The program needs large factors to compensate for threshold effects in the fragmentation functions implemented in HERWIG. For the branching ratio $\Gamma(c \rightarrow D^*)$ the cross-sections need a scaling factor of 1.34 and for $\Gamma(b \rightarrow \mu)$ the factor is 1.5. To remedy this problem, a tuning of HERWIG fragmentation parameters to HERA data would be desirable. Such a tuning has been outside the scope of this thesis.

So far, MC@NLO has only been implemented with matching to the HERWIG parton shower. The same techniques could also be implemented in a matching with the PYTHIA parton shower. The wide use of the PYTHIA event generator makes it a project which would be both very useful for the community and achievable in the near future. If implementing the process described in this thesis, namely heavy quarks produced in photoproduction, Monte Carlo subtraction terms would have to be calculated both for the pointlike and the hadronic parts of the calculation. The hadronic part of the photon is in principle only different from other hadrons by different PDF sets. Therefore, an implementation of this process in PYTHIA would also be able to describe heavy flavours produced in any hadron-hadron scattering, for example at the Large Hadron Collider (LHC), which will start to collide protons within the next couple of months.

In chapter 2.5, it is briefly described why the DGLAP evolution is expected to be invalid for small x_{Bj} and Q^2 , where the ordered parton chains are expected to be suppressed. Typically there are on the order of 1 emission in a parton chain per unit of rapidity. The MC@NLO presented in this thesis calculate the first emission exactly, and the rest of the parton evolution is then calculated by the parton shower. This approach has been shown to be sufficient to describe all HERA data of heavy flavour photoproduction. The

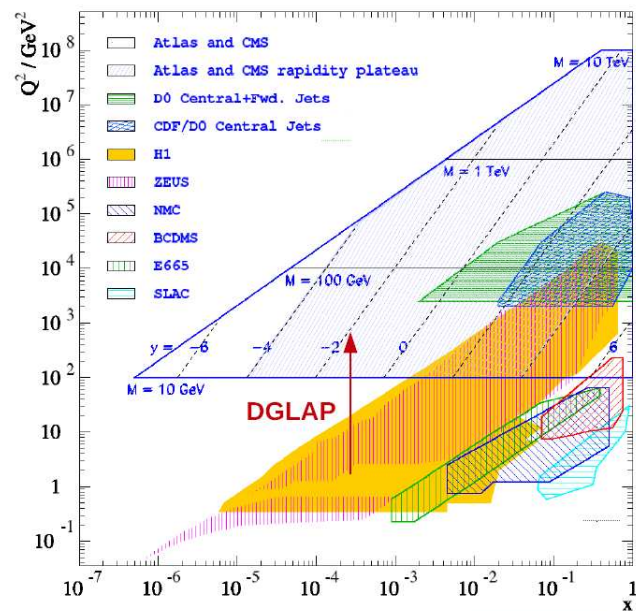


Figure 7.1: The detectable phase-space in x and Q^2 for the LHC experiments (within the blue lines). Lines of constant rapidity are included in the plot. Also compared with other existing experiments, including the ones at HERA (H1 yellow full and ZEUS red vertical lines)[59]

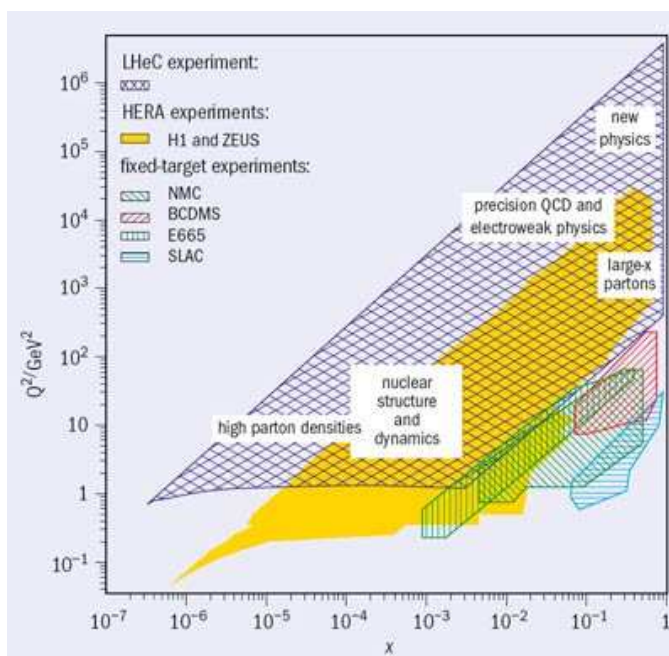


Figure 7.2: The detectable phase-space in x and Q^2 for the LHeC project (dark blue, checked). Also compared with other existing experiments, including the ones at HERA (yellow full) [60].

available phase-space at HERA for non-DGLAP evolution is however rather restricted. The detectors measure radiations from parton chains with a rapidity difference of $\Delta y \simeq 4$.

In fig. 7.1 the expected phase-space for the LHC is drawn as well as the one for HERA. There it is seen that the HERA phase-space extends much further in the direction of small Q^2 than the LHC, but on the other hand, the LHC experiment can offer a much larger rapidity coverage, of around 11 units, which will provide a possibility to test the limits of the DGLAP approach at small x . To further test these limits a new electron-hadron collider would be needed. One such suggestion is the large hadron electron collider (LHeC). An estimate of the phase space of LHeC is shown in fig. 7.2. Since it will use parts of the LHC, the angular coverage may be similar as for the LHC but the phase-space extends further for small Q^2 . If the LHeC is constructed, it will provide an important testing ground for perturbative QCD and the MC@NLO presented in this thesis may be a valuable tool for these tests.

Hamburg, the 27th of October 2009.

Appendix A

Dimensional Regularization

In quantum field theory there are two kinds of divergencies present in the calculations: ultra-violet divergencies, which are present in loop-integrals and correspond to large mass scales, and infra-red divergencies, corresponding to soft or collinear radiations. These cases are depicted in fig. A.1. There exist several methods to regularize these divergencies, but the most widely used is dimensional regularization [61]. The goal in dimensional regularization is to either transform all IR-divergencies appearing in the calculation into poles in an arbitrary complex number ϵ , or to regularize UV-divergencies with an effective cut-off scale μ , which gets absorbed into the definitions of the couplings and masses.

The idea behind dimensional regularization is to change the dimensionality of an integral from an integer number into a non-integer, or even complex, number. This is a very abstract concept which only works for quantities which are allowed to have non integer dimensions. One example on how such generalization can occur is to observe that the volume of a d -sphere, i.e. a sphere in d dimensions, can be written in a form with Euler's gamma-functions:

$$\Gamma(z) = \int_0^\infty t^{z-1} e^{-t} dt \quad (\text{A.1})$$

such that

$$V_d = \frac{1}{d} \frac{2\pi^{d/2}}{\Gamma(d/2)}. \quad (\text{A.2})$$

For $d = 1, 2$ and 3 the result is $2, \pi$ and $4\pi/3$ respectively. The Euler gamma functions are however not only defined for integers, but for all complex numbers z with real part $\text{Re}(z) > 0$. In this way, the volume of a sphere may be defined in non-integer and even complex dimensions.

To dimensional regularize a d -dimensional integral, the following steps have to be taken:

1. The integral is transformed from being d -dimensional into being of arbitrary dimension n . The integral is still expected to describe the same physics, however. In this

step the unit of the integral may change, which then has to be compensated by a suitable arbitrary parameter μ^{d-n} , where μ has the same dimension as the original integration variable.

2. A variable substitution is performed into $n - 1$ dimensional polar coordinates, such that $2d^n x = d\Omega_n x^{n-1} dx$.
3. The arbitrary dimension n is allowed to become non-integer by the transformation $n = d - 2\epsilon$, where ϵ is a complex number with $Re(\epsilon) > 0$.
4. The integration is performed.
5. The limit $\epsilon \rightarrow 0$ is taken where possible.

Regulating an IR-divergency

As an example where for an IR divergency with $d = 1$, consider the integral in eq. (1.71), which was regularized by a soft cut-off κ for small k_\perp :

$$\frac{\hat{\sigma}_{\text{QCDC}}(z, Q^2)}{\hat{\sigma}_0} = \frac{e_i^2 \alpha_s}{2\pi} P_{qq}(z) \int_0^{\hat{s}} \frac{dk_\perp^2}{k_\perp^2} \quad (\text{A.3})$$

Instead, using dimensional regularization, taking the steps above, it becomes:

$$\begin{aligned} \int_0^{\hat{s}} \frac{dk_\perp^2}{k_\perp^2} &\rightarrow \int_0^{\hat{s}} \frac{d^n k_\perp^2}{k_\perp^2} (\mu^2)^{1-n} = \frac{(\mu^2)^{1-n}}{2} \int_0^{\hat{s}} d\Omega_n \int_0^{\hat{s}} \frac{(k_\perp^2)^{n-1}}{k_\perp^2} dk_\perp^2 \\ &= (\mu^2)^{1-n} \frac{\pi^{n/2}}{\Gamma(n/2)} \int_0^{\hat{s}} \frac{dk_\perp^2}{(k_\perp^2)^{2-n}} \end{aligned} \quad (\text{A.4})$$

where eq. (A.2) has been used in the last step. Letting $n = 1 - 2\epsilon$ this becomes:

$$\begin{aligned} (\mu^2)^{2\epsilon} \frac{\pi^{\frac{1-2\epsilon}{2}}}{\Gamma\left(\frac{1-2\epsilon}{2}\right)} \int_0^{\hat{s}} \frac{dk_\perp^2}{(k_\perp^2)^{1+2\epsilon}} &= (\mu^2)^{2\epsilon} \frac{\pi^{\frac{1-2\epsilon}{2}}}{\Gamma\left(\frac{1-2\epsilon}{2}\right)} \frac{1}{-2\epsilon} [(k_\perp^2)^{-2\epsilon}]_0^{\hat{s}} \\ &= (\mu^2)^{2\epsilon} \frac{\pi^{\frac{1-2\epsilon}{2}}}{\Gamma\left(\frac{1-2\epsilon}{2}\right)} \frac{1}{-2\epsilon} \left(\frac{\hat{s}}{\mu^2}\right)^{2\epsilon} \\ &= \frac{1}{-2\epsilon} + \ln\left(\frac{\hat{s}}{\mu^2}\right) + \mathcal{O}(\epsilon) \end{aligned} \quad (\text{A.5})$$

where the limit $\epsilon \rightarrow 0$ has been taken where possible, and the equality $\Gamma(1/2) = \sqrt{\pi}$ has been used. Here it is seen that what was previously a soft divergency for small k_\perp has now been transformed into a $1/\epsilon$ pole. Also, with $\hat{s} = Q^2(1-z)/z$ and $\mu^2 = \mu_F^2$ being the factorization scale, the same result is obtained as in chapter 1.1.3. The final result for the integral in eq. (A.3) is:

$$\int_0^{\hat{s}} \frac{dk_\perp^2}{k_\perp^2} = \ln\left(\frac{Q^2}{\mu_F^2}\right) + \frac{1}{-2\epsilon} + \ln\left(\frac{1-z}{z}\right) \quad (\text{A.6})$$

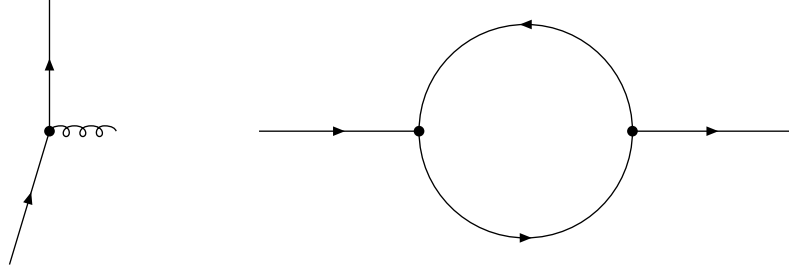


Figure A.1: To the left: the radiation of a gluon is IR singular when the energy of the gluon is 0 or if the gluon becomes collinear with the radiating quark. To the right: a one-loop diagram, which is UV singular for large momenta in the loop.

where, the pole in epsilon is absorbed by the definition of the PDF, either in the DIS or the $\overline{\text{MS}}$ subtraction scheme.

Regulating a UV-divergency

An example of a UV-divergent integral is the scalar one-loop self energy integral, which is the integral one gets by applying the Feynman rules on a one-loop diagram, such as the one in fig. A.1 [1]:

$$G^{(2)}(p) = i \int \frac{d^4 k}{(2\pi)^4} \frac{1}{(k^2 - m^2 + i\epsilon)((p-k)^2 - m^2 + i\epsilon)} \quad (\text{A.7})$$

This integral is UV-divergent as $k \rightarrow \infty$. This is however only the case when the dimensionality, n , of the integral is $n \geq 4$. To simplify the example, the integral will be taken in four-dimensional Euklidian space, such that the $i\epsilon$ factors in the denominator can be set to 0. Before beginning the steps above, the integral may be rewritten further, with a Feynman-parametrization:

$$\frac{1}{AB} = \int \frac{dx}{(xA + (1-x)B)^2} \quad (\text{A.8})$$

Using this for the denominator in the integral $G^{(2)}(p)$, it becomes in n dimensions:

$$\begin{aligned} G^{(2)}(p, n) &= i\mu^{4-n} \int \frac{d^n k}{(2\pi)^n} \int_0^1 \frac{dx}{(k^2 - 2xp \cdot k + xp^2 - m^2)^2} \\ &= i\mu^{4-n} \int \frac{d^n l}{(2\pi)^n} \int_0^1 \frac{dx}{(l^2 + x(1-x)p^2 - m^2)^2} \end{aligned} \quad (\text{A.9})$$

where the variable substitution $l = k - xp$ has been used in the last step. In this form it is easy to change variables into polar coordinates:

$$G^{(2)}(p, n) = i\mu^{4-n} \frac{\Omega_n}{(2\pi)^n} \int_0^1 dx \int_0^\infty \frac{dl l^{n-1}}{(l^2 + x(1-x)p^2 - m^2)^2} \quad (\text{A.10})$$

To compute the integral over l one may use some properties of Euler's gamma-function [1]:

$$\begin{aligned}
\Gamma(n) &= (n-1)! \quad \text{For integers } n \geq 1 & (\text{A.11}) \\
\Gamma(z-1) &= \frac{\Gamma(z)}{(z-1)} \quad \text{For all } z, \text{Re}(z) > 1 \\
\int_0^\infty dy \frac{y^{w-1}}{(y+1)^{w+z}} &= \frac{\Gamma(w)\Gamma(z)}{\Gamma(w+z)} \\
\frac{1}{\Gamma(z)} &= z + \gamma_E z^2 + \left(\frac{\gamma^2}{2} - \frac{\pi^2}{12}\right) z^3 + \dots
\end{aligned}$$

where the last equation is a Taylor expansion around $z = 0$ with γ_E being the Euler constant. Rewriting the integral and using this yields:

$$\begin{aligned}
G^{(2)}(p, n) &= i\mu^{4-n} \frac{\Omega_n}{(2\pi)^n} \int_0^1 dx (x(1-x)p^2 - m^2)^{\frac{n}{2}-2} \int_0^\infty dl \frac{l^{n-1}}{(l^2+1)^2} & (\text{A.12}) \\
&= \frac{i\mu^{4-n}}{(4\pi)^{n/2}} \frac{\Gamma(n)\Gamma(2-n)}{\Gamma(n/2)\Gamma(2)} \int_0^1 dx (x(1-x)p^2 - m^2)^{\frac{n}{2}-2} \\
&= \frac{i\mu^{4-n}}{(4\pi)^{n/2}} \Gamma\left(2 - \frac{n}{2}\right) (p^2)^{n/2-2} \\
&= \frac{i}{(4\pi)^2} \Gamma(-\epsilon) \left(\frac{p^2}{\mu^2}\right)^{-\epsilon}
\end{aligned}$$

where in the last step, $n = 4 - 2\epsilon$. Letting $\epsilon \rightarrow 0_-$ and Taylor expanding around $\epsilon = 0$ finally give:

$$G^{(2)}(p) = \frac{i}{(4\pi)^2} \left(\frac{1}{\epsilon} + \ln\left(\frac{p^2}{\mu^2}\right) + \mathcal{O}(\epsilon) \right) \quad (\text{A.13})$$

Here μ is the same renormalization scale which appeared in section 1.1.1. For QCD, the UV-regulated theory is defined by a Lagrangian of the form of the QCD Lagrangian, but with all couplings g replace as $g \rightarrow g\mu^\epsilon$.

Appendix B

Generating a Parton Shower by use of the Veto Algorithm

The parton showers described in chapter 2.2, depend on a shower time t . The task of the parton shower is to generate the t values in the shower for a given event according to the distribution $\sum_b \mathcal{I}_{ba}(t)$. For notational purposes, define $f(t) = \sum_b \mathcal{I}_{ba}(t)$, where \mathcal{I} is defined in eq.(2.16). If the primitive function $F(t)$ and its inverse $F^{-1}(t)$ are known, it is easy to select a correct t value:

$$1 - \exp\left(-\int_0^t f(\hat{t})d\hat{t}\right) = 1 - R \quad (\text{B.1})$$

where R is a random number generated according to eq. (2.5). The solution is:

$$F(0) - F(t) = \ln R \quad \Rightarrow \quad t = F^{-1}(F(0) - \ln R) \quad (\text{B.2})$$

However, the primitive function and its inverse of $f(t)$ are rarely known. As in chapter 2.1.1, one may instead try to find another function $g(t)$ such that $g(t) \geq f(t)$ over the interval and where $G(x)$ and $G^{-1}(x)$ are known. Here, the hit and miss scenario described in chapter 2.1.1 does not work, due to the exponential term. Instead one may use the so-called veto algorithm. Consider a particle a being created in a parton shower at a 'time' $t = t_0$. The parton shower also has a cut-off at $t = t_{\max}$ after which no further branchings are allowed. The veto algorithm is then:

1. Start with $i = 0$ and some appropriate t_0 where the particle a is created.
2. Add 1 to i , such as $i \rightarrow i + 1$, and select $t_i = G^{-1}(G(t_{i-1}) - \ln R_1)$, i.e. according to $g(t)$ such that $t_i > t_{i-1}$
3. If $t_i > t_{\max}$ exit the algorithm, a has not branched.
4. If $t_i < t_{\max}$ compare another random number R_2 with the ratio $f(t_i)/g(t_i)$.
If $\frac{f(t_i)}{g(t_i)} \leq R_2$ return to 2

Otherwise, the most recent value is kept as the generated t where a branching $a \rightarrow bc$ has occurred .

5. For the next branching change $b \rightarrow a$ and start at 1 with $t_0 = t$

The main difference from the importance sampling (chapter 2.1) is in the last step, which makes sure that the generated t values are ordered. To understand why this works, the various ways in which a specific t value is chosen may be considered. The probability that a value t is chosen in the first try, i.e. that $t = t_1$, is given by the probability that no intermediate t value is rejected. It is then the branching probability at 'time' t_1 according to $g(t)$ (eq. (2.18)) times the acceptance probability $f(t)/g(t)$:

$$\mathcal{P}_{a0}(t) = g(t) \exp\left(-\int_0^{t_1} g(\hat{t})d\hat{t}\right) \frac{f(t)}{g(t)} = f(t) \exp\left(-\int_0^{t_1} g(\hat{t})d\hat{t}\right). \quad (\text{B.3})$$

Now consider the case where one value t_1 is rejected and the following value kept such that $t = t_2$. Then the probability of choosing t_1 has to be multiplied by the probability $1 - f(t_1)/g(t_1)$ of rejecting it times the probability of choosing t_2 when starting at the value t_1 and again multiplied by the acceptance probability $f(t)/g(t)$:

$$\begin{aligned} \mathcal{P}_{a1}(t) &= \int_0^t dt_1 g(t_1) \exp\left(-\int_0^{t_1} g(\hat{t})d\hat{t}\right) \cdot \left[1 - \frac{f(t_1)}{g(t_1)}\right] \\ &\quad \cdot g(t) \exp\left(-\int_{t_1}^t g(\hat{t})d\hat{t}\right) \cdot \frac{f(t)}{g(t)} \end{aligned} \quad (\text{B.4})$$

As can be seen, the whole r.h.s. is integrated over all possible choices of t_1 . The exponentials together gives an integral over the range 0 to t , just as in eq. (B.3), and the factor for the final step being accepted is also the same. Therefore

$$\mathcal{P}_{a1}(t) = \mathcal{P}_{a0}(t) \int_0^t dt_1 (g(t_1) - f(t_1)) \quad (\text{B.5})$$

In a similar way, the probability that $t = t_3$, i.e. that exactly two intermediate values are rejected then becomes:

$$\begin{aligned} \mathcal{P}_{a2}(t) &= \mathcal{P}_{a0}(t) \int_0^t dt_1 (g(t_1) - f(t_1)) \int_{t_1}^t dt_2 (g(t_2) - f(t_2)) \\ &= \mathcal{P}_{a0}(t) \frac{1}{2} \left(\int_0^t d\hat{t} (g(\hat{t}) - f(\hat{t})) \right)^2. \end{aligned} \quad (\text{B.6})$$

Here the last step can be understood, with $h(t) = g(t) - f(t)$, from:

$$\begin{aligned}
\int_0^t dt_1 h(t_1) \int_{t_1}^t dt_2 h(t_2) &= \int_0^t \int_0^t dt_2 dt_1 h(t_1) h(t_2) \Theta(t_2 - t_1) \\
&= \int_0^t \int_0^t dt_1 dt_2 h(t_2) h(t_1) \Theta(t_1 - t_2) \\
&= \frac{1}{2} \left(\int_0^t \int_0^t dt_2 dt_1 h(t_1) h(t_2) (\Theta(t_2 - t_1) + \Theta(t_1 - t_2)) \right) \\
&= \frac{1}{2} \left(\int_0^t d\hat{t} h(\hat{t}) \right)^2
\end{aligned} \tag{B.7}$$

The second equality comes from symmetry of t_1 and t_2 , the third equality comes from the fact that if $A = B = C$ then $A = 1/2(B + C)$ and in the last step the sum of the Θ functions is unity. For the general case, the i intermediate steps may be ordered in $i!$ different ways. The total probability for accepting t in any step is therefore:

$$\begin{aligned}
\mathcal{P}_a(t) &= \sum_{i=0}^{\infty} \mathcal{P}_{ia} = \mathcal{P}_{0a} \sum_{i=0}^{\infty} \frac{1}{i!} \left(\int_0^t d\hat{t} (g(\hat{t}) - f(\hat{t})) \right)^i \\
&= f(t) \exp \left(- \int_0^t d\hat{t} g(\hat{t}) \right) \exp \left(\int_0^t d\hat{t} (g(\hat{t}) - f(\hat{t})) \right) \\
&= f(t) \exp \left(- \int_0^t d\hat{t} f(\hat{t}) \right)
\end{aligned} \tag{B.8}$$

which is exactly the distribution desired. In each branching also the kinematics of the created particles have to be generated. It is easy to generalize this parton shower algorithm such that $g(t)$ is the integral of $g(t, z)$ over z . Each time a t_i is selected, a z_i is also picked according to $g(t_i, z) dz$ and the point (t, z) is accepted with probability $f(t_i, z_i)/g(t_i, z_i)$. Other variables may be generated in the same fashion. In this way, one can create a parton shower, ordered in t where in each branching the four-momenta, colour information, flavour etc. is kept track of. For final state radiation, the same algorithm is used but with $t_i < t_{i-1}$.

Bibliography

- [1] R. Brock *et al.*, “Handbook of perturbative QCD; Version 1.1: September 1994,” FERMILAB-PUB-94-316. [12](#), [13](#), [130](#), [131](#)
- [2] R. Devenish and A. Cooper-Sarkar, *Deep Inelastic Scattering*. Oxford: Oxford University Press, 2004. [12](#), [15](#), [20](#), [22](#)
- [3] W. S. R.K. Ellis and B. Webber, *QCD and Collider Physics*. Cambridge: Cambridge University Press, 1996. [15](#), [18](#), [24](#)
- [4] C. F. von Weizsacker, “Radiation emitted in collisions of very fast electrons,” *Z. Phys.*, vol. 88, pp. 612–625, 1934. [17](#)
- [5] E. J. Williams, “Nature of the high-energy particles of penetrating radiation and status of ionization and radiation formulae,” *Phys. Rev.*, vol. 45, pp. 729–730, 1934. [17](#)
- [6] Y. L. Dokshitzer, “Calculation of the Structure Functions for Deep Inelastic Scattering and $e^+ e^-$ Annihilation by Perturbation Theory in Quantum Chromodynamics,” *Sov. Phys. JETP*, vol. 46, pp. 641–653, 1977. [23](#)
- [7] V. N. Gribov and L. N. Lipatov, “Deep inelastic $e p$ scattering in perturbation theory,” *Sov. J. Nucl. Phys.*, vol. 15, pp. 438–450, 1972. [23](#)
- [8] L. N. Lipatov, “The parton model and perturbation theory,” *Sov. J. Nucl. Phys.*, vol. 20, pp. 94–102, 1975. [23](#)
- [9] G. Altarelli and G. Parisi, “Asymptotic Freedom in Parton Language,” *Nucl. Phys.*, vol. B126, p. 298, 1977. [23](#)
- [10] R. K. Ellis and Z. Kunszt, “Photoproduction and Electroproduction of Heavy Flavors with Gluon Bremsstrahlung,” *Nucl. Phys.*, vol. B303, p. 653, 1988. [27](#)
- [11] F. James, “MONTE CARLO THEORY AND PRACTICE,” *Rept. Prog. Phys.*, vol. 43, p. 1145, 1980. [33](#)

- [12] L. Lonnblad, “ARIADNE version 4: A Program for simulation of QCD cascades implementing the color dipole model,” *Comput. Phys. Commun.*, vol. 71, pp. 15–31, 1992. [36](#)
- [13] T. Sjostrand, “High-energy physics event generation with PYTHIA 5.7 and JETSET 7.4,” *Comput. Phys. Commun.*, vol. 82, pp. 74–90, 1994. [36](#)
- [14] T. Sjostrand, S. Mrenna, and P. Skands, “PYTHIA 6.4 Physics and Manual,” *JHEP*, vol. 05, p. 026, 2006. [37](#)
- [15] G. Corcella *et al.*, “HERWIG 6: An event generator for hadron emission reactions with interfering gluons (including supersymmetric processes),” *JHEP*, vol. 01, p. 010, 2001. [41](#), [90](#), [104](#)
- [16] Y. L. Dokshitzer, V. A. Khoze, and S. I. Troian, “On specific QCD properties of heavy quark fragmentation (‘dead cone’),” *J. Phys.*, vol. G17, pp. 1602–1604, 1991. [43](#)
- [17] A. Perieanu, “The structure of charm jets and the dead cone effect in deep-inelastic scattering at HERA,” DESY-THESIS-2006-002. [43](#)
- [18] E. D. Bloom and F. J. Gilman, “Scaling, Duality, and the Behavior of Resonances in Inelastic electron-Proton Scattering,” *Phys. Rev. Lett.*, vol. 25, p. 1140, 1970. [44](#)
- [19] R. D. Field and R. P. Feynman, “Quark Elastic Scattering as a Source of High Transverse Momentum Mesons,” *Phys. Rev.*, vol. D15, pp. 2590–2616, 1977. [44](#)
- [20] R. P. Feynman, R. D. Field, and G. C. Fox, “Correlations Among Particles and Jets Produced with Large Transverse Momenta,” *Nucl. Phys.*, vol. B128, pp. 1–65, 1977. [44](#)
- [21] C. Peterson, D. Schlatter, I. Schmitt, and P. M. Zerwas, “Scaling Violations in Inclusive $e^+ e^-$ Annihilation Spectra,” *Phys. Rev.*, vol. D27, p. 105, 1983. [45](#)
- [22] D. Amati and G. Veneziano, “Preconfinement as a Property of Perturbative QCD,” *Phys. Lett.*, vol. B83, p. 87, 1979. [46](#)
- [23] A. Bassetto, M. Ciafaloni, and G. Marchesini, “Color Singlet Distributions and Mass Damping in Perturbative QCD,” *Phys. Lett.*, vol. B83, p. 207, 1979. [46](#)
- [24] G. Marchesini, L. Trentadue, and G. Veneziano, “SPACE-TIME DESCRIPTION OF COLOR SCREENING VIA JET CALCULUS TECHNIQUES,” *Nucl. Phys.*, vol. B181, p. 335, 1981. [46](#)
- [25] I. K. G. Dissertori and M. Schmelling, *Quantum Chromo Dynamics, High Energy Experiments and Theory*. Oxford: Oxford University Press, 2003. [46](#)

- [26] B. Andersson, G. Gustafson, and B. Soderberg, “A General Model for Jet Fragmentation,” *Z. Phys.*, vol. C20, p. 317, 1983. 47
- [27] B. Andersson, G. Gustafson, G. Ingelman, and T. Sjostrand, “Parton Fragmentation and String Dynamics,” *Phys. Rept.*, vol. 97, pp. 31–145, 1983. 47
- [28] T. Sjostrand, “JET FRAGMENTATION OF NEARBY PARTONS,” *Nucl. Phys.*, vol. B248, p. 469, 1984. 47
- [29] E. A. Kuraev, L. N. Lipatov, and V. S. Fadin, “Multi - Reggeon Processes in the Yang-Mills Theory,” *Sov. Phys. JETP*, vol. 44, pp. 443–450, 1976. 50
- [30] E. A. Kuraev, L. N. Lipatov, and V. S. Fadin, “The Pomeranchuk Singularity in Nonabelian Gauge Theories,” *Sov. Phys. JETP*, vol. 45, pp. 199–204, 1977. 50
- [31] I. I. Balitsky and L. N. Lipatov, “The Pomeranchuk Singularity in Quantum Chromodynamics,” *Sov. J. Nucl. Phys.*, vol. 28, pp. 822–829, 1978. 50
- [32] E. Avsar, G. Gustafson, and L. Lonnblad, “Small-x dipole evolution beyond the large- $N(c)$ limit,” *JHEP*, vol. 01, p. 012, 2007. 50
- [33] M. Ciafaloni, “Coherence Effects in Initial Jets at Small q^{*2} / s ,” *Nucl. Phys.*, vol. B296, p. 49, 1988. 50
- [34] S. Catani, F. Fiorani, and G. Marchesini, “QCD Coherence in Initial State Radiation,” *Phys. Lett.*, vol. B234, p. 339, 1990. 50
- [35] S. Catani, F. Fiorani, and G. Marchesini, “Small x Behavior of Initial State Radiation in Perturbative QCD,” *Nucl. Phys.*, vol. B336, p. 18, 1990. 50
- [36] G. Marchesini, “QCD coherence in the structure function and associated distributions at small x,” *Nucl. Phys.*, vol. B445, pp. 49–80, 1995. 50
- [37] H. Jung, “The CCFM Monte Carlo generator CASCADE,” *Comput. Phys. Commun.*, vol. 143, pp. 100–111, 2002. 50
- [38] B. Andersson, G. Gustafson, and J. Samuelsson, “The Linked dipole chain model for DIS,” *Nucl. Phys.*, vol. B467, pp. 443–478, 1996. 50
- [39] M. L. Mangano, P. Nason, and G. Ridolfi, “Heavy quark correlations in hadron collisions at next-to-leading order,” *Nucl. Phys.*, vol. B373, pp. 295–345, 1992. 51, 61, 65
- [40] S. Frixione and B. R. Webber, “Matching NLO QCD computations and parton shower simulations,” *JHEP*, vol. 06, p. 029, 2002. 54, 85
- [41] S. Catani and M. H. Seymour, “NLO calculations in QCD: A general algorithm,” *Nucl. Phys. Proc. Suppl.*, vol. 51C, pp. 233–242, 1996. 58, 68

- [42] S. Frixione, M. L. Mangano, P. Nason, and G. Ridolfi, “Heavy quark correlations in photon - hadron collisions,” *Nucl. Phys.*, vol. B412, pp. 225–259, 1994. [60](#), [61](#), [64](#), [90](#), [104](#)
- [43] R. K. Ellis and P. Nason, “QCD Radiative Corrections to the Photoproduction of Heavy Quarks,” *Nucl. Phys.*, vol. B312, p. 551, 1989. [61](#)
- [44] J. Smith and W. L. van Neerven, “QCD corrections to heavy flavor photoproduction and electroproduction,” *Nucl. Phys.*, vol. B374, pp. 36–82, 1992. [61](#)
- [45] S. Frixione, P. Nason, and B. R. Webber, “Matching NLO QCD and parton showers in heavy flavour production,” *JHEP*, vol. 08, p. 007, 2003. [83](#)
- [46] P. Nason, “A new method for combining NLO QCD with shower Monte Carlo algorithms,” *JHEP*, vol. 11, p. 040, 2004. [88](#)
- [47] S. Frixione, P. Nason, and C. Oleari, “Matching NLO QCD computations with Parton Shower simulations: the POWHEG method,” *JHEP*, vol. 11, p. 070, 2007. [88](#)
- [48] S. Catani, F. Krauss, R. Kuhn, and B. R. Webber, “QCD Matrix Elements + Parton Showers,” *JHEP*, vol. 11, p. 063, 2001. [89](#)
- [49] N. Lavesson and L. Lonnblad, “Extending CKKW-merging to One-Loop Matrix Elements,” *JHEP*, vol. 12, p. 070, 2008. [89](#)
- [50] K. Urban, “Measurement of inclusive and DiJet D^* meson photoproduction at the H1-experiment at HERA,” DESY-THESIS-2009-010. [104](#), [105](#), [106](#)
- [51] W. M. Yao *et al.*, “Review of particle physics,” *J. Phys.*, vol. G33, pp. 1–1232, 2006. [104](#), [114](#)
- [52] L. Gladilin, “Charm hadron production fractions,” 1999. [104](#)
- [53] L. K. Gladilin, “Experimental results on heavy quark fragmentation,” 2006. [104](#)
- [54] A. Aktas *et al.*, “Inclusive D^{*+} meson cross sections and D^{*+} jet correlations in photoproduction at HERA,” *Eur. Phys. J.*, vol. C50, pp. 251–267, 2007. [106](#), [122](#)
- [55] S. Chekanov *et al.*, “Inclusive jet cross sections and dijet correlations in D^{*+} photoproduction at HERA,” *Nucl. Phys.*, vol. B729, pp. 492–525, 2005. [106](#), [110](#), [122](#)
- [56] S. Chekanov *et al.*, “Measurement of beauty photoproduction using decays into muons in dijet events at HERA,” 2008. [115](#)
- [57] A. Aktas *et al.*, “Measurement of beauty production at HERA using events with muons and jets,” *Eur. Phys. J.*, vol. C41, pp. 453–467, 2005. [115](#)

-
- [58] S. Chekanov *et al.*, “Bottom photoproduction measured using decays into muons in dijet events in e p collisions at $s^{*1/2} = 318\text{-GeV}$,” *Phys. Rev.*, vol. D70, p. 012008, 2004. 115
- [59] A. Nikiforov, “The Impact of HERA Physics for LHC”, Epiphany 2009, Cracow.” 125
- [60] M. Klein and P. Newman, “LHeC: novel designs for electron quark scattering,” *CERN Courier*, vol. April, 2009. 126
- [61] G. Leibbrandt, “Introduction to the Technique of Dimensional Regularization,” *Rev. Mod. Phys.*, vol. 47, p. 849, 1975. 128

Acknowledgements

I am very thankful to Dr. Carsten Niebuhr and Dr. Hannes Jung for giving me the opportunity to come to Hamburg and DESY. I am also thankful to Dr. Benno List and Prof. Dr. Robert Klanner for their support in the finishing of this thesis.

To Hannes, my supervisor, I am very grateful for all the invaluable advise, support, and help. For organizing many inspirational meetings and work-shops, and always bringing people together in conversations about physics, life and everything, over food or coffee and/or cookies. I am also thankful for all the time Hannes spent reading and commenting my thesis, causing many improvements. I am also thankful to Dr. Stefano Frixione, for good help, useful discussions and for explaining many things to me.

I would like to express my gratitude to my referees Prof. Dr. Joachim Bartels and Prof. Dr. Peter Schleper for agreeing to evaluate my work.

I am thankful to Dr. Tim Namssoo, Dr. Zoltan Nagy and Matthew Forrest for reading and commenting parts of the thesis.

Many thanks to Axel Cholewa for translating the abstract into German.

I would like to give thanks to H1, especially the heavy flavour working group, for advise and support and for letting me do this phenomenology thesis within such a splendid experimental collaboration. I have learned much which I would otherwise not have.

Also special thanks to the physics and cookies group for many good discussion. Too many have been at these meetings through my time here to be mentioned, but I am grateful to all of you.

Many thanks to the original office: Snow, Lluís and Zlatusha, for many cultural exchanges, for keeping the dull moments to a minimum and for great friendship. Also, many thanks to Albert in the new office. Less cultural exchanges, but non lesser friendship.

Also, many thanks to the four o'clock fika meeting crew: Sarah, Homer, Michal, Niladri, Federico, Carlos, Mira, Krusha, The Axe, Käpt'n, Hombro, Magic, Andrew and Julia.